

UNIVERSITY OF CALIFORNIA

Santa Barbara

Silicon Evanescent Lasers

A Dissertation submitted in partial satisfaction of the  
requirements for the degree Doctor of Philosophy  
in Electrical and Computer Engineering

by

Alexander Wei-Liang Fang

Committee in charge:

Professor John E. Bowers, Chair

Professor Nadir Dagli

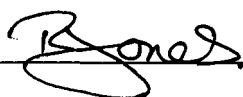
Professor Evelyn Hu

Dr. Mario J. Paniccia

Dr. Richard Jones

March 2008

The dissertation of Alexander Wei-liang Fang is approved.



Dr. Richard Jones



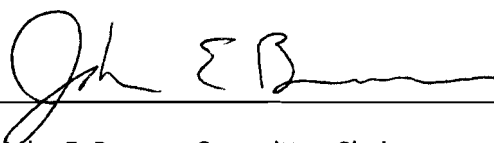
Dr. Mario Paniccia



Professor Nadir Dagli



Professor Evelyn Hu



Professor John E. Bowers, Committee Chair

March 2008

# Silicon Evanescent Lasers

Copyright © 2008

by

Alexander Wei Liang Fang

## **ACKNOWLEDGEMENTS**

I have always found the acknowledgement section of dissertations to be one of the most interesting to read since it gives a small glimpse of the author's journey to this stage in their life and the people, without whom, this destination would be unreachable. I am in debt to so many people for providing me with inspiration, emotional support, and technical guidance that has led to the completion of this period of my life.

I would first like to thank my loving parents Jean, Peter, and Josephine, my siblings, Phyllis and Eugene, and my grandmother, Yun-Hsia Fang, for being patient with me and believing in me while I spent the first 3 out of 6 years of my college career failing courses and trying to figure out what I wanted to do in life.

Next I'd like to thank my advisor, John Bowers, for taking me in as his student and giving me with the opportunity to work in his research group. During these past 4.5 years, John has provided an environment that not only helped me grow technically as a researcher, but also as a person. His work hard, play hard mentality is instilled in each of his students, and I am privileged to be one of his students.

In addition to Dr. Bowers, I'd like to acknowledge my committee members. Professor Nadir Dagli's and Professor Evelyn Hu's wealth of knowledge in optoelectronics and semiconductor fabrication have been invaluable to this research. Dr. Richard Jones' mentorship and scrutiny of results has molded me into

the researcher I am today. Dr. Mario Paniccia's vision has allowed me to go to "the superbowl" with him on the silicon Raman laser project, and the silicon evanescent laser project, making graduate school a truly memorable experience.

I would like to give special thanks Hyundai Park. The development of the silicon evanescent platform was only possible through the synergy of our complementary skill set with Hyundai bringing the brains and with me bringing the humor. I'd like to think that we both rubbed off on each other and I was able to steal some of his brains.

I would also like to thank the rest of the Bowers' group during my time here at UCSB: Gehong, Manish, Geske, Staffan, Garrett, Gan, Hubert, Raja, Satoshi, Emily, Brian Koch, Ying-Hao, Hui-wen, Di, Andy, Brian Mcskimming, Matt, Je-Hyeong, Ashok, Siddharth, and Jock. Anand Ramaswamy should get special recognition for being the target for all my evil plots, and living to tell about them.

The Bowers' group assistants: Kate Ferrian, Jasmine Young, Christina Zumenstein, and Christine Dillard-Herrera, without whom I would be in extreme debt, and be buried in paperwork that, in reality, I should have taken care of to begin with.

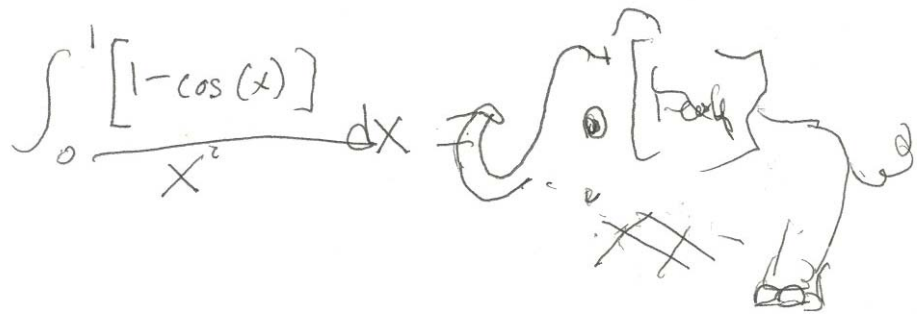
I'd like to thank all my colleagues at Intel in Santa Clara, and Israel: Haisheng Rong, Andrew Alduino, Ansheng Liu, Ling Liao, Jeffrey Tseng, Oded Cohen, Omri Raday, Hanan Bar and others.

None of the device fabrication would have been possible without the UCSB nanofabrication facility staff. Jack Whaley, Brian Thibeault, and the rest of the cleanroom staff are a key element of what makes UCSB a world class research institution. Don Freeborn deserves special recognition for dealing with the demanding group of processers known as the “UCSB wafer-bonders”.

I’d also like to thank my friends, classmates, and collaborators from the Coldren, Mishra, Dagli, Blumenthal groups and back at home for assistance in research, stimulating conversations, and a high tolerance my extreme behavior: Jon Klamkin, Janet Chen, Erica Lively, Joe Summers, Milan Mashanovitch, John Mack, Chris Sarantos, Chris Schaake, Eric Snow, Chang-Soo Suh, Ric Lwin, Eric Liu, Vikrum Nijjar, Dave Fan, Damon Do, Vijay Kamath, Jerry Sublett, and others.

Finally I’d like to thank my fiancée, Angela Penn, for understanding and supporting me when I chose to be 2500 miles away from her in order to seek out my dreams at UCSB.

This dissertation is dedicated  
to my family and fiancée



## CURRICULUM VITAE

### ALEXANDER WEI-LIANG FANG

Born October 26, 1979, Philadelphia, Pennsylvania

#### EDUCATION

*Doctor of Philosophy in Electrical and Computer Engineering*  
University of California, Santa Barbara, March 2008

*Master of Science in Electrical and Computer Engineering*  
University of California, Santa Barbara, December 2005

*Bachelors of Science in Electrical Engineering*  
San Jose State University, May 2003

#### TECHNICAL EXPERIENCE

*Intel Corporation – Photonics technology labs*  
July 2004 – January 2005

*Lawrence Livermore National Laboratory – FALCON lab*  
July 2003 – August 2003

#### MENTORING EXPERIENCE

*San Jose State University – Senior Design Project Mentor*  
August 2006 – December 2007

*NSF NNIN REU Program – REU Mentor*  
July 2006 – August 2006  
July 2007 – August 2007

*A.V.I.D. Program – Student Mentor/Tutor*  
January 2003 – May 2003

#### PATENTS

“Dual core corrugated Bragg grating,” O. Cohen, R. Jones, D. Rubin, **A. W. Fang**, US Patent number 7292753, Issued 11/6/2007

“Electrically pumped hybrid semiconductor evanescent laser,” **A. W. Fang**, H. Park, J. E. Bowers, M. Paniccia, R. Jones, O. Cohen, Filed 6/2006



## PUBLICATIONS

### *Journal Papers*

"A distributed feedback silicon evanescent laser," **A. W. Fang**, E. Lively, Y-H. Kuo, D. Liang, J. E. Bowers, *Optics Express*, Vol. 16, No. 7, pp. 4413-4419, 2008

"A racetrack mode-locked silicon evanescent laser," **A. W. Fang**, B. R. Koch, K. Gan, H. Park, R. Jones, O. Cohen, M. J. Paniccia, D. Blumenthal, J. E. Bowers, *Optics Express*, Vol. 16, No. 2, pp. 1393-1398, 2008

"Experimental and theoretical thermal analysis of a Hybrid Silicon Evanescent Laser," M. N. Sysak, H. Park, **A. W. Fang**, J. E. Bowers, R. Jones, O. Cohen, O. Raday, and M. Paniccia, *Optics Express*, Vol., 15 No. 23 Pg: 15041-15046, 2007

"A hybrid AlGaInAs-silicon evanescent preamplifier and photodetector," H. Park, Y.-H. Kuo, **A. W. Fang**, R. Jones, O. Cohen, M. J. Pannicia, J. E. Bowers, *Optics Express*, Vol. 15, No. 21, 2007

"Mode-locked silicon evanescent lasers," B. R. Koch, **A. W. Fang**, O. Cohen, and J. E. Bowers, *Optics Express*, Vol. 15, No. 18, pp. 11225-11233, 2007

"1310nm silicon evanescent laser," H.-H. Chang, **A. W. Fang**, M. N. Sysak, H. Park, R. Jones, O. Cohen, O. Raday, M. J. Paniccia, and J. E. Bowers, *Optics Express*, 15, 11466-11471, 2007

"Hybrid silicon integration," R. Jones, H. Park, **A. W. Fang**, J. E. Bowers, O. Cohen, O. Raday and M. J. Paniccia, *Journal of Materials Science: Materials in Electronics*, DOI 10.1007/s10854-007-9418-y, 2007

"Hybrid Si evanescent devices," **A. W. Fang**, H. Park, Y.-H. Kuo, R. Jones, O. Cohen, D. Liang, O. Raday, M. N. Sysak, M. J. Paniccia, and J. E. Bowers, *Materials Today*, 10, 7-8, 2007

"A hybrid AlGaInAs-silicon evanescent waveguide photodetector," H. Park, **A. W. Fang**, R. Jones, O. Cohen, O. Raday, M. N. Sysak, M. J. Paniccia, and J. E. Bowers, *Optics Express*, Vol. 15, Issue 10, pp. 6044-6052, 2007

"Integrated AlGaInAs-silicon evanescent race track laser and photodetector," **A. W. Fang**, R. Jones, H. Park, O. Cohen, O. Raday, M. J. Paniccia, and J. E. Bowers, *Optics Express*, Vol. 15, Issue 5, pp. 2315-2322, 2007

"A Hybrid AlGaInAs-Silicon Evanescent Amplifier," H. Park, **A. W. Fang**, O. Cohen, R. Jones, M. J. Paniccia, J. E. Bowers, *IEEE Photonics Technology Letters*, Vol. 19, No. 4, 2007

"Design and Fabrication of Optically Pumped Hybrid Silicon-AlGaInAs Evanescent Lasers," H. Park, **A. W. Fang**, O. Cohen, R. Jones, M. J. Paniccia, J. E. Bowers, *IEEE Journal of Selected Topics in Quantum Electronics*, Vol. 12, Part 2, page 1657-1663, 2006

"Electrically pumped hybrid AlGaInAs-silicon evanescent laser," **A. W. Fang**, H. Park, O. Cohen, R. Jones, M. J. Paniccia, and J. E. Bowers, *Optics Express*, 14, 9203-9210, 2006

"A Continuous-Wave Hybrid AlGaInAs-Silicon Evanescent Laser," **A. W. Fang**, H. Park, R. Jones, O. Cohen, M. J. Paniccia, J. E. Bowers, *IEEE Photonics Technology Letters*, Vol 18, Issue 10, pg 1143- 1145, 2006

"Hybrid Silicon Evanescent Laser Fabricated With a Silicon Waveguide and III-V Offset Quantum Wells," H. Park, **A. W. Fang**, S. Kodama, and J. E. Bowers, *Optics Express*, 13, 9460-9464, 2005

"A Continuous-Wave Raman Silicon Laser," H. Rong, R. Jones, A. Liu, O. Cohen, D. Hak, **A. W. Fang**, M. Paniccia, *Nature*, Vol. 433, Pg. 725 - 728, 2005

"Net Continuous Wave Optical Gain in a Low Loss," H. Rong, R. Jones, A. Liu, O. Cohen, D. Hak, **A. W. Fang**, M. Paniccia, *Optics Express*, Vol. 13, No. 2, Pg. 519 - 525, 2005

"An All-Silicon Raman Laser," H. Rong, A. Liu, R. Jones, O. Cohen, R. Nicolaescu, **A. W. Fang**, M. Paniccia, *Nature*, Vol. 433, Pg. 292 - 294, 2005

### *Conference Papers*

"Integrated Hybrid Lasers and Amplifiers on a Silicon Platform," R. Jones, M. N. Sysak, H. Park, **A. W. Fang**, H.-H. Chang, Y.-H. Kuo, J. E. Bowers, O. Raday, O. Cohen, Optical Fiber Communications Conference (OFC) 2008, San Diego, CA OWM1, 2008

"Distributed Feedback Silicon Evanescent Laser," **A. W. Fang**, E. Lively, Y.-H. Kuo, D. Liang, J. E. Bowers, Optical Fiber Communications Conference (OFC) 2008, San Diego, CA postdeadline session PDP15, 2008

"All-Optical Clock Recovery with Retiming and Reshaping Using a Silicon Evanescent Mode-Locked Ring Laser," B. R. Koch, **A. W. Fang**, H. N. Poulsen, H. Park, D. J. Blumenthal, and J. E. Bowers, R. Jones and M. J. Paniccia, and O. Cohen, Optical Fiber Communications Conference (OFC) 2008, San Diego, CA Paper OMN1 (Invited), 2008

"Experimental and Theoretical Analysis of Thermal Impedance in a Hybrid Silicon Evanescent Laser," M. N. Sysak, H. Park, **A. W. Fang**, J. E. Bowers, R. Jones, O. Cohen, O. Raday, and M. Paniccia, LEOS annual meeting 2007, ThR2, 2007

"Hybrid AlGaInAs-silicon evanescent racetrack laser," **A. W. Fang**, R. Jones, H. Park, O. Cohen, M. J. Paniccia, and J. E. Bowers, LEOS annual meeting 2007, ThR1 (Invited), 2007

"Hybrid III-V and IV lasers and amplifiers," J. E. Bowers, H. Park, **A. W. Fang**, Y.-H. Kuo, R. Jones, O. Cohen, O. Rada, M. J. Paniccia, European Conference on Optical Communications (ECOC) 2007, Paper 9.2.1 (Invited), 2007

"A 40 GHz Mode Locked Silicon Evanescent Laser," B. R. Koch, **A. W. Fang**, H.-H. Chang, H. Park, Y.-H. Kuo, R. Jones, O. Cohen, O. Rada, M. J. Paniccia, J. E. Bowers, 4th International Conference on Group IV Photonics, Tokyo Japan, wb1 (invited), 2007

"1310nm Silicon Evanescent Laser," H.-H. Chang, **A. W. Fang**, M. N. Sysak, H. Park, Y.-H. Kuo, R. Jones, O. Cohen, O. Rada, M. J. Paniccia, J. E. Bowers, 4th International Conference on Group IV Photonics, Tokyo Japan, wb3, 2007

"Silicon Evanescent Racetrack Laser," **A. W. Fang**, H. Park, J. E. Bowers, R. Jones, M. J. Paniccia, O. Cohen, O. Rada, Frontiers in Optics 2007, San Jose, California, FTuM3(invited), 2007

"Integrated AlGaInAs-silicon evanescent racetrack laser and photodetector," **A. W. Fang**, R. Jones, H. Park, O. Cohen, O. Rada, M. J. Paniccia, J. E. Bowers, Optics East 2007, Proc. of SPIE Vol. 6775 67750P-1 (Invited), 2007

"Silicon Evanescent Amplifiers," J. E. Bowers, H. Park, **A. W. Fang**, R. Jones, M. J. Paniccia, O. Cohen, CLEO Pacific Rim 2007, Seoul, Korea, FA1-2 (invited), 2007

"Hybrid Silicon Integration," R. Jones, H. Park, **A. W. Fang**, J. E. Bowers, O. Cohen, O. Rada, and M. J. Paniccia, ICOOPMA (The International Conference on Optical, Optoelectronic and Photonic Materials and Applications), London, 2007

"Integrated Optical Amplifiers on Silicon Waveguides," J. E. Bowers, H. Park, Y.-H. Kuo, **A. W. Fang**, R. Jones, M. J. Paniccia, O. Cohen, O. Rada, IPNRA 2007, invited paper, ITuG1, 2007

"Integrated Hybrid Silicon Evanescent Racetrack Laser and Photodetector," **A. W. Fang**, R. Jones, H. Park, O. Cohen, O. Rada, M. J. Paniccia, J. E. Bowers, 12th OptoElectronics and Communications Conference, Yokohama Kanagawa, Japan (Invited), 2007

"A hybrid silicon evanescent photodetector," H. Park, **A. W. Fang**, R. Jones, O. Cohen, O. Rada, M. N. Sysak, M. J. Paniccia, J. E. Bowers, Device Research Conference (DRC 2007), Notre Dame, IN, 2007

"Low Temperature Wafer Bonding for III-V Si Photonic Integrated Circuits," D. Liang, H. Park, **A. W. Fang** and J. E. Bowers, Electronic Materials Conference, paper L3, 2007

"Hybrid Silicon Evanescent Photonic Integrated Circuit Technology," J. E. Bowers, **A. W. Fang**, H. Park, R. Jones, O. Cohen, and M. J. Paniccia, CLEO 2007, CTuQ1, Baltimore MD, 2007

"High speed data amplification using hybrid silicon evanescent amplifier," Y.-H. Kuo, H. Park, **A. W. Fang**, J. E. Bowers, R. Jones, M. Paniccia, O. Cohen, CLEO 2007, CTuI11, 2007

"An electrically pumped hybrid silicon evanescent amplifier," H. Park, **A. W. Fang**, R. Jones, O. Cohen, J. E. Bowers, Optical Fiber Communication Conference (OFC 2007), OTuD2, Anaheim CA, 2007

"Hybrid Silicon Evanescent Laser in a Silicon-on-Insulator Waveguide," J.E. Bowers, **A. W. Fang**, H. Park, R. Jones, O. Cohen, M. J. Paniccia, Optical Fiber Communication Conference (OFC 2007), OTuK4, Anaheim CA, 2007

"High Temperature Silicon Evanescent Lasers," J. E. Bowers, H. Park, **A. W. Fang**, R. Jones, O. Cohen, M. J. Paniccia, Photonics West 2007 (PW 2007), Proceedings of SPIE, Vol. 6485, invited paper, 2007

"Scalable Wafer Bonding for Active Photonic Devices on Silicon," J. E. Bowers, H. Park, **A. W. Fang**, R. Jones, O. Cohen, M. Paniccia, LEOS Annual Meeting, TuC1 (Invited), 2006

"40 C Continuous-Wave Electrically Pumped Hybrid Silicon Evanescent Laser," H. Park, **A. W. Fang**, R. Jones, O. Cohen, M. J. Paniccia, and J. E. Bowers, International Semiconductor Laser Conference 2006 (ISLC 2006), post deadline paper, 2006

"Silicon Evanescent Lasers and Amplifiers," J. E. Bowers, **A. W. Fang**, H. Park, R. Jones, O. Cohen, M. J. Paniccia, Group IV Photonics Conference 2006 (GFP2006), Invited Paper, ThB1, 2006

"Design of Hybrid Silicon Evanescent Amplifiers," J. E. Bowers, H. Park, **A. W. Fang**, R. Jones, O. Cohen, M. J. Paniccia, COIN 2006, Jeju Korea, 2006

"Hybrid silicon evanescent lasers," J. E. Bowers, **A. W. Fang**, H. Park, O. Cohen, R. Jones, M. J. Paniccia, Device Research Conference 2006 (DRC 2006), (invited paper) University Park, PA, 2006

"A Technology for Integrating Active Photonic Devices on SOI Wafers," J. E. Bowers, H. Park, **A. W. Fang**, R. Jones, O. Cohen, and M. J. Paniccia, Indium Phosphide and Related Materials Conference (IPRM 2006), Princeton, NJ, Invited Paper, 2006

"SOI-based monolithic integration of SiON and Si planar optical circuits," O. Cohen, R. Jones, O. Raday, **A. W. Fang**, N. Izhaky, D. Rubin, M. Paniccia, Photonics Europe, 2006

"An optically pumped silicon evanescent laser operating continuous wave at 60 °C," H. Park, **A. W. Fang**, R. Jones, O. Cohen, M. J. Paniccia, and J. E. Bowers, Optical Fiber Communication Conference (OFC 2006), paper OWH2, 2006

"Heterogeneous Integration of Silicon and AlGaInAs for a Silicon Evanescent Laser," **A. W. Fang**, H. Park, R. Jones, O. Cohen, M. J. Paniccia, J. E. Bowers, Proc. of SPIE 6133, (Photonics West 2006), Vol. 6133, 61330W, San Jose, CA, Invited Paper, 2006

"An Optically Pumped Silicon Evanescent Laser," **A. W. Fang**, H. Park, S. Kodama, J. E. Bowers, The 31st European Conference on Optical Communications (ECOC 2005), SECC, Glasgow, Scotland, 2005

"Novel Laser Diode Structure consisting of a Si Waveguide and Compound-Semiconductor MQW Layers for Si Platform Integration," S. Kodama,, H. Park, **A. W. Fang** and J. E. Bowers, International Conference on Solid State Devices and Materials, Kobe, Japan, 2005

"Integration of SiON Gratings with SOI," R. Jones, O. Cohen, H. Chan, D. Rubin, **A. W. Fang** and M. Paniccia, GFP 2005 2nd International Conference on Group IV Photonics, Antwerp, Belgium, 2005

## ABSTRACT

### Silicon Evanescent Lasers

by

Alexander Wei-Liang Fang

Silicon photonics has seen much advancement in recent years, driven by the potential to break the cost barrier of optoelectronics through leveraging the low cost manufacturing infrastructure of the CMOS electronics industry. Silicon Raman lasers have been demonstrated, but an electrically pumped laser made of pure silicon has yet to be realized. Hybrid integration approaches that consist of die bonding prefabricated compound semiconductor lasers to silicon waveguides fall short of the requirements needed for high volume silicon photonic integration manufacturing due to the high precision alignment bonding techniques, leading to large variations in coupling losses and scalability limitations. In this dissertation, we present the silicon evanescent laser, an electrically pumped laser architecture that consists of III-V layers bonded to silicon waveguide optical cavities. The optical mode lies primarily in the low loss silicon waveguide while obtaining optical gain through evanescent coupling into the III-V region. Since lateral confinement is controlled by the silicon waveguide fabrication, this self aligned process allows for thousands of lasers to be fabricated on a silicon die in a single bond step. Subsequent processing is done on the III-V but can be conducted using standard lithographic based

processing techniques. We have demonstrated electrically pumped Fabry-Perot lasers, racetrack resonator lasers under continuous wave and mode locked operation and distributed feedback (DFB) lasers utilizing this platform.

## TABLE OF CONTENTS

<b>1. Introduction</b>	<b>1</b>
1.1. Silicon Photonics	1
1.2. Silicon Photonic Integrated Circuit Laser Sources	3
1.3. Silicon Evanescent Device Concept	5
1.4. This Dissertation	6
<b>2. Silicon Evanescent Laser Design, Fabrication, and Proof of Concept</b>	<b>9</b>
2.1. Silicon Evanescent Waveguide Design	10
2.2. Device Fabrication	17
2.3. Proof of Concept – Optically Pumped Silicon Evanescent Lasers	29
2.4. Summary	37
<b>3. Electrically Pumped Silicon Evanescent Lasers – Fabry Perot Lasers</b>	<b>40</b>
3.1. Pulsed Lasing Device Structure	40
3.2. Pulsed Lasing Operation	43
3.3. Continuous Wave Device Structure - Lateral Current Confinement	48
3.4. Continuous Wave Lasing	51
3.5. Thermal Analysis	61
3.6. Second Generation Fabry-Perot Lasers	63
3.7. Thermal Modeling of Fabry-Perot Lasers	67
3.8. Summary	69
<b>4. Electrically Pumped Silicon Evanescent Lasers – Racetrack Ring Lasers</b>	<b>72</b>
4.1. Racetrack Laser Design	73
4.2. Continuous Wave Lasing	84
4.3. Mode Locked Racetrack Lasers	89
4.4. Summary	97
<b>5. Distributed Feedback Silicon Evanescent Lasers</b>	<b>100</b>
5.1. Bragg Grating Design and Fabrication	102
5.2. Distributed Feedback Silicon Evanescent Lasers	105
5.3. Summary	115
<b>6. Conclusions and Future Work</b>	<b>117</b>
6.1. Summary	118
6.2. Future Directions	121
<b>A. Appendix</b>	<b>129</b>
a. Electrically Pumped SEL Process Follower	129



# Chapter 1 - Introduction

## *1.1 - Silicon Photonics*

Silicon is the material of choice for most applications in the world of electronics. People have spent decades perfecting the understanding of silicon and building up a fabrication infrastructure that is unsurpassed by any other semiconductor material system that allows for the high yield and high volume manufacturing of electronic systems. In recent years, a lot of attention in optoelectronics has shifted from compound semiconductor based material systems to silicon.

Optical communication systems are still predominantly put together on the component level, similar to electronic systems of the 1950s where resistors, capacitors, and transistors were soldered together individually. This keeps the cost of optical communication systems high, due to assembly and packaging costs. It also limits the scalability of the number of optical components within a system. As a result, optoelectronic systems have remained in markets that are high performance, and low volume, such as long haul wide area networks (WANs) and metro area networks (MANs) that connect cities digitally throughout the world, serving as the backbone of the internet, and telephone traffic where the cost of high bandwidth optical links can be justified. As our society moves further into the digital era, the demand for greater bandwidth drives the push for optical communication links in to

our homes. The supply for this demand can only happen if the cost barrier is broken, allowing for high volume deployment of optical links. The integration of components onto a single chip revolutionized electronics and the hope is to use integration as an enabler for a similar revolution in optoelectronics. Silicon based photonics strives to further reduce the cost of photonic integrated circuits by utilizing the fabrication infrastructure of silicon CMOS electronics to realize high yield manufacturing while reducing the costs associated with running dedicated photonic fabrication lines.

At first glance, silicon does not have much in its toolbox for optoelectronics. First of all, it is an indirect band gap semiconductor leading to inefficient band to band light emission. Secondly, the inversion symmetry of silicon's crystal structure results in the absence of the linear electro-optic effect [1]. Thirdly, the bandgap of silicon is 1.12 eV which corresponds to absorption of wavelengths of  $\sim 1.1$  microns and shorter making it poor for light detection at the telecommunication wavelength windows at 1.3 microns and 1.55 microns [2]. Even with these properties stacked against it, the potential to leverage silicon's high volume, low cost manufacturing infrastructure as a means to produce low cost photonic systems that can finally break the cost barrier of photonic systems has driven researchers to press on and has resulted in great strides in the field of silicon photonics. Low loss waveguides in silicon have been demonstrated with losses on the order of  $\sim 0.3$  dB/cm ( $0.075$  cm<sup>-1</sup>) [2]; over an order of magnitude improvement over their indium phosphide counterparts ( $\sim 4 - 40$  dB/cm,  $\sim 1 - 10$  cm<sup>-1</sup>). Silicon modulators have broken the

previous 20 MHz bandwidth limit with bandwidths of 30 GHz making them viable for high speed communication systems [4][5]. New ultra compact modulators utilizing ring resonators and pre-emphasized signals have shown modulation speeds of 18 Gb/s while only occupying  $12 \times 12 \mu\text{m}^2$  allowing for dense integration [6]. High speed silicon germanium photodetectors have been demonstrated in the 1550 nm [7] and the 1310 nm regime with data rates of 40 Gb/s [8]. These developments have given silicon almost everything it needs in the photonic toolbox to be used as a platform for photonic integrated circuits. The only missing piece is and electrically pumped laser on silicon.

## *1.2 - Silicon Photonic Integrated Circuit Laser Sources*

Although optically pumped silicon lasers have been demonstrated by utilizing stimulated Raman scattering (SRS) in silicon waveguides, there is no clear path to realizing an electrically pumped laser out of pure silicon [9][10].

Figure 1-1 illustrates a few methods for getting light onto a silicon photonic integrated circuit. The first approach involves using an off chip laser that is fiber coupled to the silicon chip (Figure 1-1a). Once the light is on the silicon, it can be modulated or detected via silicon modulators and detectors. Although Raman scattering can be used to achieve narrowband amplification (10 nm) via a high power pump laser [11], true broadband (~40 nm) amplification at is currently unavailable with this method. This method can be thought of as an optical power

supply. In order to minimize fabrication costs, v-grooves or other passive alignment techniques should be used in this approach to reduce packaging costs.

The second approach is taking prefabricated compound semiconductor lasers and bump bonding them to silicon waveguides (Figure 1-1b). Since the waveguide in the laser and the waveguide of the silicon is defined prior to bonding, tight alignment (< micron) needs to be made during the bonding process to ensure efficient coupling.

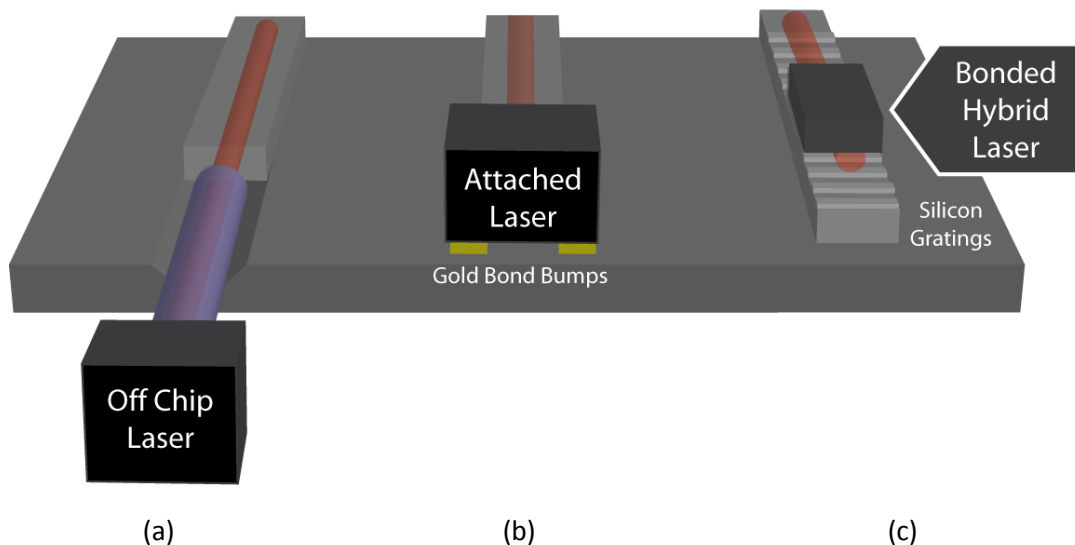


Figure 1-1 – Three methods to supply laser light to a photonic integrated circuit on silicon: (a) fiber coupling off chip lasers to silicon waveguides, (b) die attaching prefabricated III-V lasers, and (c) hybrid integration of III-V materials and silicon to form a hybrid laser.

The third approach is to transfer thin crystalline films to the silicon, and process them with standard lithographic and etching processes to define the device structure (Figure 1-1c). This approach removes the high precision alignment step from the bonding step, and moves it to lithographic steps, allowing for high precision alignment with standard semiconductor fabrication tools.

Wada *et al.* first demonstrated a III-V Fabry-Perot laser, fabricated on a silicon wafer via direct wafer bonding [12]. The optical mode of this laser lies entirely in the III-V layers, 1.5 microns away from the bonded interface and would require special coupling schemes in order to integrate it with photonics imbedded in a layer on the silicon. Although, the silicon served only as a carrier medium, this demonstration shows that the quality of thin crystalline III-V materials transferred to silicon can be maintained to create electrically driven lasers on silicon.

### *1.3 - Silicon Evanescent Device Concept*

The silicon evanescent waveguide structure also utilizes thin films crystalline III-V films transferred to silicon, but in this structure, the optical mode lies primarily in the silicon waveguide region and is evanescently coupled through the bonded interface and a thin InP layer in the III-V region to a set of quantum wells (Figure 1-2). This allows for high coupling efficiency to other passive silicon devices; typically between -3 dB and -1 dB. Since the waveguide definition is done in the silicon region, the cavity is defined by processing on the silicon through the introduction of ring resonator topographies or the use of Bragg reflectors to create distributed feedback (DFB) or distributed Bragg reflector (DBR) lasers. Although we focus

primarily on the development of lasers based on this platform, this structure is also useful for amplifiers [13], photodetectors [14], and modulators [15].

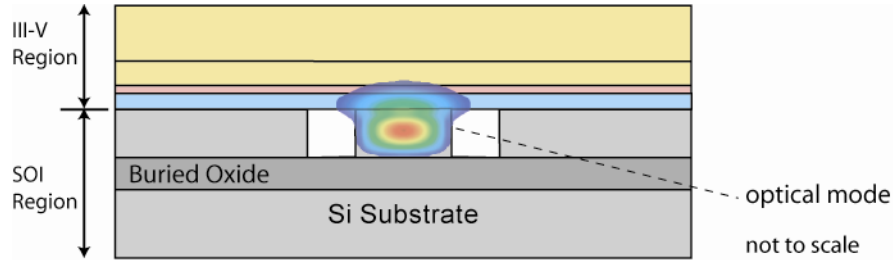


Figure 1-2 – Silicon evanescent waveguide structure consisting of III-V active layers bonded to a silicon on insulator (SOI) waveguide.

#### *1.4 - This Dissertation*

This dissertation focuses on the development of the silicon evanescent device platform to realize electrically pumped lasers on silicon. Chapter 2 describes the modal properties of silicon evanescent device platform along with the fabrication of these devices. The demonstration of optically pumped Fabry Perot silicon evanescent lasers is presented at the end of this chapter as a proof of concept. Chapter 3 describes the development of the current injection scheme and the realization of electrically pumped Fabry Perot silicon evanescent lasers. This chapter includes two generations of devices with an analysis of the device thermal performance. Chapter 4 presents the design and demonstration of racetrack silicon evanescent lasers with integrated photodetectors in order to demonstrate lasers that do not rely on facet preparation and to illustrate the use of silicon patterning to

define the laser cavity. These lasers operate continuous wave and under mode locked operation. Distributed feedback silicon evanescent lasers are presented in Chapter 5 where the gratings are fabricated in the silicon waveguide to yield single wavelength outputs for wavelength division multiplexing applications. Chapter 6 concludes this dissertation with a discussion on the future development of silicon evanescent lasers.

## References

- [1] G. T. Reed & C. E. J. Png, "*Silicon optical modulators*," Mater. Today, 8, 40–50 (2005)
- [2] B. Streetman, S. Banerjee, *Solid State electronic Devices*, New Jersey: Prentice Hall, pp. 524. (2000)
- [3] H. Rong, R. Jones, A. Liu, O. Cohen, D. Hak, A. W. Fang, M. Paniccia, "*A continuous-wave Raman silicon laser*." Nature, 433, 725–727 (2005)
- [4] A. Liu *et al.*, "*A high-speed silicon optical modulator based on a metal-oxide-semiconductor capacitor*," Nature, 427, 615–618 (2004)
- [5] A. Liu *et al.*, "*High-speed silicon modulator for future VLSI interconnect*," Indium Phosphide and Rel. Mat. Conf. (2007)
- [6] S. Manipatruni, Q. Xu, B.S. Schmidt, J. Shakya, and M. Lipson, "*High Speed Carrier Injection 18 Gb/s Silicon Micro-ring Electro-optic Modulator*," Lasers and Electro-Optic Society annual meeting (2007)
- [7] D. Ahn, C.-Y. Hong, J. Liu, W. Giziewicz, M. Beals, L. C. Kimerling, J. Michel, J. Chen, and F. X. Kärtner, "*High performance, waveguide integrated Ge photodetectors*," Opt. Express 15, 3916-3921 (2007)
- [8] T. Yin, R. Cohen, M. Morse, G. Sarid, Y. Chetrit, D. Rubin, M. Paniccia, "*40Gb/s Ge-on-SOI Waveguide Photodetectors by Selective Ge Growth*," Optical Fiber Communications Conference, OMK2 (2008)
- [9] O. Boyraz and B. Jalali, "*Demonstration of a silicon Raman laser*," Opt. Express 12, 5269-5273 (2004)

- [10] H. Rong, R. Jones, A. Liu, O. Cohen, D. Hak, A. W. Fang, M. Paniccia, "A *continuous-wave Raman silicon laser.*" *Nature*, 433, 725–727 (2005)
- [11] D. R. Solli, P. Koonath, B. Jalali, "*Broadband Raman amplification in silicon*" Lasers and Electro-Optics Society Annual Meeting, 886-887 (2007)
- [12] H. Wada and T. Kamijoh, "*Room-Temperature CW operation of InGaAsP Lasers on Si Fabricated by Wafer Bonding,*" *IEEE Photon. Technol. Lett.* 8, 173-175 (1996).
- [13] H. Park, A. W. Fang, O. Cohen, R. Jones, M. J. Paniccia, J. E. Bowers, "*A Hybrid AlGaInAs-Silicon Evanescent Amplifier,*" *IEEE Photon. Technol. Lett.*, 19, 4 (2007)
- [14] H. Park, A. W. Fang, R. Jones, O. Cohen, O. Rada, M. N. Sysak, M. J. Paniccia, and J. E. Bowers, "*A hybrid AlGaInAs-silicon evanescent waveguide photodetector,*" *Optics Express*, Vol. 15, Issue 10, pp. 6044-6052, (2007)
- [15] Y.-H. Kuo, H.-W. Chen, J. E. Bowers, "*A hybrid silicon evanescent electroabsorption modulator,*" *Optical Fiber Communications Conference*, (2008)



## **Chapter 2 - Silicon Evanescent Device Design, Fabrication, and Proof of Concept**

The silicon evanescent device structure consists of a III-V epitaxial active layer structure bonded to a silicon waveguide fabricated on a silicon on insulator (SOI) wafer. The optical mode lies primarily in the silicon waveguide region while part of the mode lies in the upper III-V region, as shown in Figure 2.1. The high modal overlap in the silicon region allows for efficient coupling into passive regions where the III-V layer is etched off, such as distributed feedback mirrors that may exist outside the gain region of the device, or other devices in a photonic integrated circuit that are composed entirely of silicon, such as modulators, multiplexers, etc. The close proximity of the III-V region, and in particular the quantum wells, to the silicon allows for efficient evanescently coupled gain. This chapter begins with a discussion on the design of this waveguide structure in the context of semiconductor lasers. Next, we describe the fabrication of the silicon evanescent lasers. This includes silicon waveguide processing, wafer bonding, and the processing of III-V materials after bonding. The chapter is concluded with a demonstration and brief analysis of optically pumped silicon evanescent lasers as a proof of concept of the device structure [1][2].

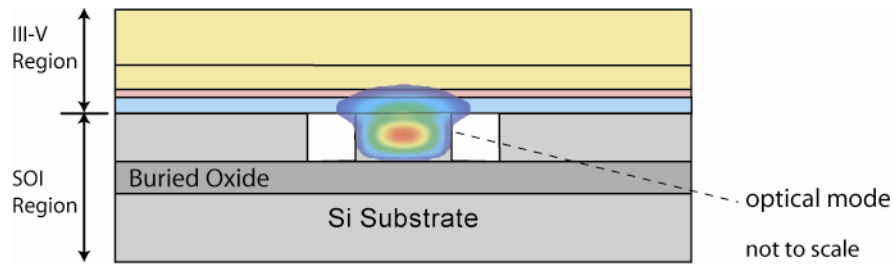


Figure 2.1 – Silicon evanescent device concept.

## 2.1 – Silicon Evanescent Waveguide Design

Several things are important when designing the waveguide for silicon evanescent lasers. First, we need to ensure that we have enough optical mode overlap with the active region to achieve sufficient optical gain for lasing. Second, we want to maximize the overlap in the silicon region such that the device can easily couple to non-hybrid regions that may help form the cavity, such as silicon gratings for distributed Bragg grating lasers, or other photonic devices on silicon. Finally, the waveguide design strongly affects the minimum bend radius a waveguide can undergo before bend loss becomes an issue. This factor is not important for linear lasers, but plays a large role in ring and racetrack lasers and will be discussed in Chapters 4 and 6.

We define the optical mode overlap, or confinement factor, in a given region in the transverse plane  $(x,y)$  as [3]:

$$(Eq - 2.1) \quad \Gamma = \frac{\iint_{region} E(x, y)^* E(x, y) dx dy}{\iint E(x, y)^* E(x, y) dx dy}$$

where  $E(x,y)$  is the electric field profile of the optical mode over the x-y plane. The confinement factor is a key design parameter for designing silicon evanescent lasers since it helps relate the amount of interaction the mode has with the gain material and helps give a ball park value for butt-coupling between hybrid and non-hybrid waveguide regions.

The threshold modal gain condition states that the lasing threshold occurs where the round trip gain equals the round trip losses. These losses originate from absorption and scattering during propagation through the waveguide and light coupled out of the cavity at facets or output couplers. For linear cavity lasers, this condition is expressed [4]:

$$(Eq - 2.2) \quad \langle g_{th} \rangle = \Gamma_{Quantum\ Well} g_{th} = \langle \alpha_i \rangle + \langle \alpha_{mirror} \rangle$$

$$(Eq - 2.3) \quad = \langle \alpha_i \rangle + \frac{1}{L_{cavity}} \ln \frac{1}{\sqrt{r_1 r_2}}$$

where  $g_{th}$  is the material gain at threshold, and  $\langle \alpha_i \rangle$  is the modal propagation loss. These values are on the order of  $1000 \text{ cm}^{-1}$  and  $16 \text{ to } 40 \text{ cm}^{-1}$  for typical III-V lasers [5], respectively. The mirror loss,  $\langle \alpha_{mirror} \rangle$ , consists of the two facet reflectivities,  $r_1$  and  $r_2$ , and the cavity length,  $L_{cavity}$ . The facet reflectivity is roughly 0.53 ( $R = 0.3$ ), between silicon and air based on Fresnel reflection [6]. The cavity length,  $L_{cavity}$ , is

designed to be  $\sim 800 \mu\text{m}$  long in order to keep the mirror loss below or equal to the modal loss. Substituting these values into Equation 2.2 and solving for  $\Gamma_{\text{Quantum Well}}$ , we find that the confinement factor in the quantum well,  $\Gamma_{\text{Quantum Well}}$ , should be at least 3% to achieve lasing. Although this condition is very rough, it gives us a good starting point on how to design these lasers. Ideally, there is an optimum design where confinement factors for the III-V and the silicon regions are decided to yield the desired lasing performance.

The 1-D layer structure is shown in Figure 2-2 along with the index profile, and mode amplitude profile of this structure. The mode has two lobes, with the main lobe lying in the silicon waveguide region, and the small second lobe lying in the SCH and active region. A thin N-type InP region with low index lies between these two regions and is used in this structure for vertical carrier confinement and as a current injection layer for electrically pumped devices. It is kept thin enough, that efficient evanescent coupling between the active region and silicon region can be achieved while being thick enough that current can flow through this layer without adding a substantial amount of series resistance.

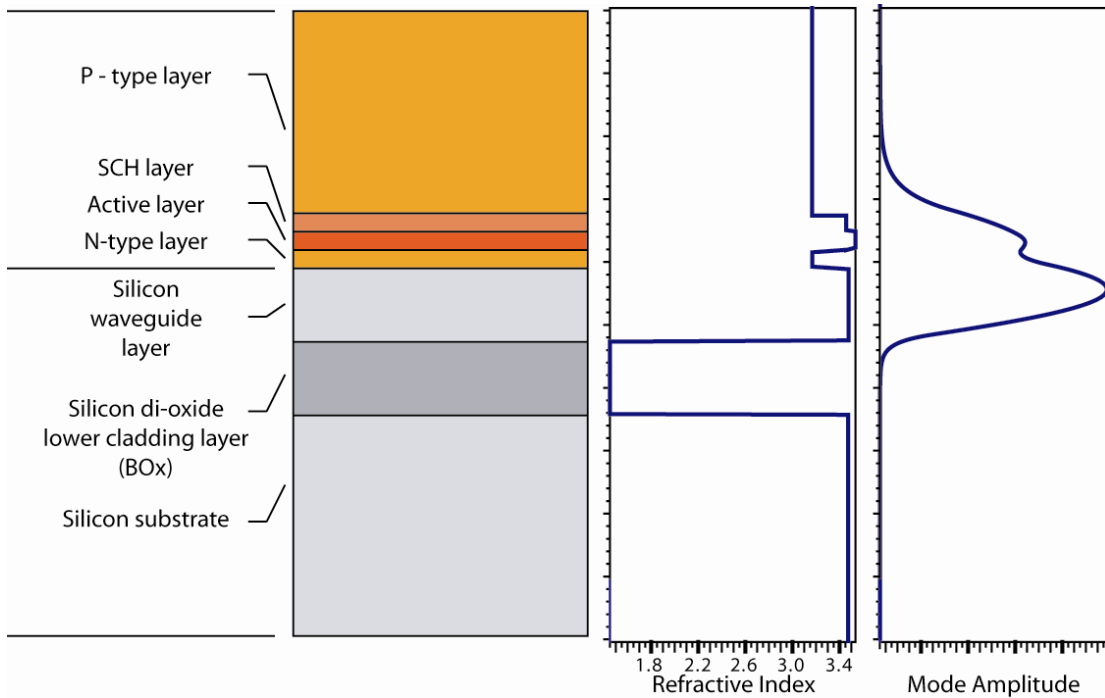


Figure 2.2 – A 1-D diagram of the layer structure with the refractive index and the 1-D mode amplitude profile.

The waveguide has an upper waveguide cladding of P-type InP and a lower waveguide cladding of silicon dioxide. The silicon dioxide layer has an index of  $\sim 1.45$  and needs to be sufficiently thick enough to prevent the evanescent coupling of the optical mode in the waveguide layer to the substrate modes. In this work we use a minimum buried oxide (BOx) thickness of  $1 \mu\text{m}$ , based on optical mode calculations of the evanescent field penetration depth, to maintain low loss.

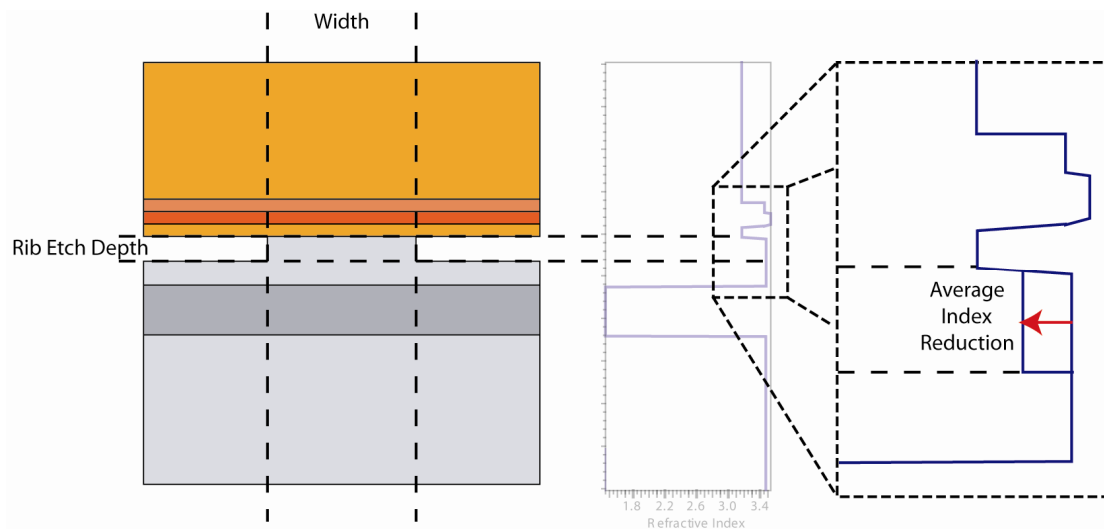


Figure 2.3 – A Diagram of the layer structure with the addition of lateral confinement in the silicon region. The average index profile is shown to the right.

Before diving into a full parameter scan of confinement factors with a mode solver, let's develop a qualitative understanding of how to manipulate the mode in the vertical direction. It is well understood that the mode profile will occupy regions with higher index [7]. Without lateral confinement, the confinement factor over the silicon region, and the quantum well region is modified by altering the silicon waveguide height and the SCH thickness where taller silicon heights pull the mode into the silicon, or greater SCH thicknesses pull the mode into the III-V region. We use a silicon height of 700 nm and an SCH thickness of 500 nm for optically pumped devices and 250 nm for electrically pumped devices and throughout this thesis. This leads to confinements in the silicon region and quantum well region of about ~60-45% and 3 - 8%, respectively. The remaining mode lies in the III-V region outside of the quantum wells.

Transverse optical confinement is achieved by etching a rib waveguide into the top silicon waveguide layer as shown in Figure 2.3. This leads to a reduction in the average lateral index as seen in the index profile vertical cross section (Figure 2.3). The strength of this reduction increases as rib waveguide width narrows. The narrower a waveguide is etched, the lower the average index in the silicon region, pushing the mode out to the III-V region.

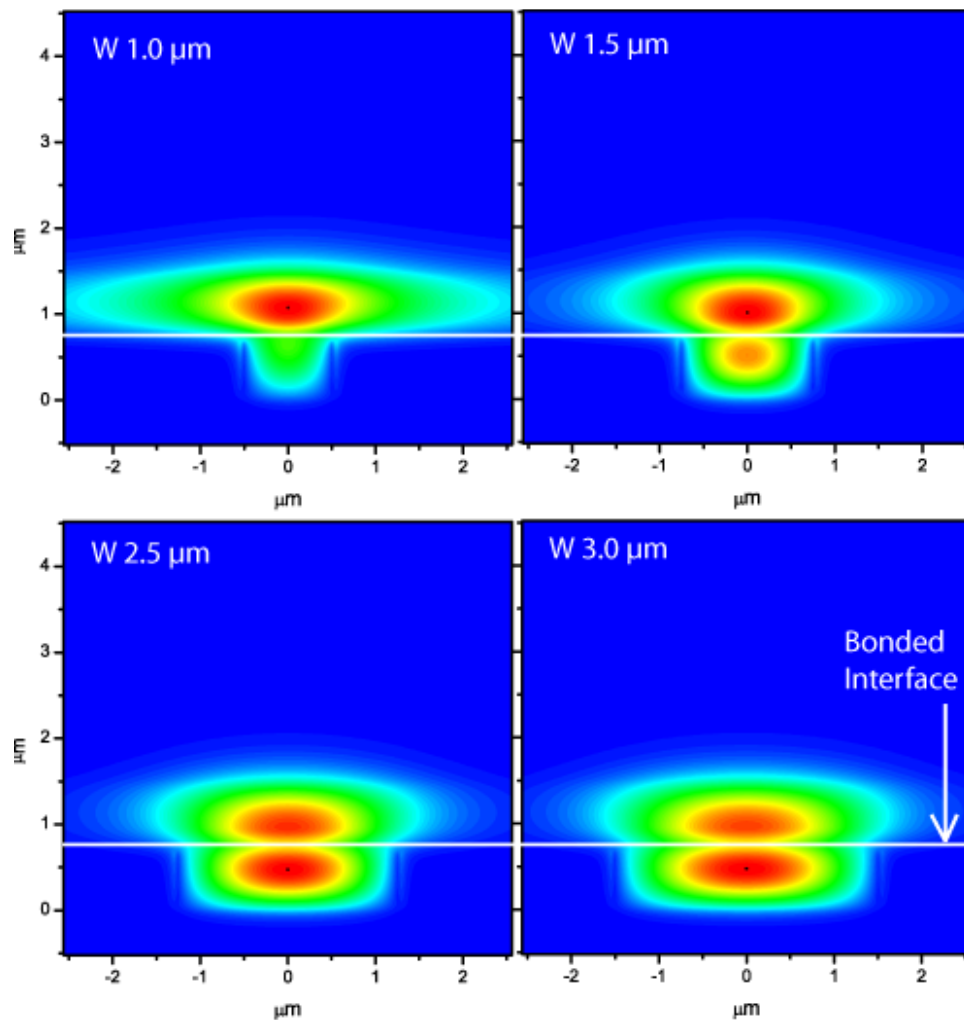


Figure 2.4 – Calculated mode profiles for fixed waveguide heights of  $0.7 \mu\text{m}$  and rib etch depths of  $0.5 \mu\text{m}$ . The waveguide width is varied from  $1.0 \mu\text{m}$  to  $3.0 \mu\text{m}$  to show the change in optical mode with waveguide width.

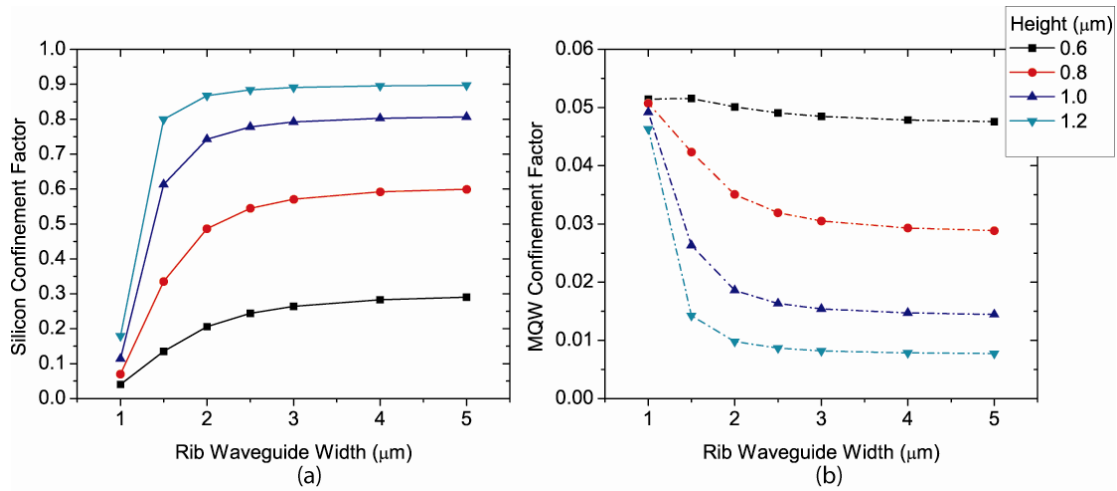


Figure 2.5 – (a) Silicon waveguide and (b) Multiple quantum well region confinement factors for an SCH thickness of 500nm and for various waveguide heights and waveguide widths.

Figure 2.4 shows four calculated mode profiles with fixed waveguide heights and rib etch depths of 0.7 μm and 0.5 μm, respectively. The waveguide widths varied from 1.0 μm to 3.0 μm. It can be seen that for the widest waveguide width, the mode lies primarily in the silicon region. As the waveguide width gets narrower, the mode is pushed into the III-V region. Since the III-V region lacks lateral confinement, the mode gets substantially wider. Figure 2.5 shows the calculated confinement factors for the silicon region and the quantum well regions as a function of waveguide width and height. Again, it can be seen that the narrower widths yield higher quantum well confinement factors while the silicon confinement factors are reduced. As the waveguide width becomes wider, the mode moves towards the silicon region and saturates to a value equivalent to the 1-D slab structure. The ability to control the optical mode with the silicon waveguide is a key feature of this platform. Take for



example, if you wanted to integrate amplifiers and lasers with a single chip. Amplifiers are typically designed with low quantum well confinement factors in order to achieve high saturation powers [8], [9], while lasers are designed with higher confinement factors to achieve lower threshold currents. This can still be realized on a single die with a single bond by having narrow waveguide widths in the laser region, while tapering out the waveguide in amplifier regions. The fact that the optical mode is defined by the silicon and can be tailored across the chip, allows major flexibility for photonic integrated circuit design without adding additional complexity to the fabrication process.

## *2.2 Device Fabrication*

This section will give an overview of processing used to fabricate the various devices reported on in this dissertation. The main flow of the device processing can be divided into 4 major steps as shown in Figure 2.6. First, the pre-bonding process consists of the formation of silicon waveguides on a silicon-on-insulator wafer and the growth of the III-V epitaxial layer structure on the InP substrate. Next, wafer bonding is conducted and the substrate of the InP is removed such that the III-V epitaxial layer structure is transferred to the top surface of the silicon-on-insulator wafer. In the third major step, the post bonding processing is done on the III-V layers in order to manipulate the flow of current in the hybrid regions through the etching of mesas, deposition of contacts, and definition of insulating areas through proton

implants and dielectric layer deposition and patterning. In addition, III-V materials are removed from passive regions. The final step is the sample preparation of the device for testing and characterization. This includes dicing, facet polishing, and the deposition of high reflection or anti reflection coatings, depending on the device being tested. Since this step is unique from device to device, it is not discussed in this section, but will be mentioned in the individual device sections.

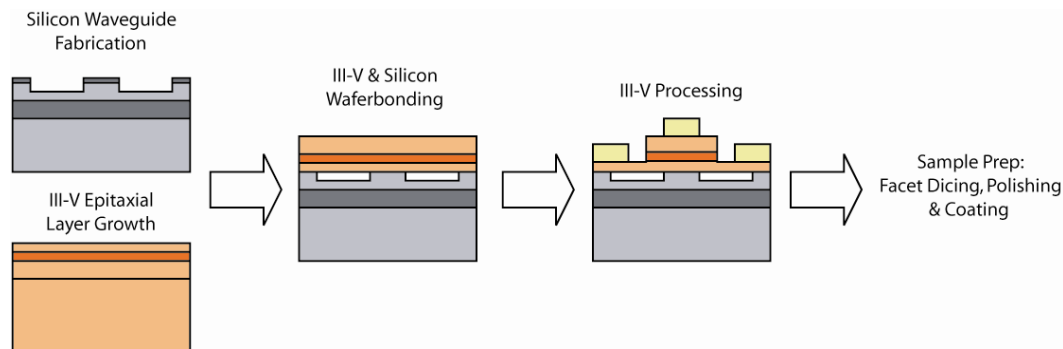


Figure 2.6 – Basic silicon evanescent laser process flow.

### 2.2.1 - Silicon Processing

Since a lot of the work reported in this dissertation was in collaboration with Intel Corporation, most of the silicon processing (devices in Chapters 2, 3, and 4) was done in an Intel fabrication facility. This section will briefly describe the process used at UCSB to make silicon rib-waveguides. Although the exact etch conditions used at Intel may vary slightly, the overall process is similar.

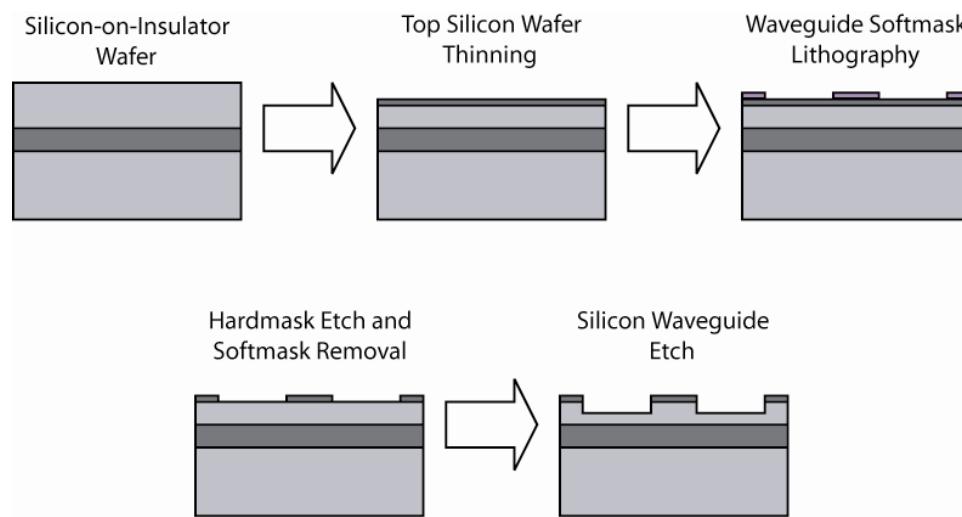


Figure 2.7 – Silicon waveguide fabrication process flow.

Silicon-on-insulator wafers consist of the following structure: a silicon substrate, a thin silicon dioxide layer ( $\sim 1 \mu\text{m}$  for photonic applications), and a top layer of silicon. Figure 2.7 shows the fabrication process flow. Silicon waveguide processing is done by first thinning the top silicon layer to the desired waveguide height through thermal oxidation. During thermal oxidation, the top silicon is consumed during the formation of an additional silicon dioxide layer at the surface. Next, projection lithography is used to make a soft mask of the waveguides. The soft mask is transferred to the top silicon dioxide layer by inductively coupled plasma etching. The photo-resist is then removed by burning the photo-resist in an  $\text{O}_2$  plasma descum chamber followed by a chemical photo resist removal. Finally, the silicon rib waveguides are dry etched by inductively coupled plasma to ensure smooth vertical

sidewalls and hence, low loss waveguides. The silicon is now ready for wafer bonding.

### *2.2.2 Wafer Bonding*

Since the lattice spacing of crystalline silicon (5.431 Å) and indium phosphide (5.8687 Å) has a 7.5% mismatch, wafer bonding is used to transfer the thin InP based active region to the silicon on insulator wafer. Direct wafer bonding is commonly used to mate lattice mismatched semiconductors such as GaAlAs & GaP for high power LEDs, InGaAsP, AlAs & GaAs for improved mirror reflectivity in long wavelength VCSELS, and InGaAsP & AlGaAs for high  $T_0$  lasers [10]. This process consists of the following steps. First a thorough cleaning of the sample surface is done to remove all semiconductor particles that were generated during dicing or cleaving and to remove all organics on the surface, followed by a chemical surface treatment removing any surface oxide states or other stable surface states. The samples are then placed in physical contact with each other and undergo spontaneous bonding and are held together with Van der Waals forces [10]. This bond is relatively strong, depending on the two material systems being bonded, but is further strengthened through a high temperature anneal (typically 600 °C or higher) while applying pressure on the bonded sample. The high temperature anneal results in chemical changes and re-crystallization at the bonded interface, while the pressure on the sample compensates for any waviness or surface roughness and ensures greater surface area contact between the two materials. The substrate of one of the

material systems is then removed by using a wet etch resulting in the transfer of one epitaxial layer structure to another.

The thermal expansion coefficient mismatch of silicon ( $\alpha_{Si} = 2.6 \times 10^{-6} /K$ ) [11] and InP ( $\alpha_{InP} = 4.8 \times 10^{-6} /K$ ) [12] requires the use of a low temperature wafer bonding technique in order to preserve the quality of the transferred epitaxial layers. Equation 2.4 describes the thermal mismatch stress of the bonded wafers as follows [reference]:

$$(Eq - 2.4) \quad \sigma = \frac{E}{1-\nu^2} \left\{ \frac{\frac{E_{InP}}{1-\nu_{InP}^2} \alpha_{InP} h_{InP} + \frac{E_{Si}}{1-\nu_{Si}^2} \alpha_{Si} h_{Si}}{\frac{E_{InP}}{1-\nu_{InP}^2} h_{InP} + \frac{E_{Si}}{1-\nu_{Si}^2} h_{Si}} - \alpha \right\} \Delta T$$

where  $\alpha$  is the thermal expansion coefficient,  $h$  is the thickness of the substrate,  $E$  is the Young's modulus,  $\nu$  is the Poisson's ratio, and  $\Delta T$  is the difference the bonding temperature and room temperature. This equation is used by Pasquariello *et al.* to express the maximum sheer stress in the <110> direction, the maximum slip system between the alternating indium and phosphide {1,1,1} planes, as a function of temperature as follows [13]:

$$(Eq - 2.5) \quad \tau_{Sheer} = \frac{2}{\sqrt{6}} \sigma$$

The critical stress required to generate dislocations in InP is empirically formulated by Pasquariello *et al.* using the theory of stress induced dislocation generation [13] is expressed in Equation 2.6.

$$(Eq - 2.6) \quad \tau_{critical} = 898e^{\frac{5934.17}{T}}$$

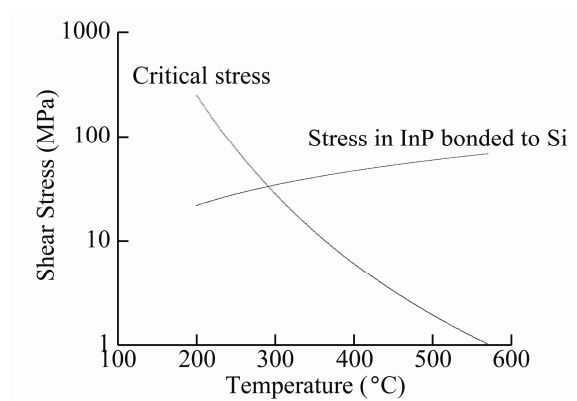


Figure 2.8 - Plot of critical dislocation generation stress in InP and shear stress between InP bonded to silicon versus temperature [Pasquariello *et al.*, reference [13]]

Figure 2.8 shows a plot of the critical stress and the shear stress as a function of temperature. In order to prevent the generation of dislocations in the InP, the bonding temperature must be kept below 300 °C. Normarski mode microscope images of the surface of III-V epitaxial layers transferred to silicon at (a) 600 °C and (b) 250 °C are shown in Figure 2.9. It can be seen that the sample bonded at higher temperatures shows cross hatching and waviness in the III-V film indicating stress within the film. The low temperature sample, on the other hand, shows a pristine surface, indicating a high III-V film quality. In order to maintain high bond strengths, a low temperature oxygen plasma assisted wafer bonding process, consisting of an O<sub>2</sub> plasma based surface activation prior to the mating of the two surfaces followed by a 250 °C anneal, was pursued. This temperature was raised to 300 °C during device processing in order to further increase bond strength, while not exceeding the 300 °C limit shown in Figure 2.8.

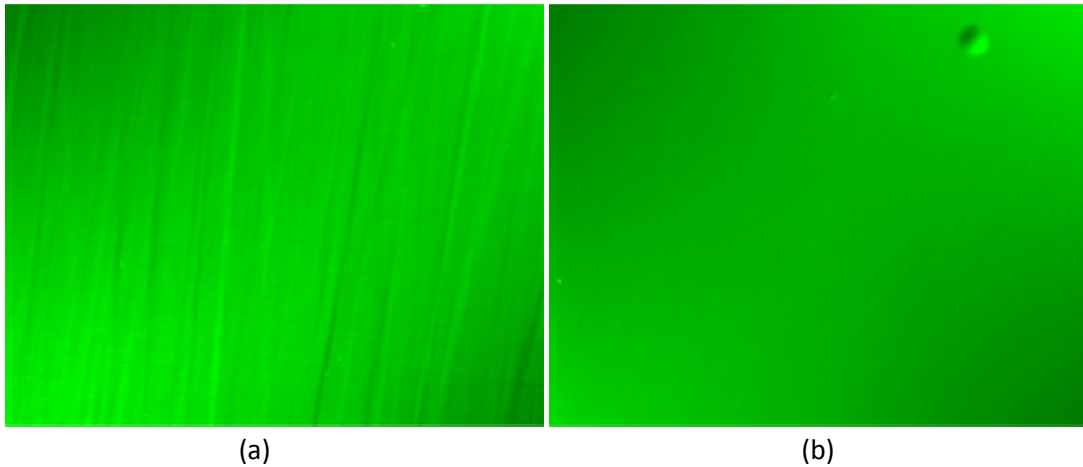


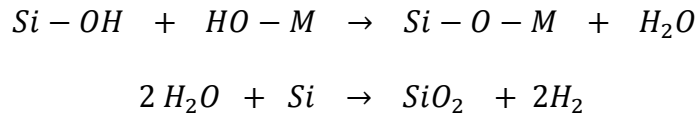
Figure 2.9 Nomarski microscope images, showing the surface roughness of the transferred III-V surface at bonding temperatures of (a) 600 °C and (b) 250 °C.

The low temperature oxygen plasma assisted wafer bonding process begins with the same cleaning processes as the direct bonding approach. This is done by solvent cleaning the silicon and III-V with acetone, isopropanol, and deionized water. Next the samples are placed in a solution of Tergitol:H<sub>2</sub>O (5 drops: 1 liter) and are physically wiped with cleanroom grade q-tips to remove particles. Tergitol is an organic detergent that assists in the removal of surface particles. Next the samples are rinsed in deionized water and inspected under the microscope for particles. The swab and inspect process is repeated until the samples are particle free.

The silicon dioxide hard mask layer used during silicon waveguide fabrication is then removed by using an HF dip. The III-V material is typically grown with a 200 nm InGaAsP cap layer to protect the surface quality during handling and cleaving. This layer is removed with a chemical wet etch and the samples undergo another swab

and inspect step to remove any particles that may have been accumulated during the acid treatments. A final organic clean is done by conducting a 30 minute Ozone clean of the surface.

The samples are then treated with an O<sub>2</sub> Plasma where a thin (<5 nm), highly strained, and highly reactive hydrophilic oxide is formed on the surface. The samples are dipped in deionized water and their surfaces are terminated with OH groups. At this point, the samples are placed in physical contact with each other and spontaneous bonding occurs by the formation of hydrogen bonds. The samples are place in a Suss SB-6, a commercial wafer bonder, at 300 °C with 1.5 MPa of pressure for 12 hours. During this annealing process, the chemistry of the bond changes in a two step process as follows [14]:



where M is either indium, or phosphide. The chemical change in the bond, leads to the generation of water. The water then oxidizes the silicon and outgases hydrogen. The outgassed hydrogen at the bonded interface leads to void formations on un-patterned surfaces as shown in Figure 2.10. The rib waveguides in the silicon act as in-plane out-gassing channels, allowing the hydrogen released during the bond to flow out of the sample. Void formation still occurs in regions far from the channels (~150 μm) but do not affect device performance since they are away from device regions. The void density can be reduced by conducting the annealing in vacuum and



by increasing the time to 18 hours to allow for hydrogen diffusion out of the bonded interface.

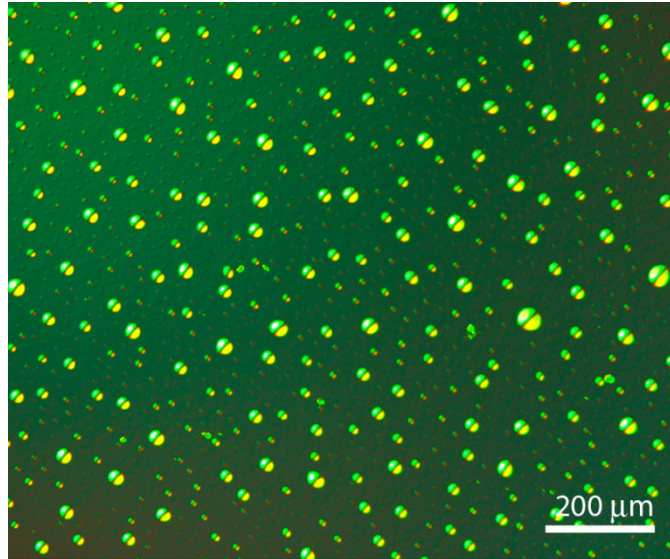


Figure 2.10 – Nomarski microscope images, showing void formation on unpatterned bonded wafers

Although the use of in-plane out-gassing channels is useful to demonstrate devices, it does place constraints on how the waveguides must be laid out on the silicon such that the channel density is high enough to allow for sufficient H<sub>2</sub> removal. A complete study was not done to find the minimum density required to achieve good bonding, but a general design rule was of a maximum spacing of 125 μm per channel was used .

Next, the substrate of the InP is removed in a solution of HCL:H<sub>2</sub>O. This selective etch is designed to stop at the top InGaAs etch stop/p contact layer, protecting the AlGaInAs epitaxial layer structure. To prevent the lateral etching of the epitaxial

layer structure, the sample is mounted onto a glass slide with mounting wax or “crystal bond”. The sample is mounted silicon side down. Mounting wax is spread along the four edges of the sample as shown in Figure 2.11.

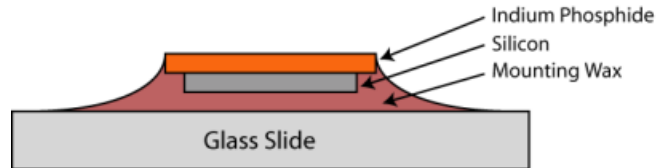


Figure 2.11: Cross section diagram of bonded sample mounted to a glass slide for sidewall protection during substrate removal.

The sample is reheated to remove it from the glass slide and undergoes a final solvent clean to remove the residual mounting wax and prepare the sample for device processing.

### *2.2.3 Post-bond Device Process Flow*

The post-bond device process flow is shown in Figure 2.12. Once the wafers are bonded, mesas need to be etched above the waveguide. This is done by first depositing a thick SiN hard mask on the top III-V surface of the bonded sample. Next the SiN hard mask is patterned with a photo lithographically defined soft mask and is etched with  $\text{CF}_4$  in an RIE etch chamber. Next, the photo resist is removed and the P mesas are etched in a two step etch processes. First, a dry etch is done in a reactive ion etch (RIE) chamber using  $\text{CH}_4/\text{H}_2/\text{Ar}$ . This etch depth is monitored using laser interferometry such that the etch goes through the top InP cladding region, but stops within the SCH/QW region. A wet etch is used to finish the p mesa etch using a solution of  $\text{H}_2\text{O}_2:\text{H}_3\text{PO}_4:\text{H}_2\text{O}$ . This etch is selective against InP and is designed to etch

through the AlGaInAs materials in the SCH and QW such that the bottom InP layer is exposed. Next, Ni/Ge/Au/Ni/Au N contacts are patterned, deposited, and lifted off via a Bi-layer liftoff process. The SiN hard mask is then removed and Pd/Ti/Pd/Au P contacts are patterned, deposited, and lifted off. The p contact not only serves as a path for current to flow into the mesa, but it also serves as a mask above the waveguide such to prevent the implantation of protons above the waveguide, effectively defining the current path through the mesa. The contacts are then annealed for activation on a strip annealer at 320 °C for 30 seconds and TLM patterns are measured to ensure good contact resistances. Next, a bi-layer structure of PMGI and photo-resist are used to create a mask for proton implant. This mask protects the exposed n regions from implantation maintaining the conductivity of those regions. The samples are then sent out for proton implantation. Upon the return of the samples, the proton implant mask is removed and a dielectric electrical isolation layer is deposited on the surface. Most of the devices fabricated in Chapters 3 and 4 utilize a thick layer of SiN for this insulation layer, while the final device design (Ch. 5) utilizes SU-8 since it is a low k dielectric to lower the device capacitance and it also adds structural integrity to the structure for improved facet polishing. Vias are patterned into this isolation layer and Ti/Au probe pads are patterned and deposited on the sample. The deposition of this layer is done while rotating the sample at an angle as to ensure good sidewall coverage. This completes

the processing and the samples are now ready for device specific sample prep, and/or on-chip device characterization.

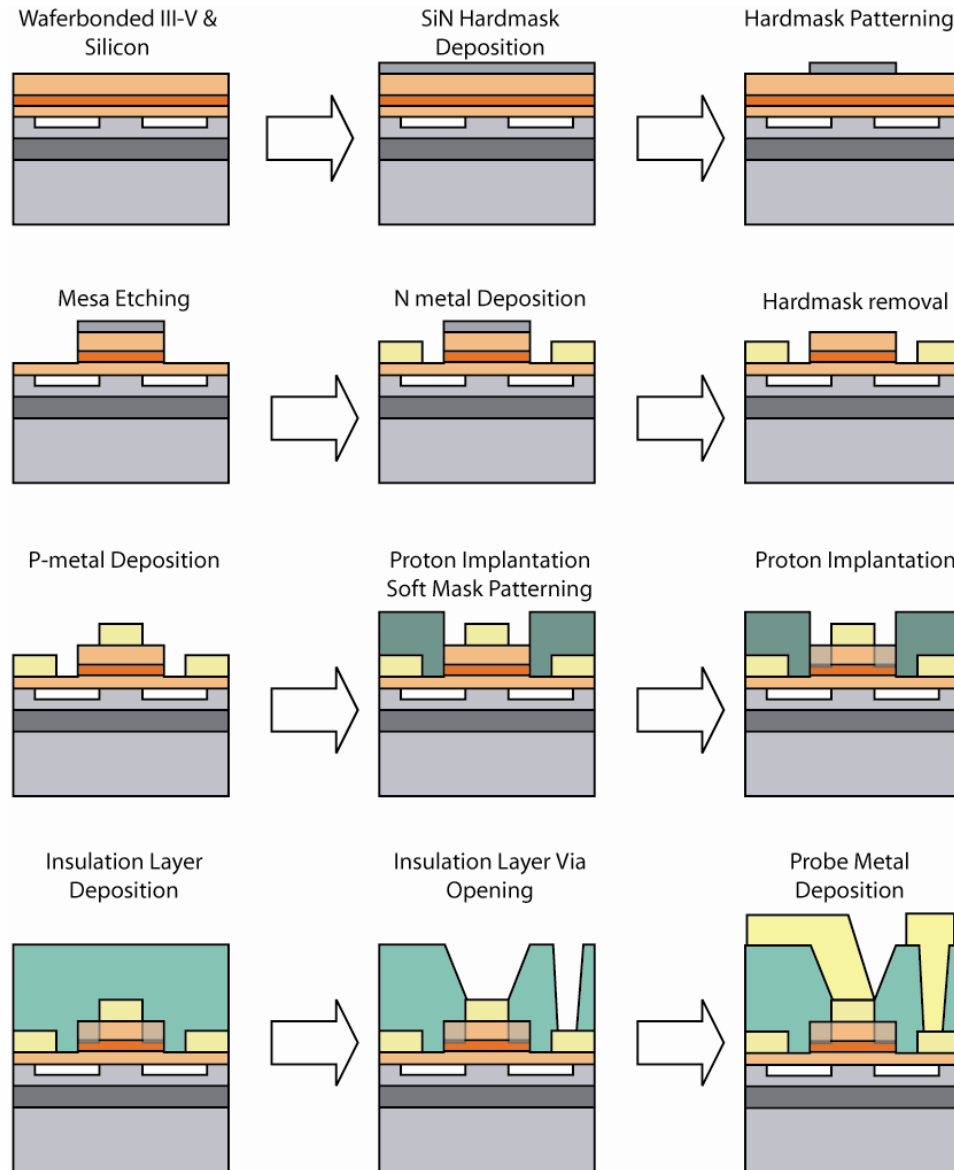


Figure 2.12 – III-V post bond process flow.

## 2.3 – Proof of Concept – Optically Pumped Silicon Evanescent Lasers

Optically pumped silicon evanescent lasers were first demonstrated as a proof of concept for the silicon evanescent waveguide architecture. This chapter discusses the device structure and design of the active region, the experimental methods used to test the devices, and discusses the pulsed [1] and continuous wave [2] lasing performance of these devices.

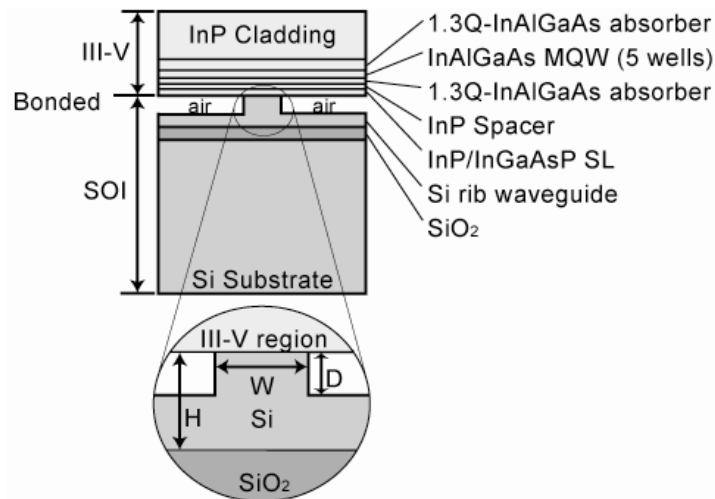


Figure 2.13 – The optical pumped silicon evanescent laser device structure cross section

### 2.3.1 - Device Structure

Figure 2.13 shows a cross sectional diagram of the optically pumped device. The device is the simplest of all SELs and consists only of a III-V active region structure designed for optical pumping bonded to silicon rib waveguides.

The III-V active layer structure is shown in Table 2.1. The structure is designed to be optically pumped from the top surface through the InP cladding in the 900 nm to 1275 nm wavelength range, with the pump light being absorbed in the SCH region. The pump light field intensity decays as it is absorbed, generating a carrier profile in the SCH. This carrier distribution causes the carriers to flow from the SCH into the quantum wells where they recombine, generating spontaneous emission and optical gain at 1550 nm. A thin super lattice region is used in this structure between the lower SCH InP region and the InP bonding layer to prevent the propagation of defects from the bonded interface to the quantum wells [15].

<b>III-V Epitaxial growth layer structure</b>		
Name	Composition	Thickness
Etch stop layer	$\text{In}_{0.53}\text{Ga}_{0.47}\text{As}$	0.1 $\mu\text{m}$
Cladding	InP	1.5 $\mu\text{m}$
Upper SCH	$\text{Al}_{0.131}\text{Ga}_{0.34}\text{In}_{0.528}\text{As}$ , 1.3 $\mu\text{m}$	0.5 $\mu\text{m}$
Quantum Wells	$\text{Al}_{0.089}\text{Ga}_{0.461}\text{In}_{0.45}\text{As}$ , 1.3 $\mu\text{m}$ (6x)	10 nm
	$\text{Al}_{0.055}\text{Ga}_{0.292}\text{In}_{0.653}\text{As}$ , 1.7 $\mu\text{m}$ (5x)	7 nm
Lower SCH	$\text{Al}_{0.131}\text{Ga}_{0.34}\text{In}_{0.528}\text{As}$ , 1.3 $\mu\text{m}$	0.05 $\mu\text{m}$
Lower SCH barrier	InP	110 nm
Super Lattice	$\text{In}_{0.85}\text{Ga}_{0.15}\text{As}_{0.327}\text{P}_{0.673}$ (2x)	7.5 nm
	InP (2x)	7.5 nm
Bonding layer	InP	10 nm

Table 2.1 – Optically pumped III-V layer structure

### 2.3.2 Experimental set up and method

Figure 2.14 shows the experimental set up. The devices are pumped perpendicular to the top surface. The pump beam cross section should ideally be rectangular such that the entire device length of 600-900  $\mu\text{m}$  is pumped, and the width of the beam is

as closely matched to the device width as possible ( $\sim 1 - 4 \mu\text{m}$ ). A fiber coupled 980 nm laser diode and a 2 W 1250 nm fiber laser were used as optical pumps for pulsed and continuous wave operation, respectively. The pump light is first collimated and focused onto the top surface of the laser through a cylindrical lens forming a 0.916 mm by 12  $\mu\text{m}$  ellipse. The pump system was positioned with an XYZ stage. This system was placed on a sliding rail along with a top surface imaging system such that they could be interchanged easily.

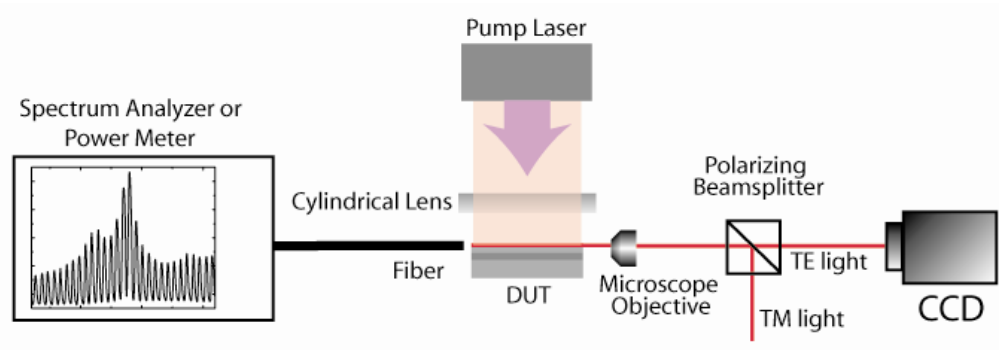


Figure 2.14 – The experimental setup for testing optically pumped silicon evanescent lasers

The light from the device is collected at one facet with a lensed fiber and routed to a spectrum analyzer or a power meter, depending on the measurement being made. The other facet is imaged with an infrared imaging system. The system consists of an 80X microscope objective, with a modified Navitar telescoping zoom system mounted on a Hamamatsu infrared camera. The Navitar zoom system's front lens was removed such that higher magnifications could be achieved with the 80X microscope objective. In addition, a polarizing beam splitter can be placed in the

optical path such that TE or TM polarization images can be observed independently. This imaging system has proved to be quite useful for testing these devices since it allows us to assess the waveguide facet quality, ensure we have proper alignment during other experiments in which we launch light from the fiber into the waveguide, and give us an experimental way to verify which mode lases and if the waveguide is single mode.

### *2.3.3 - Pulsed Operation*

The 980 nm optical pump was driven at 1 microsecond pulse width and 4% duty cycle. This allowed us to operate the optical pump with peak powers of  $\sim 1\text{W}$ , far above the 300 mW maximum continuous wave operating power. Figure 2.15 shows the computed optical mode and the near-field image of lasing optical mode, showing good qualitative agreement. The lasing mode was TE with a TE/TM ratio of  $> 20\text{ dB}$ .

Figure 2.16 shows the peak single sided fiber coupled output power of the laser as a function peak pump power (Light vs. Light curve). The lasers lased up to  $20\text{ }^\circ\text{C}$  with a maximum fiber coupled power of 1.4 mW and a minimum threshold 30 mW. The single output differential quantum efficiency is approximately 3.2 % at  $12\text{ }^\circ\text{C}$ , the total efficiency taking into account the light from both facets and the estimated 5 dB coupling loss is approximately 20 %. It is important to note that lasing only occurs in the optical mode defined by the Si waveguide region. In other words, slab modes in



the III-V region do not support lasing. This can be seen from the inset of Figure 2.15, which compares the light output for pumping in the two regions.

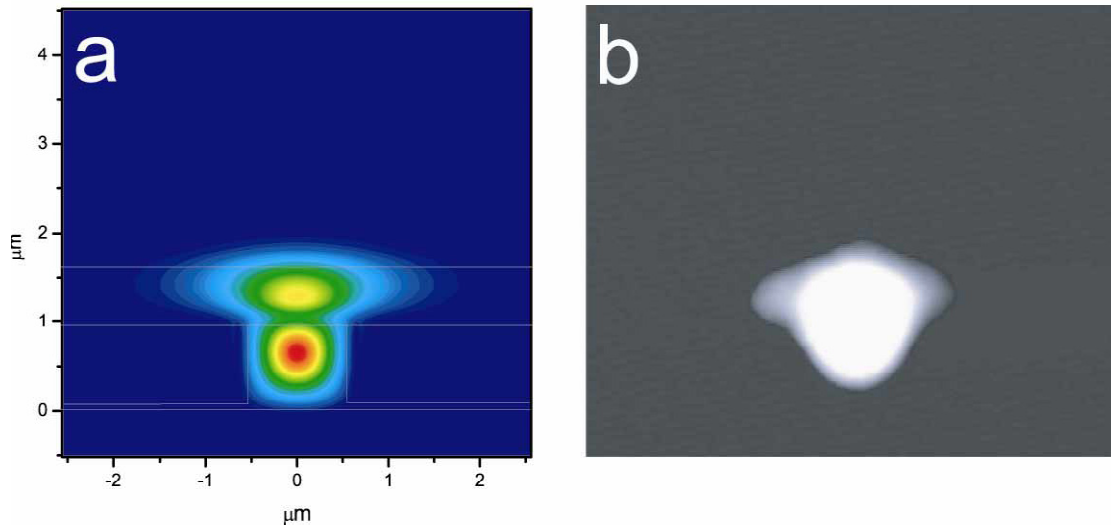


Figure 2.15 – a) The simulated optical mode superimposed over the waveguide structure. b) The nearfield image of the lasing optical mode.

Figure 2.17 shows the lasing spectrum at 1.4 times the threshold pump power and at a temperature of 12 °C. The optical spectrum consists of the expected Fabry-Pérot response for the 600  $\mu\text{m}$  long cavity, with a group index of 3.7. The devices were limited to pulsed lasing due to the maximum power available.

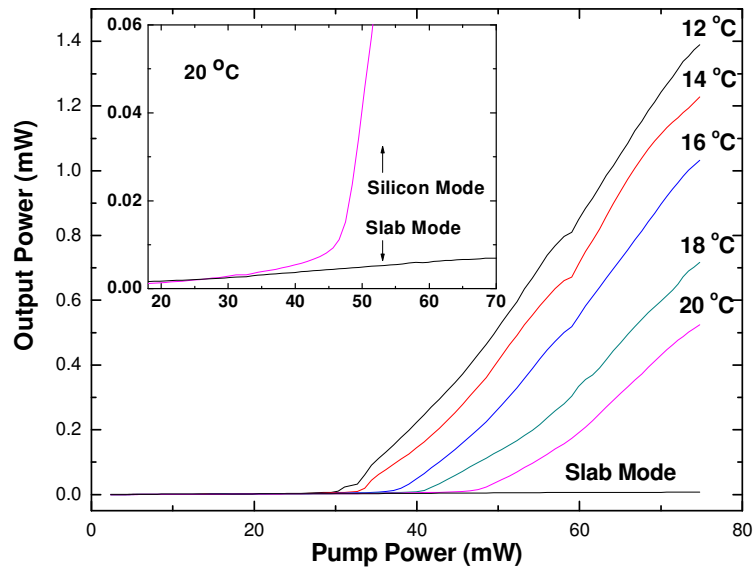


Figure 2.16 – Pulsed L-L curves as a function of temperature. (inset) L-L curve of device when pumped above the silicon waveguide and above the silicon slab without lateral modal confinement

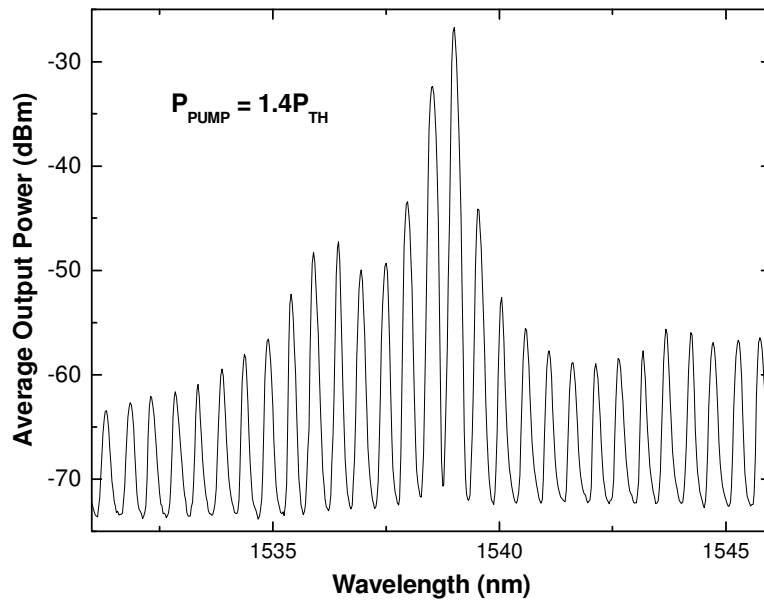


Figure 2.17 – Optically pumped pulsed lasing spectrum

### 2.3.4 - Continuous wave operation

Continuous wave operation was achieved by replacing the 980 nm laser diode with a 2 W fiber laser operating at 1250 nm. A second batch of devices was fabricated with a variety of waveguide widths such that their modal characteristics could be observed.

The lasing optical modes as a function of waveguide width with their corresponding simulated optical modes is shown in Figure 2.18. As you can see, for narrow silicon waveguide widths, the mode lies primarily in the III-V region and as the widths become wider and wider, the optical mode lies more and more in the silicon region, as predicted by simulations.

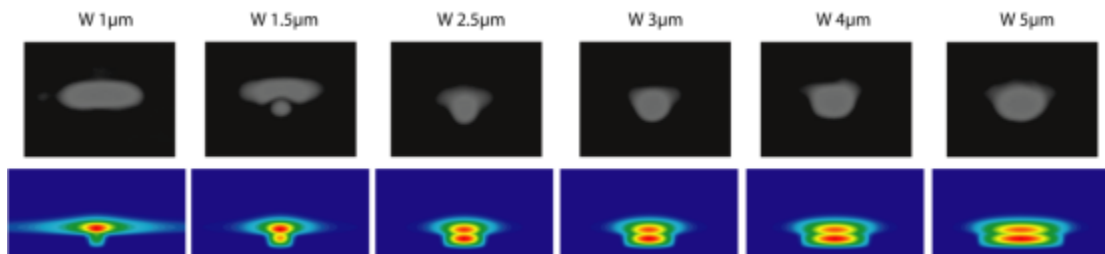


Figure 2.18 – Experimentally captured near field profiles of the lasing modes and their corresponding calculated mode profiles for various waveguide widths.

The lasers operated in continuous wave mode, with widths less than 1.5 µm operating with a single transverse mode, while wider widths lased with multiple transverse modes. Figure 2.19 shows the L-L curve of 1 µm waveguide width laser operating up to 30 °C. It can be seen that the L-L curve is relatively clean with very minimal kinks in its shape. The optical mode was observed throughout the various

operating conditions and showed stable lasing in the fundamental mode. The maximum fiber coupled laser output power was 0.9 mW. The total maximum output power including the output from both facets and coupling losses is approximately of 5 mW with a slope efficiency of 2.8%.

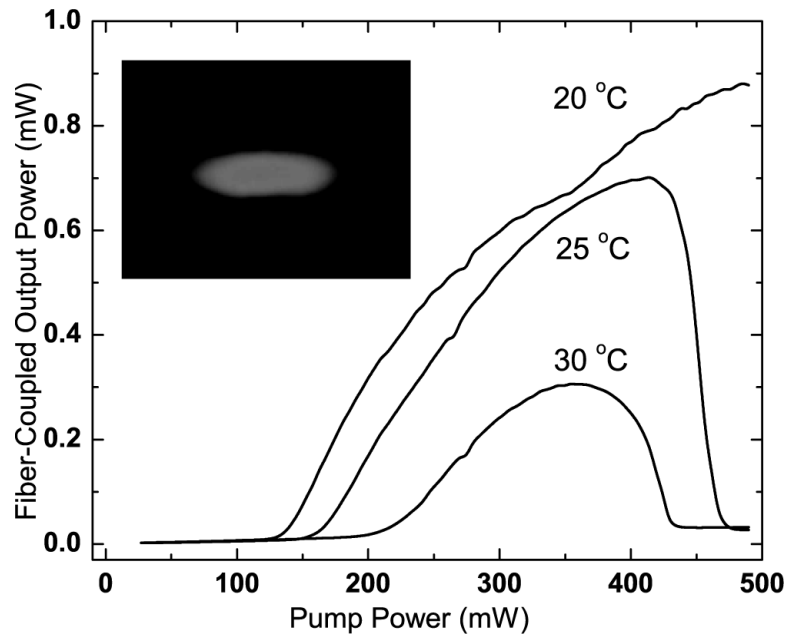


Figure 2.19 - L-L curve for a waveguide width of 1  $\mu\text{m}$  and the corresponding optical mode.

In Figure 2.20, a 4  $\mu\text{m}$  wide device is operating with a threshold pump power of 23 mW with a fiber-coupled maximum output power of 4.5 mW and a slope efficiency of 3% at 20  $^{\circ}\text{C}$ . The total maximum output power taking into account the light from both facets and the coupling losses of 5 dB is approximately 28 mW and the corresponding slope efficiency is 16%. The threshold increases from 23 to 105 mW between 20  $^{\circ}\text{C}$  and 60  $^{\circ}\text{C}$  and the structure exhibits a temperature coefficient of 27

K. The kinks in the LL curves are due to the multimode lasing with wide waveguide dimension. It is clearly shown from two different mode profiles in Figure 2.20 that higher modes are superimposed with a fundamental mode at the region II of the LL curve while only a fundamental mode is lasing at the region I.

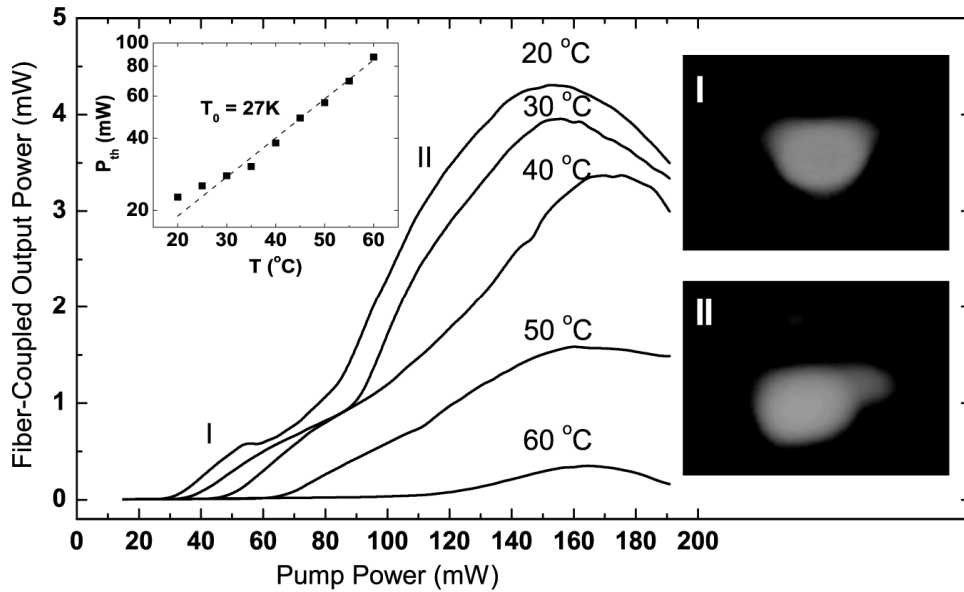


Figure 2.20 - L-L curve for a waveguide width of 4  $\mu\text{m}$  and the corresponding optical mode at two pump powers. Inset: Threshold as a function of temperature.

## 2.5 – Summary

The silicon evanescent waveguide structure is presented in this chapter. The device consists of a III-V gain structure bonded to a silicon on insulator rib waveguide to allow for evanescent coupling of the silicon waveguide mode into the III-V region to achieve gain. The design of optical mode characteristics is presented showing the ability to tailor the modal profile based on silicon waveguide definition. The fabrication of these devices is discussed. In particular, the transfer of the III-V active

layer from an InP substrate to a silicon wafer through a low temperature wafer bonding process is presented. Optically pumped lasers are demonstrated as a proof of concept for the device architecture. The lasers show continuous wave lasing up to 60 °C with a maximum fiber coupled output power of 4.5 mW at 20 °C. The lasers modal characteristics are shown to be strongly dependent on the silicon waveguide formation by comparing the lasing performance of regions with and without lateral confinement in the silicon, with the later showing no lasing. In addition, the experimental observation of the optical mode verifies that the optical mode can be manipulated across a single silicon chip by changing the waveguide width.

### *References*

- [1] H. Park, A. W. Fang, S. Kodama, and J. E. Bowers, “Hybrid silicon evanescent laser fabricated with a silicon waveguide and III-V offset quantum wells,” *Optics Express*, 13, 9460-9464, (2005)
- [2] W. Fang, H. Park, R. Jones, O. Cohen, M. J. Paniccia, J. E. Bowers, “A Continuous-Wave Hybrid AlGaInAs–Silicon Evanescent Laser,” *IEEE Photonics Technology Letters*, Vol. 18, Issue 10, pg 1143 – 1145 (2006)
- [3] L. A. Coldren and S. W. Corzine, *Diode Lasers and Photonic Integrated Circuits*, New York: John Wiley & Sons, Inc., pp. 432 (1995)
- [4] L. A. Coldren and S. W. Corzine, *Diode Lasers and Photonic Integrated Circuits*, New York: John Wiley & Sons, Inc., pp. 39 (1995)
- [5] L. A. Coldren and S. W. Corzine, *Diode Lasers and Photonic Integrated Circuits*, New York: John Wiley & Sons, Inc., pp. 45 (1995)

- [6] Yariv, and P. Yeh. *Photonics*, New York, Oxford University Press, pp. 196 (2007)
- [7] B.E.A. Saleh and M.C. Teich, *Fundamentals of Photonics*, New York: John Wiley & Sons, Inc., pp. 248 (1991)
- [8] K. Morito, S. Tanaka, S. Tomabechi, and A. Kuramata, "A broadband MQW semiconductor optical amplifier with high saturation output power and low noise figure". Semiconductor Optical Amplifiers and their Applications Meeting, PD1-1, San Francisco, CA June 30 2004.
- [9] P. W. Juodawlkis, J. J. Plant, R. K. Huang, L. J Missaggia, and J. P. "High Power 1.5 $\mu$ m InGaAsP-InP Slab-Coupled Optical Waveguide Amplifier," IEEE Photon. Technol. Letts. vol. 17, Feb, 2005.
- [10] Black, A. R. Hawkins, N. M. Margalit, D. I. Babic, A. L. Holmes, Jr., Y.-L. Chang, P. Abraham, J. E. Bowers and E. L. Hu, "Wafer Fusion: Materials Issues and Device Results," IEEE Journal of Selected Topics in Quantum Electronics, 3(3), 943-951, (1997)
- [11] *The Thermal Properties of Silicon*. Retrieved 25 January, 2008, <http://www.ioffe.rssi.ru/SVA/NSM/Semicond/Si/thermal.html>
- [12] *The Thermal Properties of Indium Phosphide (InP)*. Retrieved 25 January, 2008, <http://www.ioffe.rssi.ru/SVA/NSM/Semicond/InP/thermal.html>
- [13] D. Pasquariello, M. Camacho, F. Ericsson, and K. Hjort, "Crystalline Defects in InP-to-Silicon Direct Wafer Bonding," Jpn. J. Appl. Phys. Vol. 40, pp. 4837-4844, (2001)
- [14] U. Gosele, and Q.-Y. Tong, "Semiconductor wafer bonding," Annual Review of Materials Science, 1998, Vol. 28 Issue 1, p21
- [15] Karim, K. A. Black, P. Abraham, D. Lofgreen, Y. J. Chiu, J. Piprek, and J. E. Bowers, "Super lattice barrier 1528-nm vertical-cavity laser with 85 $^{\circ}$ C continuous-wave operation," IEEE Photon. Technol. Lett. 12, 1438-1440 (2000).

## **Chapter 3 - Electrically Pumped Silicon Evanescent Lasers - Fabry – Perot Lasers**

This chapter reports on the first electrically pumped silicon evanescent laser [1]. All results reported in this chapter utilize a Fabry-Perot laser topography. The first section of this chapter describes pulsed lasing operation with a simplified device structure used to validate the epitaxial layer design for current injection without lateral current confinement structures. The second section of the chapter presents the design of a lateral current confinement structure through the use of proton implantation and discusses continuous lasing operation. Lastly, this chapter presents a second generation electrically pumped laser structure for improved lasing performance and compares the thermal performance of the two generations.

### *3.1 - Pulsed Lasing Device Structure*

The device diagram for the first generation electrically pumped silicon evanescent lasers is shown in Figure 3.1. The III-V mesa regions were 75  $\mu\text{m}$  wide such that the p-contact could be easily probed from the top. N-contacts were placed 5  $\mu\text{m}$  away both sides of the mesa. In order to keep the device structure simple, no lateral current confinement was used in the p region. Instead, a 6  $\mu\text{m}$  wide current aperture was used at the center of a 300 nm thick silicon nitride isolation layer



under the p-contact. A scanning electron microscope image of the device is shown in

Figure 3.2.

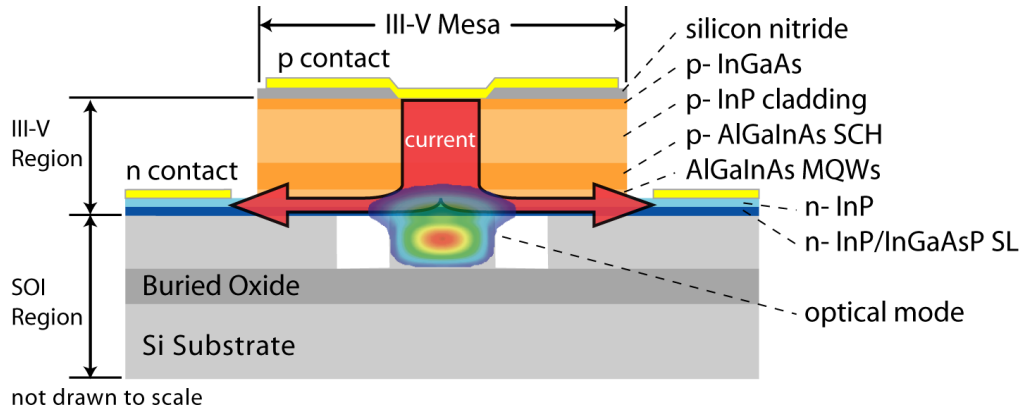


Figure 3.1 – The device cross section for the electrically pumped silicon evanescent pulsed laser.

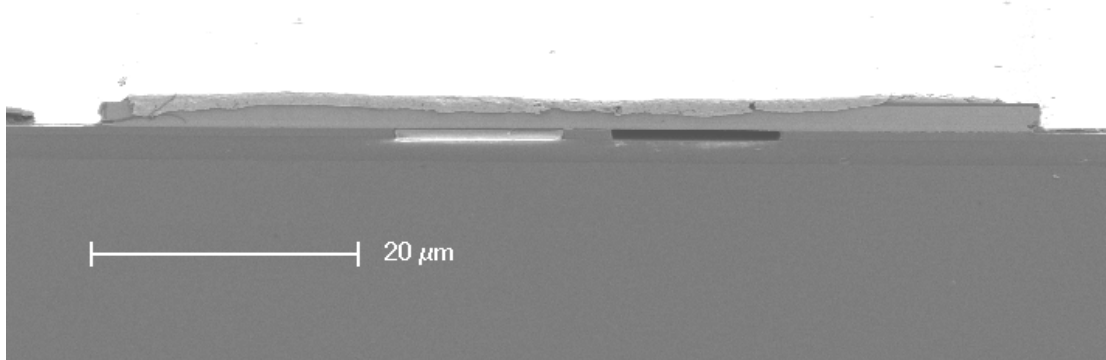


Figure 3.2 – Scanning electron microscope image of the electrically pumped silicon evanescent pulsed laser device cross section.

The buried oxide, silicon waveguide width, and height were  $2\ \mu\text{m}$ ,  $2\ \mu\text{m}$ , and  $0.76\ \mu\text{m}$  based on the criteria described in chapter 2. The rib was unintentionally etched all the way to the buried oxide, resulting in a strip waveguide. However, the confinement factors were not significantly perturbed in the deeply etch regime. The resulting silicon waveguide and quantum well confinement factors calculated using

Rsoft Beamprop were 74% and 5.5%, respectively. The laser's facets were diced and polished resulting in a total cavity length of  $\sim 780 \mu\text{m}$ . Other waveguide widths of  $1 \mu\text{m}$ ,  $1.5 \mu\text{m}$ ,  $2.5 \mu\text{m}$ ,  $3 \mu\text{m}$ , and  $3.5 \mu\text{m}$  were also fabricated and tested, but are not presented in detail here since the  $2 \mu\text{m}$  width devices showed the best overall performance. The variation of device performance due to facet polishing created scatter in the laser thresholds and differential efficiencies such that relationships between width and device performance could not be established.

### III-V Epitaxial growth layer structure

Name	Composition	Doping Concentration	Thickness
P contact layer	P-type $\text{In}_{0.53}\text{Ga}_{0.47}\text{As}$	$1 \times 10^{19} \text{cm}^{-3}$	$0.1 \mu\text{m}$
Cladding	P-type InP	$1 \times 10^{18} \text{cm}^{-3}$	$1.5 \mu\text{m}$
Separate Confinement Heterostructure	P-type $\text{Al}_{0.131}\text{Ga}_{0.34}\text{In}_{0.528}\text{As}$ , $1.3 \mu\text{m}$	$1 \times 10^{17} \text{cm}^{-3}$	$0.25 \mu\text{m}$
Quantum Wells	$\text{Al}_{0.089}\text{Ga}_{0.461}\text{In}_{0.45}\text{As}$ , $1.3 \mu\text{m}$ (9x)	undoped	10 nm
	$\text{Al}_{0.055}\text{Ga}_{0.292}\text{In}_{0.653}\text{As}$ , $1.7 \mu\text{m}$ (8x)	undoped	7 nm
N layer	N-type InP	$1 \times 10^{18} \text{cm}^{-3}$	110 nm
Super Lattice	N-type $\text{In}_{0.85}\text{Ga}_{0.15}\text{As}_{0.327}\text{P}_{0.673}$ (2x)	$1 \times 10^{18} \text{cm}^{-3}$	7.5 nm
	N-type InP (2x)	$1 \times 10^{18} \text{cm}^{-3}$	7.5 nm
N bonding layer	N-type InP	$1 \times 10^{18} \text{cm}^{-3}$	10 nm

Table 3.1 – Electrically pumped III-V epitaxial layer structure transferred to silicon.

The epitaxial layer structure used in the electrically pumped devices is shown in Table 3.1. It is similar to the optically pumped devices except for a few modifications. First, N layers (S dopant) and P layers (Zn dopant) were added to the structure such that current could be injected into the quantum well region. The region below the quantum wells (closer to the silicon waveguide after bonding) was doped N type since N type InP has lower optical loss and electrical resistance than P type for a given doping level [2]. This is important because this layer goes through the optical mode, and needs to be as low loss as possible to minimize threshold

currents. Additionally, this layer needs to be low resistance in order to minimize carrier spreading in the active region. The second change, was the removal of the lower SCH layer such that the quantum wells would be closer to the silicon waveguide, thereby increasing the active region confinement factor.

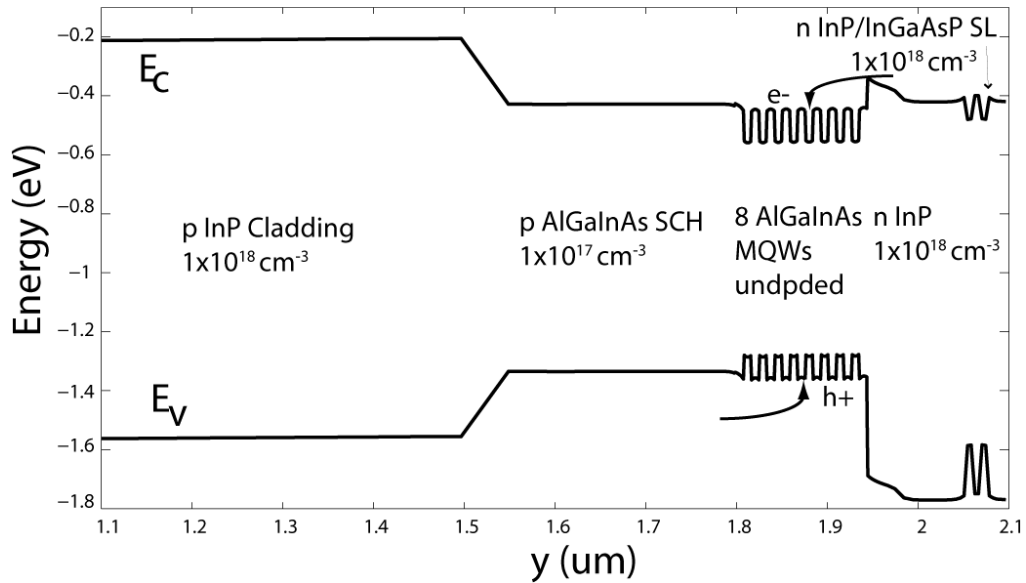


Figure 3.3 – The band diagram of the doped SEL epitaxial layer structure.

Figure 3.3 shows the band structure of the doped epitaxial structure with the P-InP cladding to the left, and the N-layers to the right. Holes are injected to the right from the p-region where they flow through the SCH layers into the quantum well. Electrons are injected from the N-InP layer on the right where they flow left into the quantum wells. At higher temperatures, it is possible that the electrons would have enough energy to escape the wells and flow into the SCH region, reducing the injection efficiency.

### 3.2 – Pulsed Lasing Operation

The laser is driven by applying a 0.5  $\mu\text{s}$  long square-wave current pulse with a 4 % duty cycle to the top p and n-contacts. The laser output from one facet is collected by a lensed single mode fiber and detected by a spectrum analyzer or photodetector.

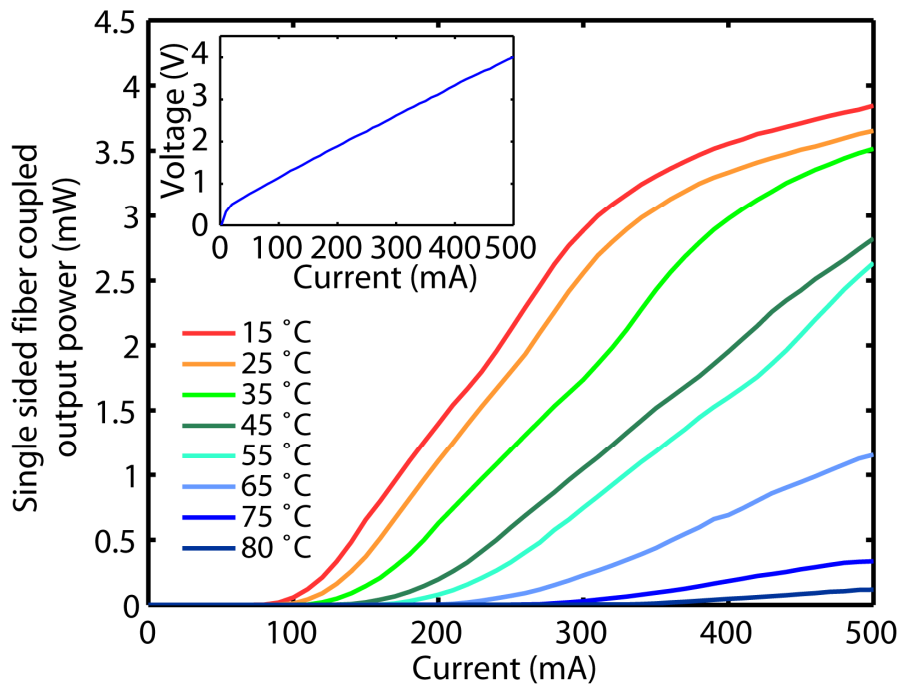


Figure 3.4 - The single sided fiber coupled laser output as a function of drive current for various temperatures. The inset displays the voltage - current characteristics of the laser.

Figure 3.4 shows the measured laser output power as a function of injected current for various temperatures ranging from 15 to 80 °C. As can be seen from the figure, the laser threshold is 120 mA with a maximum power of 3.8 mW at 15 °C. Using the

measured 4 dB coupling loss from waveguide to fiber, and the fact that light is only collected from one facet, we calculate a maximum differential quantum efficiency of 11 %. At higher injection currents, the slope efficiency drops and may be related to device heating induced parasitic current paths [3]. The laser has a maximum lasing temperature of 80 °C.

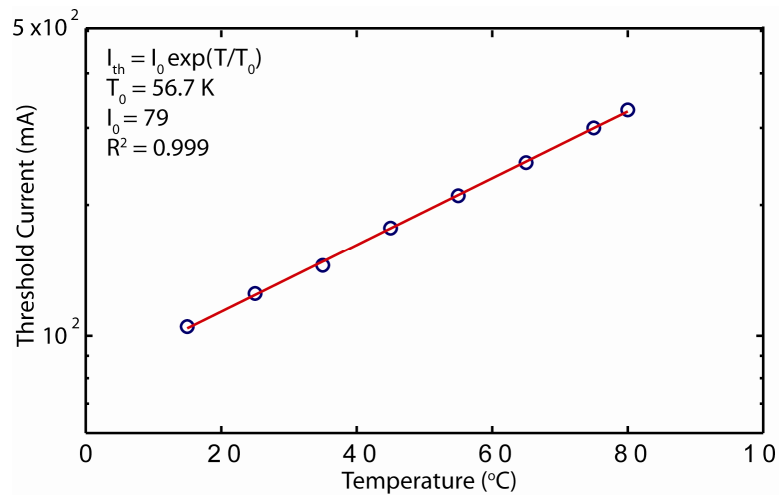


Figure 3.5 – Pulsed threshold versus temperature.

The inset in Figure 3.4 shows the current dependence on voltage for the laser structure. The laser has a threshold voltage of 1.2 V and a series resistance of 7.2 +/- 0.1 ohms. Figure 3.5 shows the threshold current as a function of temperature. The experimental data was fit to extract a characteristic temperature ( $T_0$ ) of 57K, which is in the typical range of 50-70K for III-V lasers in the 1.3-1.55  $\mu\text{m}$  wavelength window [4].

Figure 3.6 shows the measured lasing spectrum of the device driven at 130 mA. The spectrum was measured with an HP 70952A optical spectrum analyzer with a resolution bandwidth of 0.08 nm. The inset in the figure shows the characteristic multi-mode spectrum of a Fabry-Perot laser with a free spectral range of 0.43 nm and multiple lasing modes around 1573 nm. The corresponding group index of the modes is 3.71.

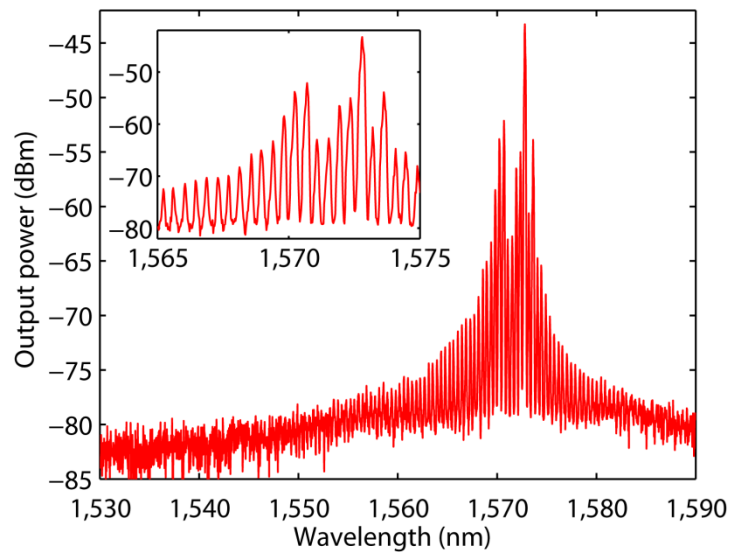


Figure 3.6 - The spectrum of the lasing device. The inset displays a close up of the lasing Fabry-Perot modes.

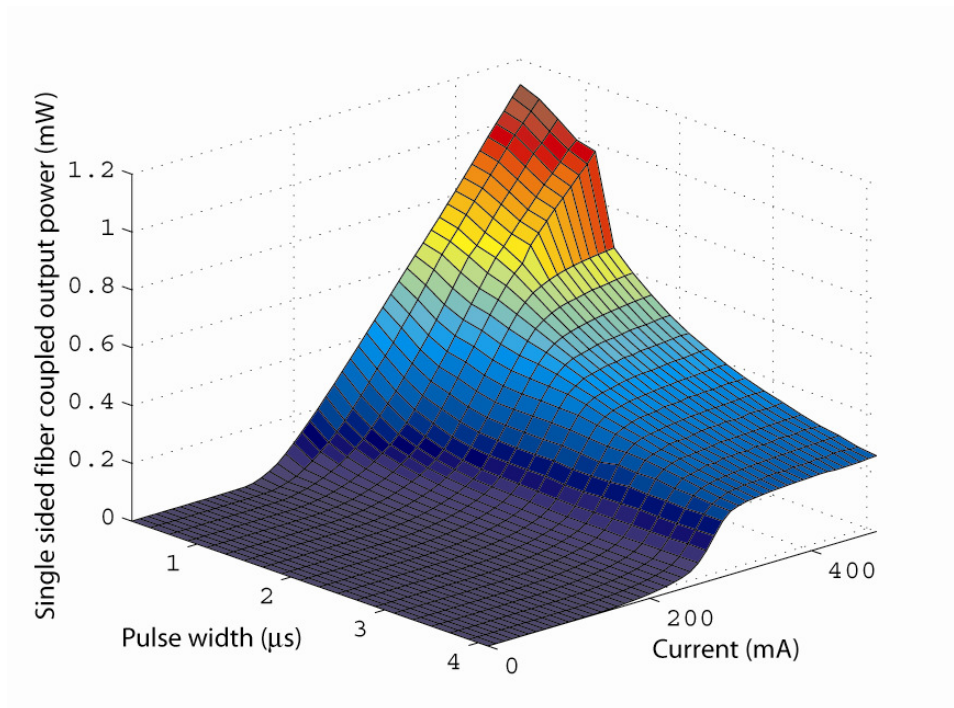


Figure 3.7 - L-I characteristics of a 1  $\mu\text{m}$  waveguide width laser as a function of injected pulse width.

Figure 3.7 - shows the L-I characteristics as the current pulse width is varied from 0.3  $\mu\text{s}$  to 4.1  $\mu\text{s}$ . The duty cycle and stage temperature are held at 4% and 15  $^{\circ}\text{C}$ , respectively. It can be seen that as the pulse duration increases, the lasing threshold increases. For pulses longer than 1.1  $\mu\text{s}$ , the lasing power saturates prematurely slightly above threshold giving evidence of current leakage paths that turn on with device heating [4]. This behavior continues beyond 4.1  $\mu\text{s}$  until lasing is no longer observed. At this point, light is no longer localized in the silicon waveguide region, and the entire mesa shows spontaneous light emission. When the laser is running with pulses short enough that self heating is minimized, and the n mobility is high. In this regime, the P resistance is substantially larger than the N region. The path of

least resistance for the current in this case is first straight down through the mesa towards the silicon waveguide, and then laterally through the N layers (Figure 3.8 a). As the pulse duration increases, device self heating causes the n mobility to decrease, leading to current spread in the P mesa before it reaches the quantum wells (Figure 3.8 b). The injection efficiency,  $\eta_i$ , becomes extremely small since the broadened current profile in the quantum wells is much wider than the optical mode. Consequently, carriers radiatively recombine in regions where they do not contribute to optical gain. This ultimately prohibits continuous wave lasing.

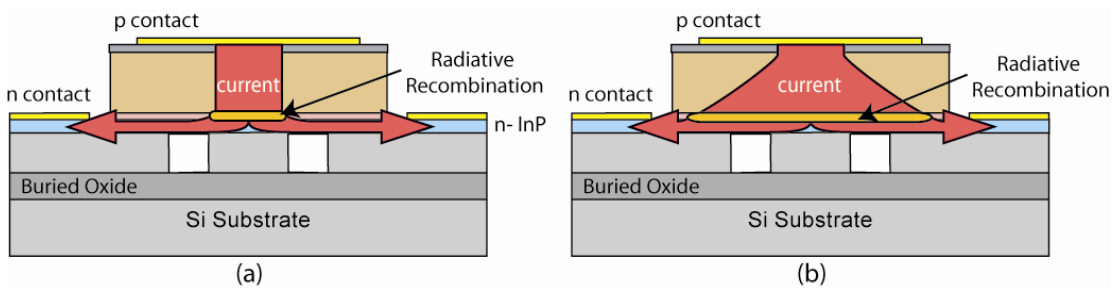


Figure 3.8 – (a) Current path without device heating. (b) Current path with device heating.

### 3.3 – Continuous Wave Device Structure – Lateral Current Confinement

Based on the pulsed results, it is clear that lateral current confinement in the p-upper cladding region is necessary to achieve continuous wave lasing. Figure 3.9 illustrates a current confinement scheme consisting of a current channel through the center of the p-mesa region surrounded by resistive p regions on both sides.



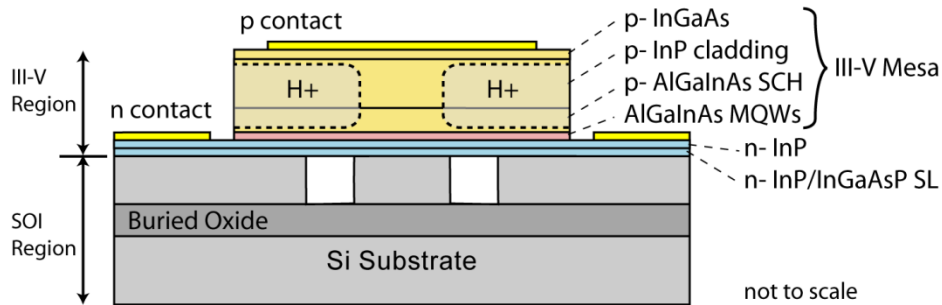


Figure 3.9 – Continuous wave device structure. Proton implanted regions (H<sup>+</sup>) provide lateral current confinement in the p type mesa region.

H<sup>+</sup> ion implantation, or ion irradiation, provides a method for electrical isolation in p-type InP [5]. The implanted ions create deep level centers that trap free carriers that are not thermally excited at device operating temperatures, resulting in areas of high resistance. This method is commonly used for the isolation of elements in photonic integrated circuits and the reduction of free carrier loss caused by dopants in passive waveguides. The degree of isolation is related to the Ion implant density. A critical density of  $2.5 \times 10^{18}$  ions/cm<sup>3</sup> is used as a design rule to achieve proper isolation, while densities in the conductive regions are kept below  $1 \times 10^{17}$  ions/cm<sup>3</sup>.

The H<sup>+</sup> implant profile was designed by calculating the implant depth, spread, and lateral straggle for various implant energies for our layer structure using SRIM, an ion stopping range program [6]. An implant angle of 7 degrees from the normal axis to the sample surface is used to minimize channeling effects. A 300 nm SiN layer is used on the top surface during implant and included in our layer structure calculations in order to protect the surface quality of the semiconductor.

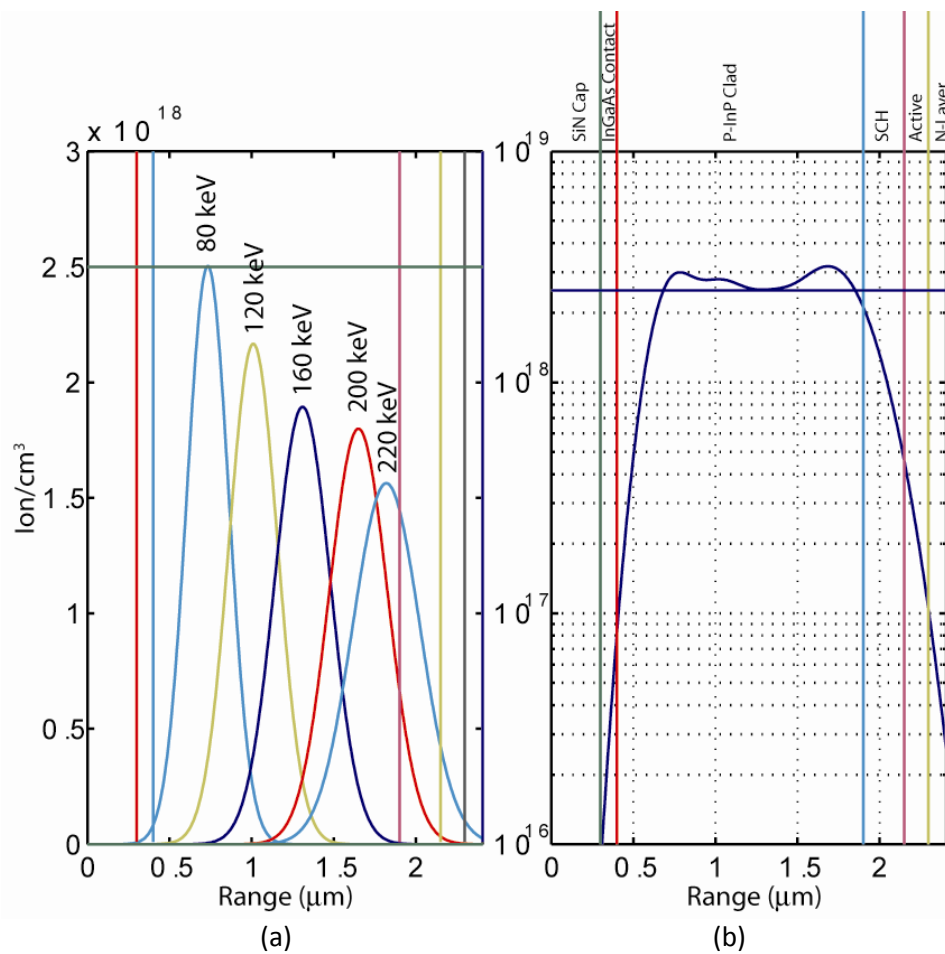


Figure 3.10 – a) Implant profiles for various implant energies and dosages. b) Total implant profile.

After a table of depths and straggles are computed, dosages are chosen for various implant energies (Figure 3.10 a) and the individual profiles are added together to form a total implant profile (Figure 3.10 b). The goal of our first proton implant design was to insulate ( $> 2.5 \times 10^{18}$  ions/cm<sup>3</sup>) the p region as deep as possible to minimize current spreading. In order to maintain lateral current flow through the n region, the n region was kept at a doping level of  $< 1 \times 10^{17}$  ions/cm<sup>3</sup>, as shown in

Figure 3.9 b. The active region implant density was also kept as low as possible in order to prevent the introduction of non-radiative recombination centers [7].

In addition to the implant profile depth, the current channel width plays a role in the device injection efficiency. 8  $\mu\text{m}$ , 6  $\mu\text{m}$ , and 4  $\mu\text{m}$ , channel widths (as drawn on the mask) were chosen since the contact aligner has an alignment error of  $\pm 1.5 \mu\text{m}$  and the optical mode is  $\sim 2 \mu\text{m}$  wide. The lateral straggle is calculated to be 292 nm.

The silicon waveguide die were off the same wafer as those presented in the pulsed section with waveguide widths of 1  $\mu\text{m}$  to 3.5  $\mu\text{m}$  in 0.5  $\mu\text{m}$  steps.

### *3.4 – Continuous Wave Lasing*

The 2.5  $\mu\text{m}$  width waveguides with a 4  $\mu\text{m}$  current channel width had the best overall performance and will be presented here in detail. The confinement factors for the silicon and quantum well regions for this dimension were 75% and 3% respectively.

A  $15 \text{ cm}^{-1}$  modal loss was measured using the Hakki-Paoli method in the long wavelength regime [8]. Since the gain is extremely low in the long wavelength regime, the Fabry-Perot response of the cavity is primarily determined by the modal loss and the mirror loss. By measuring the extinction ratio of the peaks and valleys of the long wavelength Fabry-Perot response, the loss is estimated as follows:

$$(Eq. 3-1) \quad \langle \alpha \rangle = \frac{1}{L} \ln \left( \frac{1 + \sqrt{\frac{Power_{valley}}{Power_{peak}}}}{\frac{1}{R} \sqrt{\frac{Power_{valley}}{Power_{peak}}}} \right),$$

where L is the cavity length, and R is the mirror reflectivity. We assume a reflectivity of 30%, based on Fresnel reflection. This loss is larger than what you would expect if you estimate the loss by taking the sum of the product of the confinement factors and their typical waveguide losses as follows:

$$(Eq. 3-2) \quad \langle \alpha \rangle = \Gamma_{Si} \alpha_{Si} + \Gamma_{III-V} \alpha_{III-V}$$

$$= 0.74 * 0.075 \text{ cm}^{-1} + 0.26 * 10 \text{ cm}^{-1} = 2.665 \text{ cm}^{-1}$$

We are not certain where the additional loss comes from, but a few possibilities may be from scattering losses at the bonded interface, or scattering off contamination in the air regions of the rib etch during processing and although the loss is higher than expected, it is still on the same order as typical III-V lasers.

Figure 3.11 shows the measured continuous wave laser fiber coupled output power from one facet as a function of injected current for various operating temperatures ranging from 15 to 40 °C. As can be seen from Figure 3.11, the laser threshold is 65 mA with a maximum single sided fiber coupled output power of 1.8 mW at 15 °C. The laser has a 40 °C maximum lasing temperature with a characteristic temperature

of 39 K. The differential efficiency taken from the data in Fig. 3.11 was 2.1%.

Differential efficiency is expressed as follows [9]:

$$(Eq. 3-3) \quad \eta_d = \eta_i \frac{\langle \alpha_m \rangle}{\langle \alpha_i \rangle + \langle \alpha_m \rangle}$$

where  $\eta_i$  is the injection efficiency and  $\langle \alpha_m \rangle$  is the mirror loss. Plugging in the measured value for  $\langle \alpha_i \rangle$  of  $15 \text{ cm}^{-1}$ , the calculated value for  $\langle \alpha_m \rangle$  of  $13.4 \text{ cm}^{-1}$ , and the 0.51% value for  $\eta_i$ , extrapolated from the laser threshold as discussed in the end of this section, the differential efficiency comes out to 24%. The 10.5 dB discrepancy between the measured value and the calculated value can be reconciled by taking into account light coming out of both facets (-3 dB) and the coupling loss between the waveguide and the fiber. The coupling loss is measured on a few devices at 6 dB +/- 1.5 dB. We believe a 7.5 dB coupling loss is reasonable and show a secondary y-axis is shown denoting the estimated total laser output power. This leads to a 24% differential efficiency and 20 mW total laser output power at 15 °C. The laser has a threshold voltage of 2 V and a series resistance of 7.5 ohms.

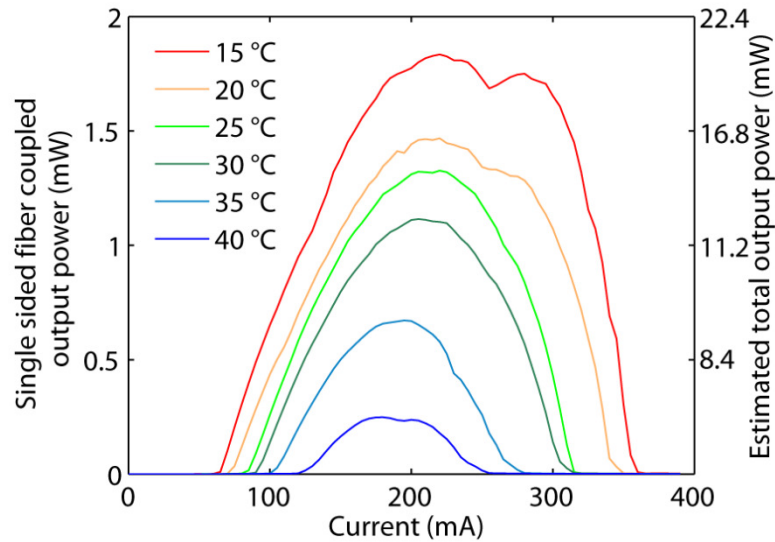


Figure 3.11 - The single sided fiber coupled laser output as a function of drive current for various operating temperatures.

Figure 3.12 shows the measured multi-mode lasing spectrum of the silicon evanescent laser driven slightly above threshold at 70 mA, and well above threshold at 100 mA. The spectrum was measured with an HP 70952A optical spectrum analyzer with a resolution bandwidth of 0.08 nm. The lasing wavelength is around 1577 nm at 75 mA and is shifted to longer wavelengths at higher injection currents due to device heating. It is important to note that the spectral shift is not the expected 10 nm between 75 mA and 200 mA, based on the typical 0.5 nm/°C seen in typical Fabry-Perot III-V lasers. This can be due to the uncharacteristic modulation seen in the spectrum with a free spectral range of about 23 nm. The modulation is also visible below threshold, and indicates a wavelength dependent loss or gain, influencing the lasing peak. Although this has not been fully analyzed, we believe that this may be due to wavelength dependent coupling to other modes in the

structure such as the high index substrate or slab modes in the mesa as observed by Bergmann *et al.* in AlGaIn/InGaIn laser diodes [10]. Coupling between the waveguide layer and other layer is enhanced when the mode of the other layer is in resonance, while the coupling is repressed when the mode of the other layer is off resonance, resulting in a periodic wavelength dependent loss in the waveguide.

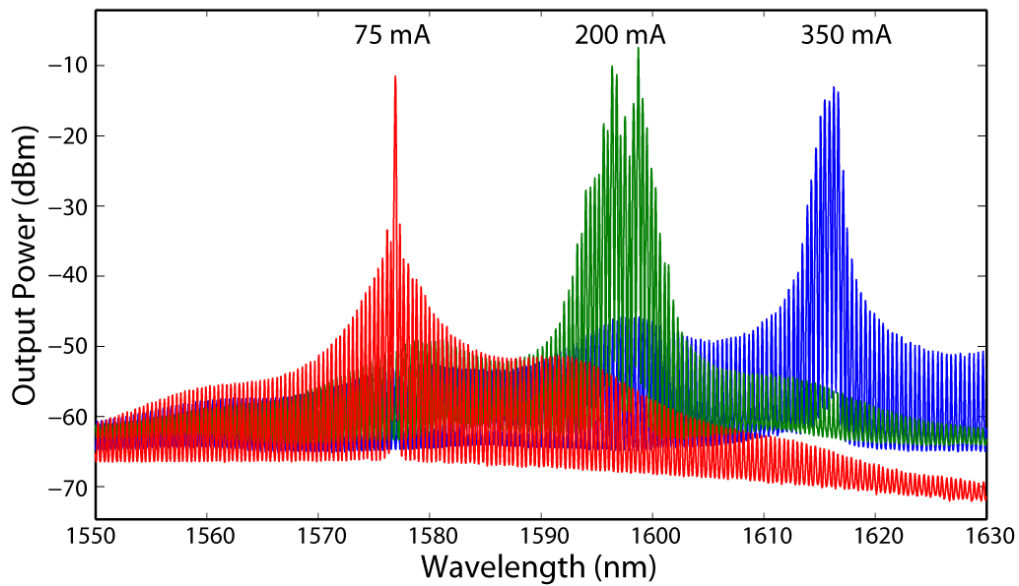


Figure 3.12 - The hybrid laser spectrum taken slightly above threshold (75 mA) and well above threshold (200 and 350 mA). The y-axis is on a logarithmic scale.

Figure 3.13 shows a scatter plot of the thresholds for varying waveguide width and proton implant channel width. We believe that the facet polishing creates enough scatter in the data that no relationship between waveguide width and threshold is seen. The relationship between current channel widths is clearly seen with current channels of 4  $\mu\text{m}$  wide having the lowest threshold. The number of working devices for each waveguide width is marked above the data out of a total number of 6. It can

be seen that the narrower waveguide widths have lower yield and can be attributed to device delamination and facet damage during waveguide polishing as observed when the laser facet is imaged with a camera. The narrower waveguides have less bonded area across the mesa region leading to reduced mechanical strength. The yield of this process is reasonable with 26 of the 36 lasers on this chip lasing with similar performance when tested individually. Incorporating monolithic laser feedback schemes, such as ring resonator cavities or gratings in the silicon region, greatly improves yield.

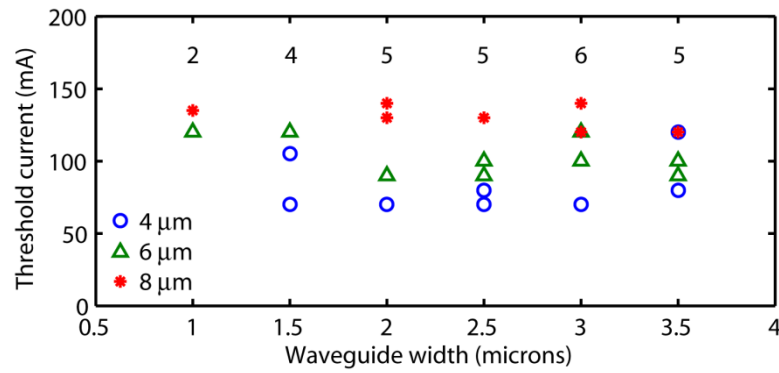


Figure 3.13 – Scatter plot of laser thresholds with varying waveguide width and current channel width.

The threshold of a laser can be expressed as follows [11]:

$$(Eq. 3-4) \quad I_{th} = \frac{N_{tr}^2 B q V_{active}}{\eta_i} e^{\frac{2(\langle \alpha_i \rangle + \langle \alpha_m \rangle)}{\Gamma_{qw} g_0}}$$

where  $N_{tr}$ ,  $B$ , and  $V_{active}$ , and, are the transparent current density, the bimolecular recombination coefficient, and the volume of the active region respectively. The gain



coefficient,  $g_0$ , was measured to be  $972 \text{ cm}^{-1}$  by fabricating amplifiers with this structure and fitting the gain current density relation [12]:

$$(Eq. 3-5) \quad \langle g \rangle = \Gamma_{qw} g_0 \ln \frac{J \eta_i}{J_{tr}}$$

The threshold current is calculated by taking the measured values of  $\langle \alpha_i \rangle$ , and  $g_0$ , and the calculated value for  $\Gamma_{qw}$  of 3.5%. The values of  $B$ , and  $N_{tr}$  were assumed to be  $10^{-10} \text{ cm}^3/\text{s}$  [13], and  $1.4 \times 10^{18} \text{ cm}^{-3}$ , respectively, and  $\eta_i$  was used as a fitting parameter such that injection efficiency could roughly be determined.

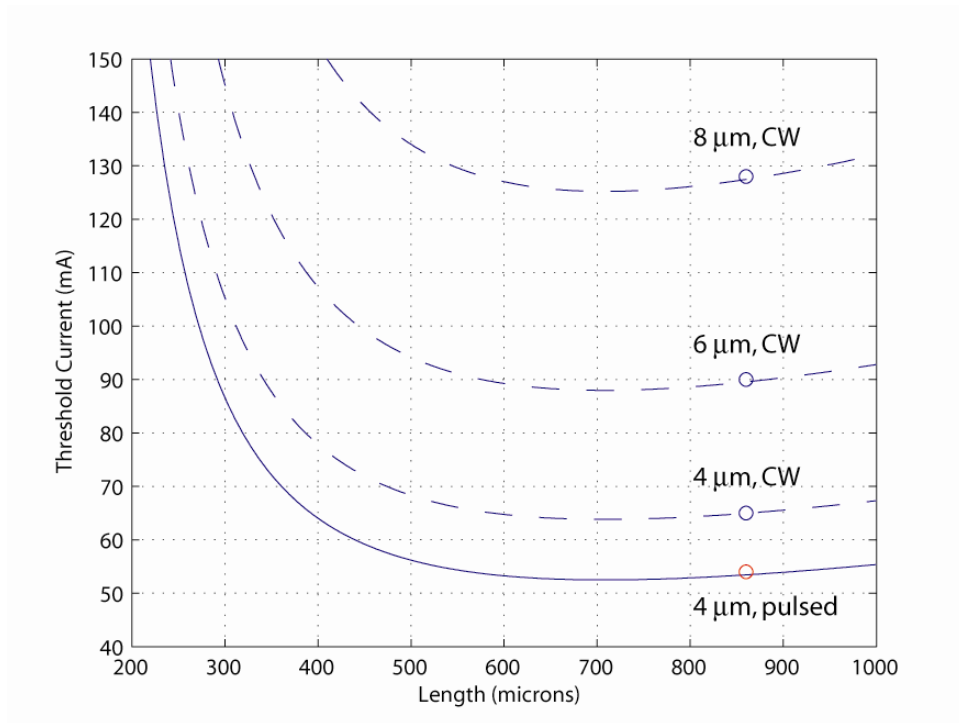


Figure 3.14 – Fitted threshold curves for  $W = 2.5 \mu\text{m}$  waveguides with various current channel widths.

Current channel width	$\eta_i$	waveguide width/ channel width
4 microns (pulsed)	0.62	0.62
4 microns (CW)	0.51	0.62
6 microns (CW)	0.37	0.41
8 microns (CW)	0.26	0.31

Table 3.2 – Current channel width and the fitted injection efficiencies for  $w = 2.5 \mu\text{m}$  waveguides.

Figure 3.14 shows the fitted threshold current vs. length curves for a  $2.5 \mu\text{m}$  wide waveguide width for a  $4 \mu\text{m}$  wide current channel under pulsed and CW lasing, and  $6 \mu\text{m}$  and  $8 \mu\text{m}$  current channels under CW lasing. Table 3.2 shows the injection efficiency used in these fits. The ratio of the waveguide width over the channel width is also denoted on this chart as it is a rough approximation for mode to current profile overlap and therefore serves as the upper limit to the injection efficiency. It can be seen that the injection efficiency is best for the  $4 \mu\text{m}$  wide current channels and the current channel can be narrowed further to improve the injection efficiency to the 90% range. The proton implant profile is designed to be effective through at least the upper half of the SCH in the p-type mesa, but has not been experimentally optimized. Additional improvements in injection efficiency of the device can be made by optimizing the depth of the proton implant profile in order to reduce the current spreading in the SCH while maintaining high conductivity on the n-type layers.

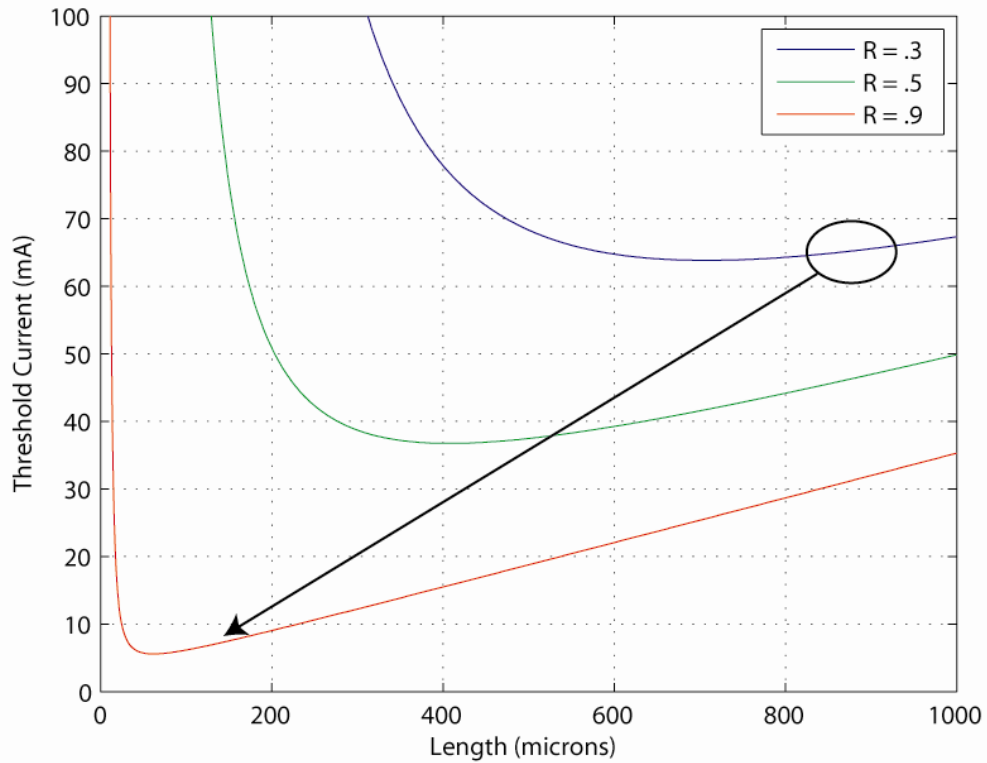


Figure 3.15 – Theoretical threshold improvements based on cavity length reduction and an increase in mirror reflectivity.

Figure 5.15 shows the predicted CW threshold currents for the 4  $\mu\text{m}$  current channel width as a function of length for mirror reflectivities of 0.3, 0.5, and 0.9. Since the current device relies only on the 30 % silicon-to-air facet reflection, a significant reduction in threshold current would be achieved through the deposition of high reflection coatings onto the waveguide facets or integrating gratings on the silicon, allowing for much shorter cavities.

To demonstrate the potential scalability of this hybrid laser approach, Figure 3.16 shows the imaged output facet using an infrared camera of seven c.w. silicon evanescent lasers operating simultaneously from a single bonded silicon chip. The lasers were fabricated on an 8 mm wide silicon chip containing 36 lasers of varying waveguide widths from 1-3.5 $\mu\text{m}$ . The number of evanescent laser devices running simultaneously is only limited by the electrical contact configuration of the current experimental set up (i.e. the number of electrical probes that could be placed simultaneously onto the test chip rather than the number of functional devices). Waveguides with larger widths showed multimode behavior in the lateral direction. Waveguides 2.5  $\mu\text{m}$  wide and narrower lased at the fundamental mode.

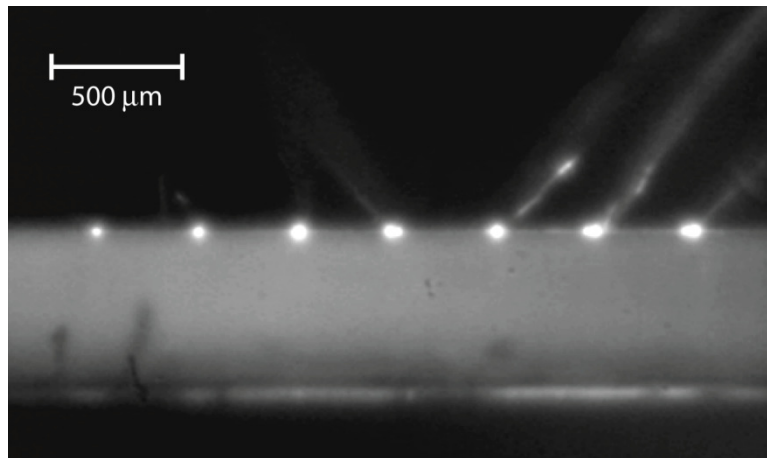


Figure 3.16 - An infrared image taken from one of the polished facets showing seven c.w. silicon evanescent lasers operating simultaneously.

### 3.5 – Thermal Analysis

The modal gain,  $\langle g \rangle$ , is dependent on the temperature of the active region. As the active region temperature increases,  $\langle g \rangle$  decreases due to increased carrier leakage out or not reaching the active region, and/or increased non-radiative recombination [14]. More current is needed to achieve enough modal gain to maintain lasing. Beyond a certain active region temperature,  $T_{off}$ , no current density will allow  $\langle g \rangle$  to satisfy the characteristic laser equation. We can utilize this concept to analyze the lasers CW L-I curve to extract the device thermal impedance as described by Margalit [15].

The temperature in the active region at laser turnoff can be written as the sum of the device stage temperature and the change in temperature due to electrical power dissipation:

$$(Eq. 3-6) \quad T_{off} = T_{Stage} + \Delta T$$

where the change in temperature due to electrical power dissipation at turnoff is equal to the power dissipation multiplied by the thermal impedance of the device:

$$(Eq. 3-7) \quad \Delta T = P_{dissipated} Z_T$$

Therefore the power dissipated is as follows:

$$(Eq. 3-8) \quad P_{dissipated} = -\frac{1}{Z_T} [T_{Stage} - T_{off}]$$

Since  $T_{off}$  and  $Z_T$  are constants, this relationship is linearly decreasing with a slope inversely proportional to  $-Z_T$  as a function of stage temperature and can be used to experimentally measure the device thermal impedance by multiplying the current injection level and device voltage at turnoff for various temperatures.

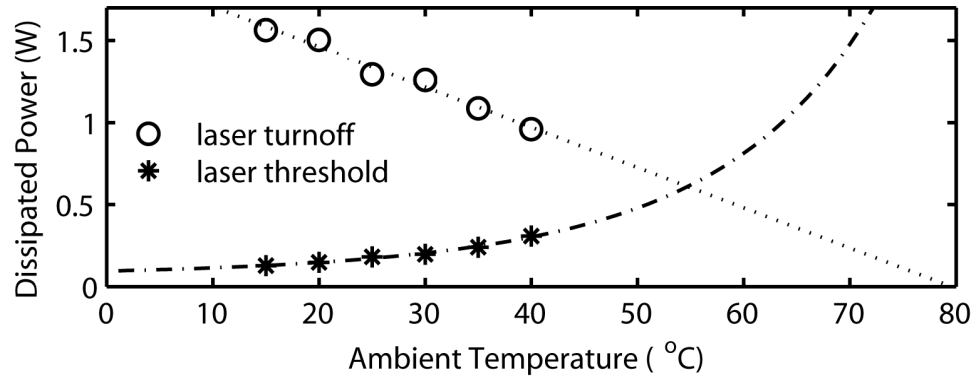


Figure 3.17 - Dissipated electrical power at the threshold and laser turnoff.

Figure 3.17 shows the dissipated electrical power at laser threshold and laser turn off. The thermal resistance of 38 °C/W is extracted from the slope of this data. In addition, the x-intercept of 80 °C of the line is the maximum temperature for lasing,  $T_{off}$ , which is ideally the maximum temperature of pulsed operation.

This plot also gives us some understanding on how to improve the device performance. It can be seen that CW lasing only occurs where the power dissipated at laser threshold is below the power dissipated at laser turn-off. The maximum CW lasing temperature can be increased by raising the turnoff line, or by lowering threshold curve. The turnoff line can be raised by lowering the thermal impedance

or by pushing out the  $T_{\text{off}}$  point. The power dissipation at threshold follows the following behavior:

$$\text{(Eq. 3-9)} \quad P_{\text{dissipated at threshold}} = I_{\text{th}} V_{\text{th}}$$

Assuming  $I_{\text{th}}$  exponentially scales with temperature and the turn on voltage of the diode is linear with threshold current,  $I_{\text{th}} = R_s (V_{\text{th}} - V_{\text{on}})$  we come to the following expression:

$$\text{(Eq. 3-10)} \quad P_{\text{dissipated at threshold}} \approx I_0^2 R_s e^{\frac{2T_{\text{stage}}}{T_0}} + V_{\text{on}} I_0 e^{\frac{T_{\text{stage}}}{T_0}}$$

1-D Simulations show that the buried oxide thickness reduction from 2  $\mu\text{m}$  to 1  $\mu\text{m}$  will reduce the thermal resistance from 38  $^{\circ}\text{C}/\text{W}$  to 28  $^{\circ}\text{C}/\text{W}$  leading to better heat extraction from the active region. In addition to reduction of electrical and thermal resistance, lasing threshold reduction would also improve the temperature performance.

### ***3.6 – Second Generation Fabry-Perot Lasers***

After the initial demonstration of electrically pumped silicon evanescent lasers, a second generation of devices was designed to improve the device performance. The first change was a reduction in buried oxide thickness from 2  $\mu\text{m}$  to 1  $\mu\text{m}$  in order to reduce the thermal impedance. The second change was to reduce the mesa width

from 75  $\mu\text{m}$  to 14  $\mu\text{m}$  such that the n contacts could be brought closer to the optical mode to lower the n layer series resistance.

The device dimensions were kept as close to the first generation as possible in order to maintain the active region confinement factor and roundtrip loss, to enable direct comparisons between the first generation and second generation designs. The waveguide height, width, rib etch depth, and cavity length were 0.7  $\mu\text{m}$ , 2  $\mu\text{m}$ , 0.5  $\mu\text{m}$ , and 850  $\mu\text{m}$ , respectively. The current channel was kept fixed at 4  $\mu\text{m}$  since the first generation devices showed a clear improvement for current channels of 4  $\mu\text{m}$  over the 6  $\mu\text{m}$  and 8  $\mu\text{m}$  current channel devices. Although further optimization of this channel width can and should be made, we chose to stick with this value due to the tolerances associated with contact alignment, and it was unclear at the time whether or not the projection lithography stepper would focus properly on our 8 mm x 8 mm samples. A move to projection lithography for future generations would allow alignment tolerances well within the 1  $\mu\text{m}$  range, allowing for much narrower current channels.

Since the mesa in this design is too narrow for probing, P probe pads were placed on 450 nm thick silicon nitride ( $\text{SiN}_x$ ) electrical isolation pads. A top view diagram of the device layout is shown in Figure 3.18. The 8 mm long devices were laid out across the die such that a few laser bars could be diced and polished out at the desired lengths.



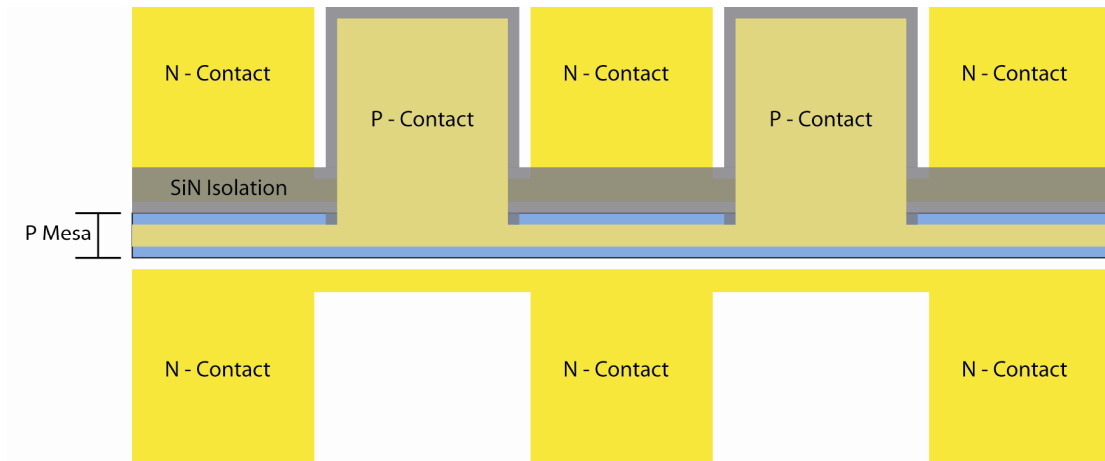


Figure 3.18 – Top view of the Fabry Perot Laser layout illustrating the p pad and n pad configuration.

The CW LI curve for this device is collected on one side with an integrating sphere as shown in Figure 3-19. In order to account for light exiting both sides of the cavity, the data is multiplied by two. It can be seen that the maximum laser output, threshold, and differential efficiency at 15 °C are 32.8 mW, 70 mA, and 26%, respectively.

It is difficult to compare the difference in absolute power improvement between the two generations since the first generation was measured with fiber coupling, leading to uncertainty in the absolute coupling efficiency, but it can be seen that the current level where the laser has maximum output power increased from 205 mA to 350 mA, indicating the push back of thermal roll-off to higher current levels due to

reduced power dissipation. The device series resistance was 4.6 ohms over the first generation resistance, supporting the theory of minimized parasitic device power dissipation in the n-region. The maximum operating temperature was slightly improved to 45 °C.

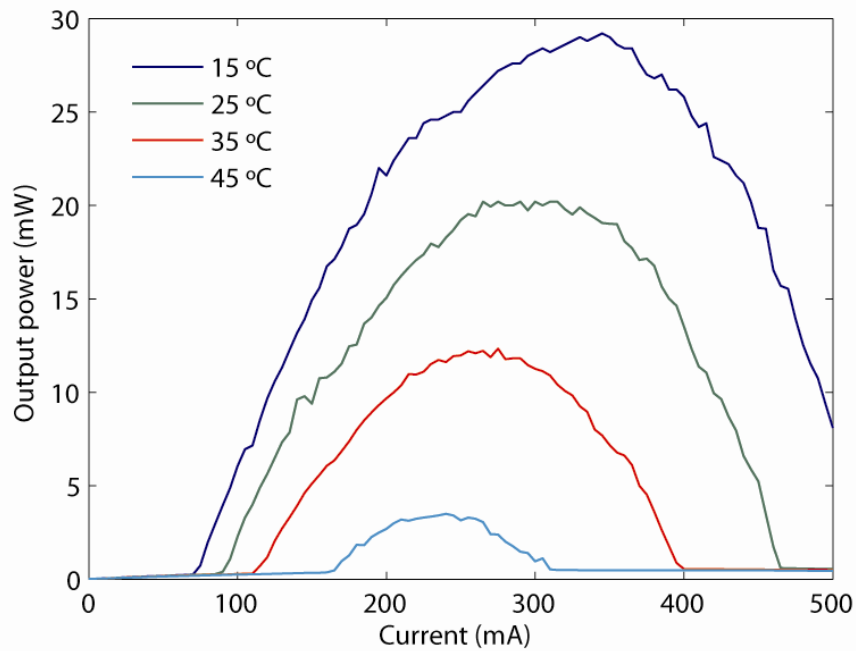


Figure 3-19: L-I curve for second generation 850 μm long hybrid silicon evanescent Fabry Perot laser

By applying the same thermal analysis of electrical power dissipation at laser threshold and laser turn off to this second generation of devices, we find that even though there is an improvement in device output power, as seen in the CW LI curves, the overall thermal impedance between the two generations was almost identical at  $\sim 38$  °C/W. This result came as a surprise, as we expected a thermal impedance reduction to 28 °C/W, due to the reduction in buried oxide thickness.

### 3.7 – Thermal Modeling of Fabry Perot Lasers

A 2-D model of the device structure was conducted to investigate the thermal characteristics of the two structures [16]. The model is generated by mapping out the thermal conductivity,  $k$ , in each layer, and by taking into account the heat generated in each section under a fixed current injection through the structure. A thermal profile is then generated allowing us to estimate the temperature of the active region for a given electrical power dissipation and is used to calculate the thermal impedance. The thermal conductivity in each of the various regions is  $k_{\text{InP}} = 130 \text{ W/m/K}$ ,  $k_{\text{Si}} = 130 \text{ W/m/K}$ ,  $k_{\text{SiO}_2} = 1.3 \text{ W/m/K}$ , and  $k_{\text{QWs}} = 5 \text{ W/m/K}$  (active QWs). Heat is generated in the structure from resistive heating in the  $4 \mu\text{m}$  wide p-type current channel above the active region, the n regions between the n contacts and the active region, the p and n contacts, and the active region. There is also additional heat generation associated with the diode drop in the active region.

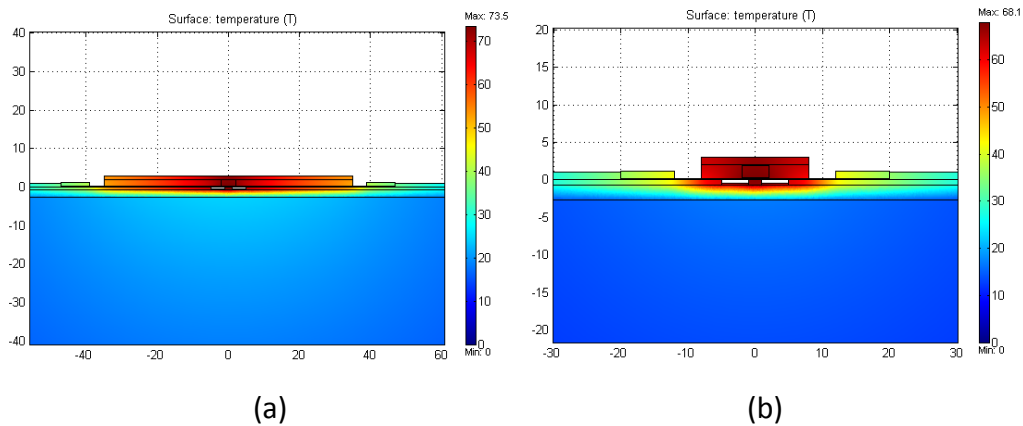


Figure 3-20: The thermal profile for the (a) first generation, and (b) second generation waveguide cross sections under 500 mA of injection current.

Figure 3-20 shows the temperature profile for the first generation (a) and second generation (b) laser structure for a current injection level of 500 mA. As you can see, due to the low thermal conductivity of the buried oxide, most of the heat is kept in the III-V region and needs to flow laterally in order to leave the device. Recall that there are two differences between the 1<sup>st</sup> and 2<sup>nd</sup> generation devices. First, the buried oxide was thinned from 2  $\mu\text{m}$  to 1  $\mu\text{m}$ . Second the III-V mesa was narrowed from 70  $\mu\text{m}$  to 14  $\mu\text{m}$ .

		Mesa Width ( $\mu\text{m}$ )	
		14	70
Buried Oxide thickness ( $\mu\text{m}$ )	1	36.2 / 52.4	24.5 / 55.7
	2	46.7 / 68.1	33.4 / 73.5
		$Z_t$ ( $^{\circ}\text{C}/\text{W}$ ) / $\Delta T$ ( $^{\circ}\text{C}$ )	

Table 3.3 – The thermal impedance and temperature change for buried oxide thickness of 1  $\mu\text{m}$  and 2  $\mu\text{m}$  and mesa widths of 14  $\mu\text{m}$  and 70  $\mu\text{m}$  at a current injection level of 500 mA

Table 3.3 shows a matrix of the thermal impedance and the change in active region temperature for these 4 structures under 500 mA of current injection. As you can see, when the III-V mesa width is fixed, and the buried oxide thickness is reduced, the thermal impedance improves, with a reduction from 33.4  $^{\circ}\text{C}/\text{W}$  to 24.5  $^{\circ}\text{C}/\text{W}$  for the 70  $\mu\text{m}$  wide mesa, by increasing heat to flow down through the substrate.

Unfortunately, as the mesa width narrows lateral heat extraction degrades. We simulate the thermal impedance of the generation 1 and generation 2 devices to be 33.4 °C/W and 36.2 °C/W, respectively; values that are very similar to the experimentally measured value of 38 °C/W. Although the thermal impedances of the two generations are very similar, we see an improvement in device performance in the second generation device due to a reduction in power dissipation in the narrowed n regions of the device. This results lower active region temperatures for a given current level in the generation 2 devices (table 3.3), resulting in higher gain and improved output performance.

### *3.8 – Summary*

In this chapter, we presented a current injection scheme for realizing electrically pumped silicon evanescent lasers. Pulsed lasing was demonstrated by modifying the epitaxial-layer structure to include doped layers for carrier injection. In order to achieve CW lasing, a proton implant scheme was used to provide lateral current confinement, leading to an improved electrical carrier profile to optical mode overlap. 1<sup>st</sup> generation electrically pumped CW lasers were shown to have a 65 mA minimum current threshold at 15 °C with a maximum operating temperature of 40 °C. The total output power is ~ 20 mW, taking into account 7.5 dB fiber coupling loss and light exiting both facets. The device thermal impedance is measured to be 38 °C/W. Second generation devices were demonstrated with a reduced buried oxide

and reduced mesa width, resulting in devices that had less heat generation while maintaining similar thermal impedance. With these improvements, the lasers show a 40% improvement in output power, with a maximum power of 28 mW and a 26 % differential efficiency. In addition, a maximum operating temperature of 45 °C was achieved; a 5 degree improvement over the first generation devices. The work in this chapter demonstrates the ability of the silicon evanescent platform to produce electrically pumped lasers on silicon with reasonable device thresholds and device output powers comparable to typical III-V lasers with the potential for further optimization in future devices.

### *References*

- [1] A. W. Fang, H. Park, O. Cohen, R. Jones, M. J. Paniccia, and J. E. Bowers, "Electrically pumped hybrid AlGaInAs-silicon evanescent laser," *Optics Express*, 14, 9203-9210, (2006)
- [2] A. Karim, P. Abraham, D. Lofgreen, Y. J. Chiu, J. Piprek, and J. E. Bowers, "Wafer-bonded 1.55- $\mu$ m vertical-cavity lasers with continuous-wave operation up to 105 C," *Appl. Phys. Lett.*, vol. 78, no. 18, pp. 2632–2633, Apr. 2001.
- [3] L. A. Coldren and S. W. Corzine, *Diode Lasers and Photonic Integrated Circuits*. New York: John Wiley & Sons, Inc., 1995 pp. 60
- [4] L. A. Coldren and S. W. Corzine, *Diode Lasers and Photonic Integrated Circuits*. New York: John Wiley & Sons, Inc., 1995 pp. 58
- [5] H. Boudinov, H. H. Tan, and C. Jagadish, "Electrical isolation of n-type and p-type InP layers by proton bombardment," *J. Appl. Phys.* 89 10, 5343-5347
- [6] SRIM The Stopping and Range of Ions in Matter, <http://www.srim.org>

- [7] L. A. Coldren and S. W. Corzine, *Diode Lasers and Photonic Integrated Circuits*. New York: John Wiley & Sons, Inc., 1995 pp. 144
- [8] Hakki, B. W., & Paoli, T. L., "CW degradation at 300K of GaAs double-heterostructure junction lasers –II: Electronic gain," *J. Appl. Phys.* 44 , 4113-4119 (1973)
- [9] L. A. Coldren and S. W. Corzine, *Diode Lasers and Photonic Integrated Circuits*. New York: John Wiley & Sons, Inc., 1995 pp. (Differential efficiency page)
- [10] M. J. Bergmann, and H. C. Casey, Jr., "Optical-field calculations for lossy multiple-layer  $\text{Al}_x\text{Ga}_{1-x}\text{N}/\text{In}_x\text{Ga}_{1-x}\text{N}$  laser diodes," *J. Appl. Phys.* 84 , 1196-1203 (1998)
- [11] L. A. Coldren and S. W. Corzine, *Diode Lasers and Photonic Integrated Circuits*. New York: John Wiley & Sons, Inc., 1995 pp. 45
- [12] H. Park, A. W. Fang, O. Cohen, R. Jones, M. J. Paniccia, J. E. Bowers, "A Hybrid AlGaInAs-Silicon Evanescent Amplifier," *IEEE Photonics Technology Letters*, Vol. 19, No. 4, (2007)
- [13] L. A. Coldren and S. W. Corzine, *Diode Lasers and Photonic Integrated Circuits*. New York: John Wiley & Sons, Inc., 1995 pp. 45
- [14] L. A. Coldren and S. W. Corzine, *Diode Lasers and Photonic Integrated Circuits*. New York: John Wiley & Sons, Inc., 1995 pp. 58
- [15] N. Margalit, "High temperature long-wavelength vertical-cavity lasers" June 1998
- [16] M. N. Sysak, H. Park, A. W. Fang, J. E. Bowers, R. Jones, O. Cohen, O. Raday, and M. Paniccia, "Experimental and theoretical thermal analysis of a Hybrid Silicon Evanescent Laser," *Optics Express*, Vol., 15 No. 23 Pg: 15041-15046, (2007)

## Chapter 4 - Electrically Pumped Silicon Evanescent Lasers – Racetrack Ring Lasers

Although the realization of Fabry-Perot lasers with the silicon evanescent waveguide structure demonstrates electrically pumped lasers on, the end goal is to integrate these with other devices. The Fabry-Perot laser's dependence on facet polishing make it a discrete device by nature. By using a racetrack ring resonator topography, we are able to make an on chip laser with performance characteristics that are independent of sample preparation such as dicing and polishing. The device topography is shown in Figure 4-5. Feedback is achieved by wrapping the waveguide on-to itself forming a racetrack ring resonator. Another bus waveguide is brought into close proximity of the straight section of the racetrack resonator to form a directional coupler. In this chapter we present the design of racetrack lasers, and the continuous wave and mode locked lasing performance of fabricated devices.

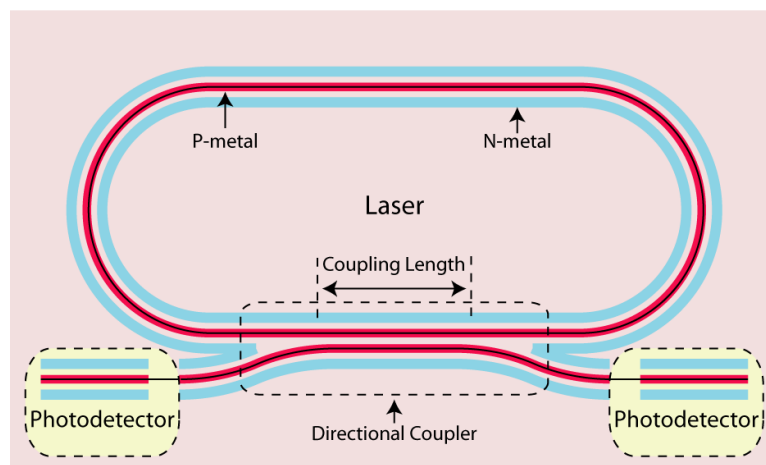


Figure 4-5. The layout of the racetrack resonator and photodetectors.



## 4.1 – Racetrack Laser Design

Ring lasers and linear cavity lasers have subtle differences that affect the lasers characteristics, such as lasing threshold, differential efficiency, and output stability [1][2][3]. First of all, in linear cavity lasers, the forward propagating light is coupled to the backward propagating light through mirror reflections. In ring lasers, the clockwise propagating light is generally decoupled from the counter clockwise propagating light. This results in two major differences. First, the round trip cavity length of a ring laser is the circumference of the cavity, as opposed to twice the cavity length. This will affect the formulation of “mirror loss”, which will in turn alter the formulation for threshold current and differential efficiency. The second result is that there is a degeneracy between these two modes and unless the degeneracy is broken by creating differential loss/gain between the modes or by coupling them into a single mode, they will compete with each other resulting in random mode hopping from one to the other [1][2][3].

The amplitude of the round trip condition at threshold for racetrack lasers is written as follows:

$$(Eq. - 4.1) \quad 1 = \sqrt{T} e^{\frac{-(\alpha_i) + \langle g_{th} \rangle}{2} L_{cavity}} e^{\frac{-\alpha_{bend}}{2} L_{bend}}$$

where T is the fraction of the power sent in to the directional coupler coming out of the through port contributing to feedback,  $\langle \alpha_i \rangle$  is the modal loss,  $\langle g_{th} \rangle$  is the

threshold modal gain, and  $L_{cavity}$  is the circumference of the racetrack. Bend loss from the two circular portions of the racetrack is taken into account by adding the second exponential term where  $\alpha_{bend}$  is the additional loss from bends and  $L_{bend}$  is the length of the circular portions of the ring. This formulation can be modified by doing some simple algebra to give the following form:

$$\begin{aligned}
 \text{(Eq. - 4.2)} \quad \langle g_{th} \rangle &= \langle \alpha_i \rangle + \langle \alpha_{bend} \rangle + \langle \alpha_{coupler} \rangle \\
 &= \langle \alpha_i \rangle + \alpha_{bend} \frac{L_{bend}}{L_{cavity}} + \frac{2}{L_{cavity}} \ln \frac{1}{\sqrt{T}}
 \end{aligned}$$

where the additional loss due to bends is defined as follows:

$$\text{(Eq. - 4.3)} \quad \langle \alpha_{bend} \rangle = \alpha_{bend} \frac{L_{bend}}{L_{cavity}}$$

Recall that for linear cavity lasers, the mirror loss is given by:

$$\text{(Eq. - 4.4)} \quad \langle \alpha_{mirror} \rangle = \frac{1}{L_{cavity}} \ln \frac{1}{\sqrt{r_1 r_2}}$$

where  $r_1$  and  $r_2$  are the reflection coefficients of the laser. For Ring lasers, the coupler loss is analogous to mirror loss with the following definition:

$$\text{(Eq. - 4.5)} \quad \langle \alpha_{coupler} \rangle = \frac{2}{L_{cavity}} \ln \frac{1}{\sqrt{T}}$$

As you can see, rings introduce an additional of factor of 2 in  $\langle \alpha_{coupler} \rangle$ . With these changes, the racetrack laser threshold current is expressed as follows:

$$(Eq. - 4.6) \quad I_{th} = \frac{N_{tr}^2 B q \text{Volume}_{active\ region}}{\eta_i} e^{\frac{2(\langle\alpha_i\rangle + \langle\alpha_{bend}\rangle + \langle\alpha_{coupler}\rangle)}{\Gamma_{qw} g_0}}$$

The laser differential efficiency is also modified and expressed as:

$$(Eq. - 4.7) \quad \eta_d = \frac{\eta_i \langle\alpha_{coupler}\rangle}{\langle\alpha_i\rangle + \langle\alpha_{bend}\rangle + \langle\alpha_{coupler}\rangle}$$

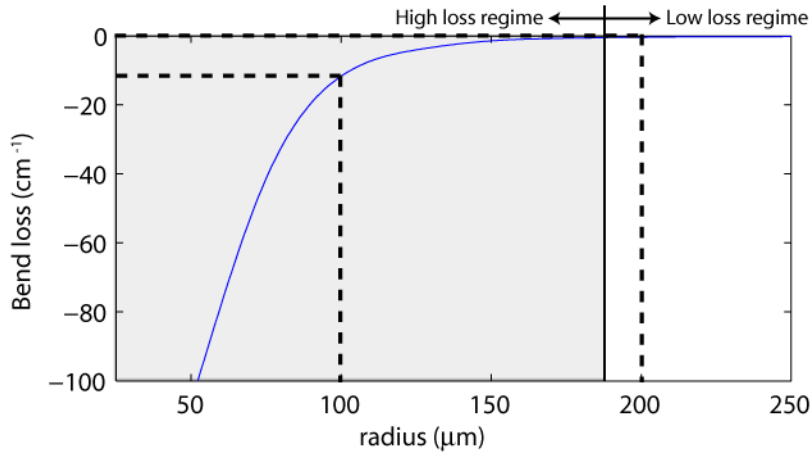


Figure 4-6. The simulated additional loss due to bending as a function of radius for the fabricated hybrid waveguide structure

In order to determine the desired T, the cavity length needs to be determined. The limiting factor for minimum cavity length of racetrack ring lasers is bend loss. Beamprop was used to calculate the bend loss as a function of bend radius (Figure 4-6). Although the absolute bend loss numbers for this calculation are not always accurate, it does give a good idea where the bend loss begins to increase rapidly. We chose radii of 200  $\mu\text{m}$  and 100  $\mu\text{m}$ , since 200  $\mu\text{m}$  is in the low loss regime while 100  $\mu\text{m}$  is a riskier design with a simulated loss of 12  $\text{cm}^{-1}$ . This brings the minimum

cavity length to 1256  $\mu\text{m}$  and 628  $\mu\text{m}$  with free spectral ranges of  $\sim 0.5$  nm and  $\sim 1$  nm, respectively.

We will focus on the radius = 200  $\mu\text{m}$  devices when we design the lasers since they lie in our conservative bend loss regime. Figure 4-7 shows three plots of (a) threshold current, (b) differential efficiency, and (c) laser output power when driven at 300 mA as a function of cavity length and coupler through-port power (T). Although this plot neglects bend loss, we denote the low bend loss regime as being cavity lengths larger than 1256  $\mu\text{m}$  and will only focus on that area. It can be seen from the panel (a) of the figure that at these lengths, varying T from 0.8 to 0.25 only increases the threshold by 20%. However, the power extraction increases by 60%. Thus, optimum coupler designs would have Ts in the range of 0.1 to 0.25.

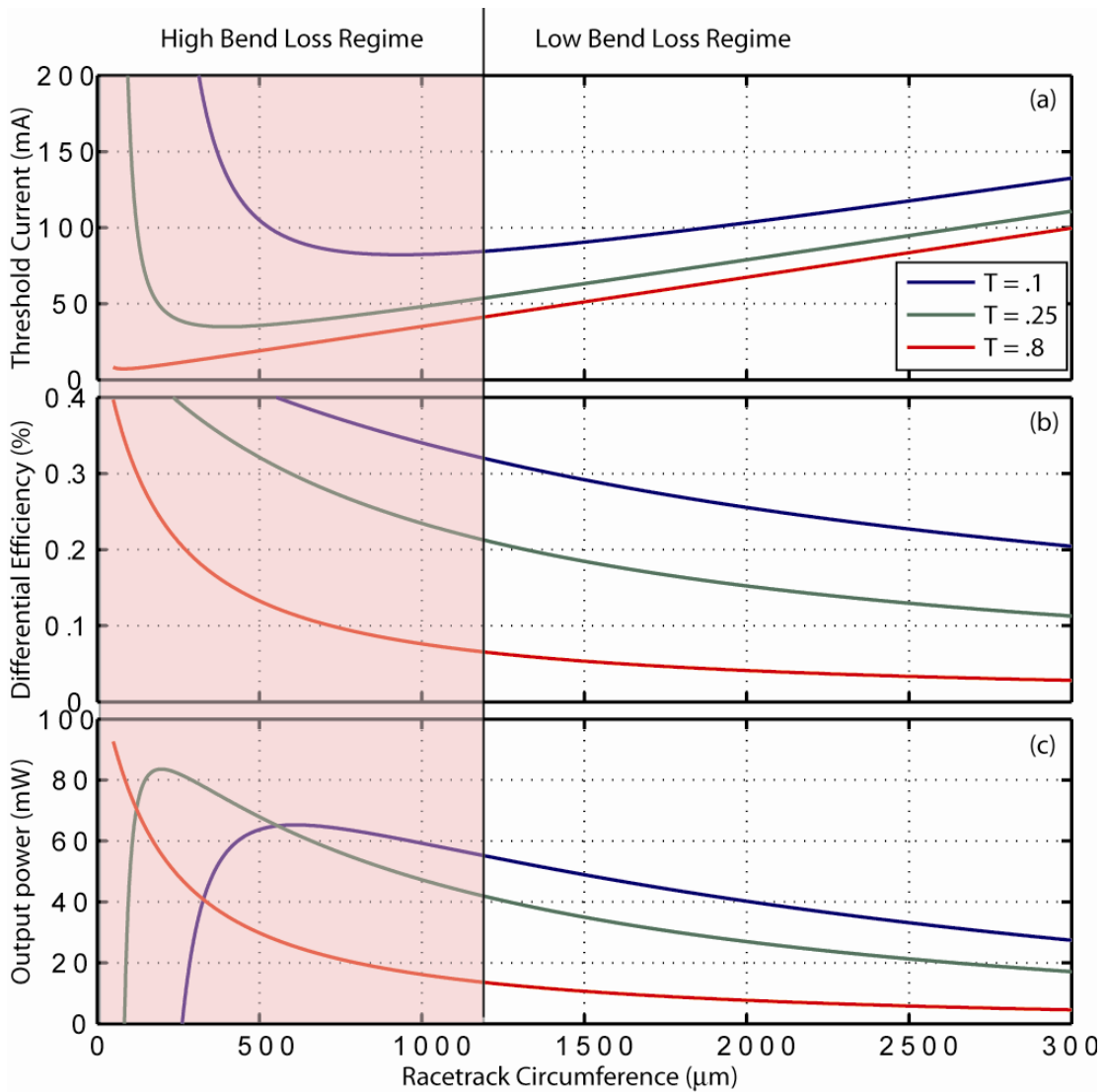


Figure 4-7 – (a) Threshold current (b) Differential efficiency, and (c) Output power at  $I = 300$  mA as a function of Length and coupler through - port power. This calculation neglects bend loss and is only valid in the low bend loss regime.

#### 4.1.1 - Directional Coupler Design

The directional coupler is designed using coupled mode theory for two modes propagating in the same direction. As this topic is widely understood, the mathematical background of coupled mode theory will not be covered here, but can

be found in references [4][5]. Instead, a brief explanation of how to understand and design the directional coupler will be given here.

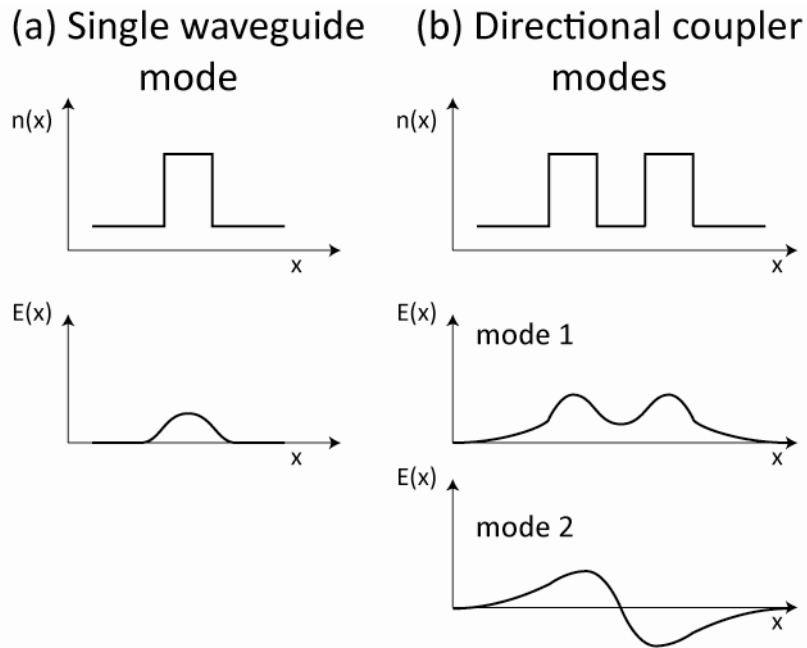


Figure 4-8 - (a) The index profile for a single mode waveguide and the E-field profile for the guided mode. (b) The index profile for two single mode waveguides placed in close proximity to form a directional coupler and the E-field profile of the two guided modes.

The index profile of a single mode waveguide and the corresponding E field mode profile are shown in Figure 4-8a. When two waveguides are placed in close proximity to form a directional coupler, the eigenmodes of this structure are no longer the same as those of the single waveguide (Figure 4-8b). The structure will have two supermodes; one will be even (mode 1), the other odd (mode 2) with propagation constants,  $\beta_1$  and  $\beta_2$ , respectively. When light is launched into one of these waveguides, it is the superposition of these two super-modes (Figure 4-8c). As the light propagates down the directional coupler, these two modes propagate at

different phase velocities. After a certain propagation length, the two modes have a 180 degree phase shift between them, resulting in a transfer of energy to the second waveguide (Figure 4-9a top). As the light continues to propagate, the phase difference will become 360 degrees, resulting in an energy transfer back again to the first waveguide. We assume the two waveguides to be identical, resulting in a sinusoidal transfer of energy from one waveguide to the other as a function of directional coupler length. Figure 4-9 illustrates this by showing the mode intensity profile (b), mode intensity plot (c) and the power in the left and right waveguide (d) as a function of propagation distance.

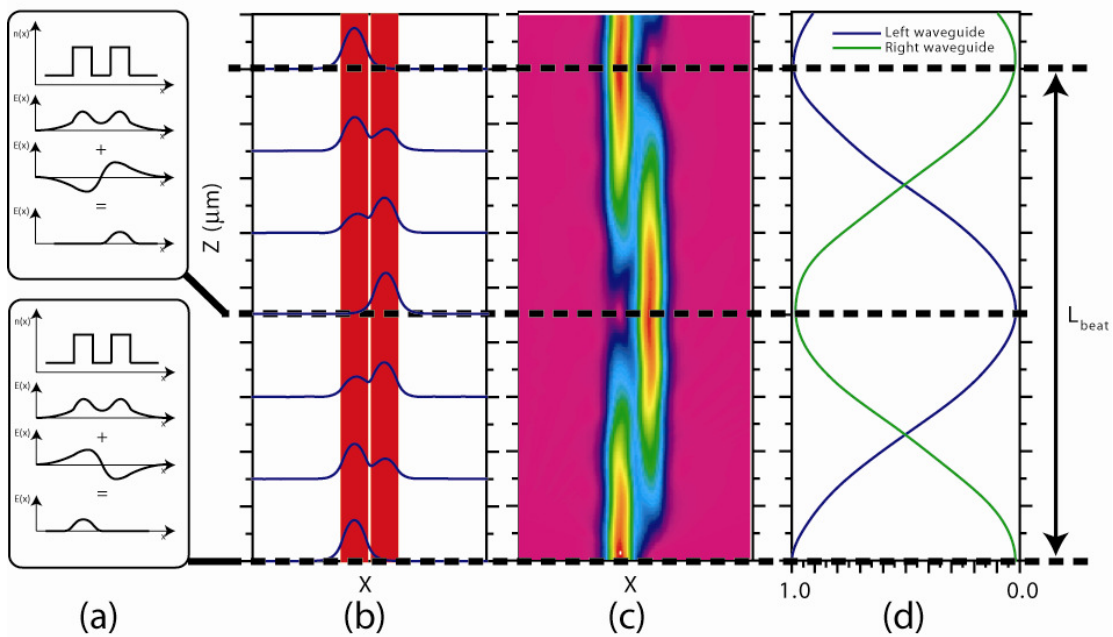


Figure 4-9 – (a) Bottom – Mode profile at input of directional coupler where the two modes are in phase. Top – mode profile where two modes are out of phase by 180 degrees. (b) Mode intensity slice profiles as a function of Z position in directional coupler (c) Mode intensity plot as a function of Z position in directional coupler (d) Power in left waveguide and right waveguide as a function of Z position in directional coupler.

The coupler beat length is defined as the coupler length in which 360 degrees of phase difference is accumulated between the two modes and is written as follows:

$$(Eq. - 4.8) \quad L_{Beat} = \frac{2\pi}{|\beta_2 - \beta_1|} = \frac{\lambda}{|n_2 - n_1|}$$

This length defines the periodicity of the coupler. The coupling power from one waveguide to the other can then be expressed as [6]:

$$(Eq. - 4.9) \quad K = \sin^2 \left( \pi \frac{L_{Coupler}}{L_{Beat}} \right)$$

while the through-port power is expressed as:

$$(Eq. - 4.10) \quad T = 1 - \sin^2 \left( \pi \frac{L_{Coupler}}{L_{Beat}} \right)$$

where  $L_{coupler}$  is the coupler length. We design the coupler by calculating the refractive indices of the first two modes of the coupler structure, and using these three expressions. The target waveguide dimensions for this generation of devices were a waveguide height, width, and rib etch depth of 0.7  $\mu\text{m}$ , 1.5  $\mu\text{m}$ , and 0.5  $\mu\text{m}$ , respectively. The minimum gap size was set at 0.6  $\mu\text{m}$  based on the resolution of the stepper projection lithography we had available to us. This structure's effective modal indices for the first and second coupler mode are 3.369, and 3.679 at 1600 nm, respectively, resulting in a beat length of 1113  $\mu\text{m}$ .

Before finalizing coupler lengths, a few simulations were conducted to understand the sensitivity of the coupler performance to fabrication error. Figure 4-10a shows a



cross section schematic of the directional coupler. Since the directional coupler's strength relies on the amount of evanescent coupling between the two waveguides, any dimension errors that influence the region in between the waveguides will alter the beat length. The beat lengths for three coupler dimension variations are plotted in Figure 4-10(b-c). Targeting errors in rib etch depth are intrinsic to this process since there is no chemically selective hard stop. This etch can be done with +/- 100 nm precision (Figure 4-10b). The waveguide width always has a degree of targeting error due to small lithographic exposure variations. As the waveguide pattern is over exposed or under exposed, the two waveguide are effectively brought closer or farther apart. We assume that this can be controlled within +/- 50 nm (Figure 4-10c). Although the etch depth between the coupler is conducted at the same time as the rib etch depth, the small gap size may slow etch rate inside this narrow trench. This is assumed to be on the order of -100 nm (Figure 4-10c). These curves show that beat length should be within +1% and - 5% of the targeted value. This targeting error is relatively small compared to rib waveguide directional couplers made out of silicon since the evanescent coupling occurs primarily in the III-V region for these deep etched waveguides.

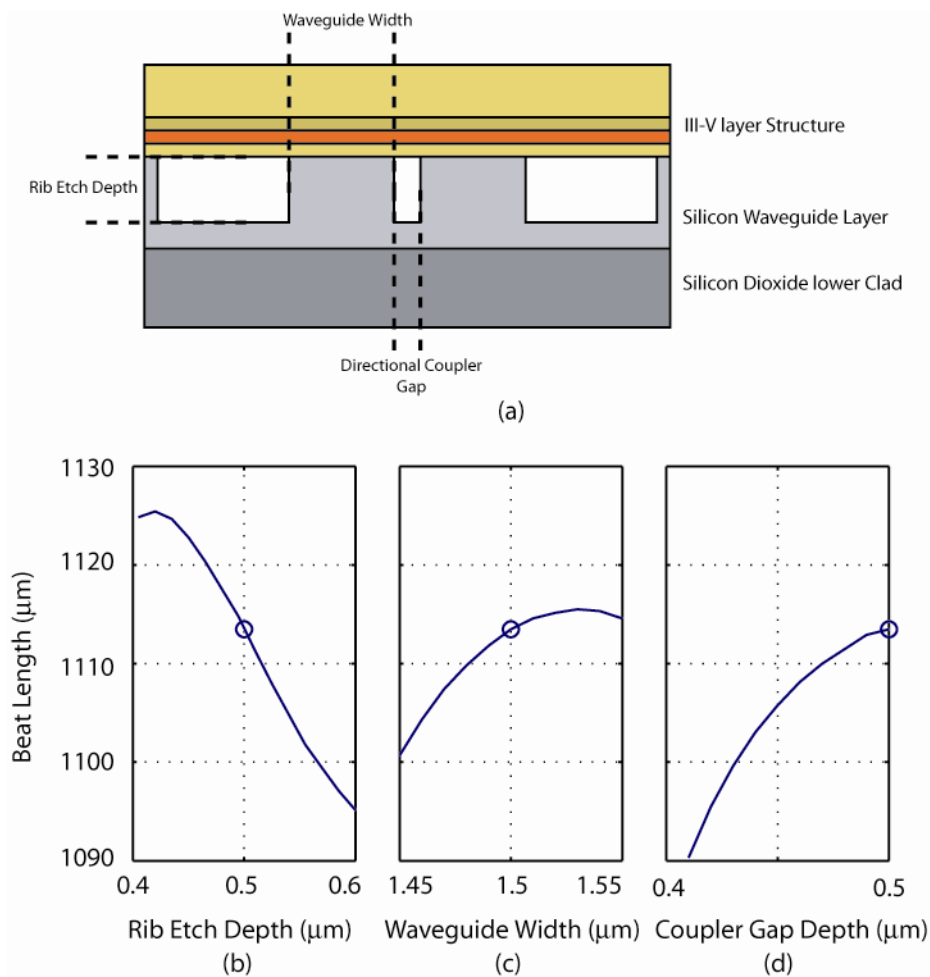


Figure 4-10 – (a) Directional coupler cross section. Beat length as a function of (b) rib etch depth, (c) waveguide width, and (d) coupler gap depth fabrication deviation. The target value is marked on each plot with a data point.

#### 4.1.2 – Device Dimensions

The fabricated waveguide width, silicon height, and rib etch depth are 1.5  $\mu\text{m}$ , 0.71  $\mu\text{m}$ , and 0.49  $\mu\text{m}$ , respectively. The resulting confinement factors for the silicon waveguide region and quantum well regions were 59.5 %, and 5.2 %, respectively.

Four device designs were fabricated with varying ring radius, and coupler lengths ( $L_{\text{interaction}}$ ). Table 4-1 shows the device layout breakdown with the corresponding

cavity lengths ( $L_{\text{cavity}}$ ). Figure 4-11 shows the calculated T value as a function of coupler length for the target dimensions and the +1% and -5% fabrication tolerance curves. We select coupler lengths of 400  $\mu\text{m}$  and 600  $\mu\text{m}$  in order to get Ts of 14 % to 20% and 1% to 6% for the 200  $\mu\text{m}$  radius devices. Higher T values are chosen for the radius 100  $\mu\text{m}$  devices in order to minimize losses. The straight sections of the racetrack ring are 700  $\mu\text{m}$  long. The total cavity lengths are listed in Table 4-1 .

Radius	$L_{\text{cavity}}$	$L_{\text{Interaction}}$
200 $\mu\text{m}$	2656 $\mu\text{m}$	600 $\mu\text{m}$ 400 $\mu\text{m}$
100 $\mu\text{m}$	2028 $\mu\text{m}$	300 $\mu\text{m}$ 100 $\mu\text{m}$

Table 4-1 - Fabricated racetrack laser dimensions

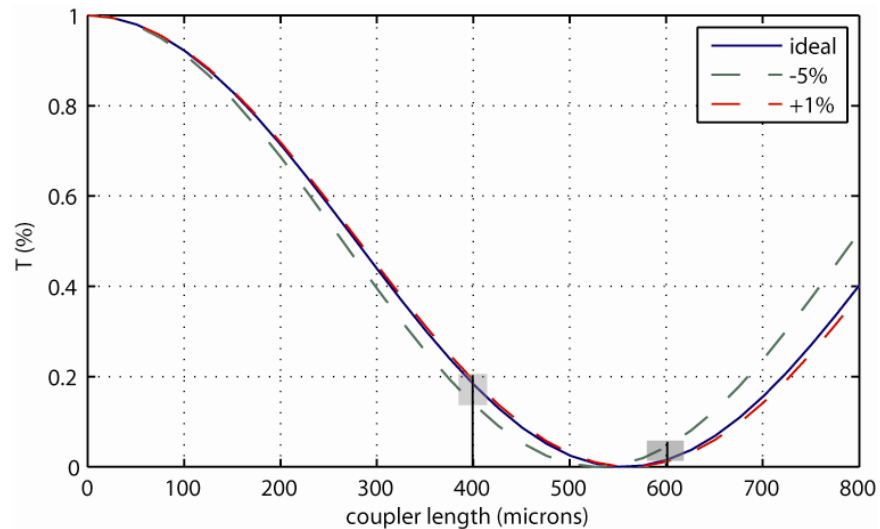


Figure 4-11 – T versus coupler length. Ideal curve and +1% to -5% curves are shown to account for fabrication variation

The laser power is collected into the two 440  $\mu\text{m}$  long photodetectors. These photodetectors have the same waveguide architecture as the hybrid laser, the only

difference being that they are reverse biased to collect photo-generated carriers.

The fabricated device SEM is shown in Figure 4-12.

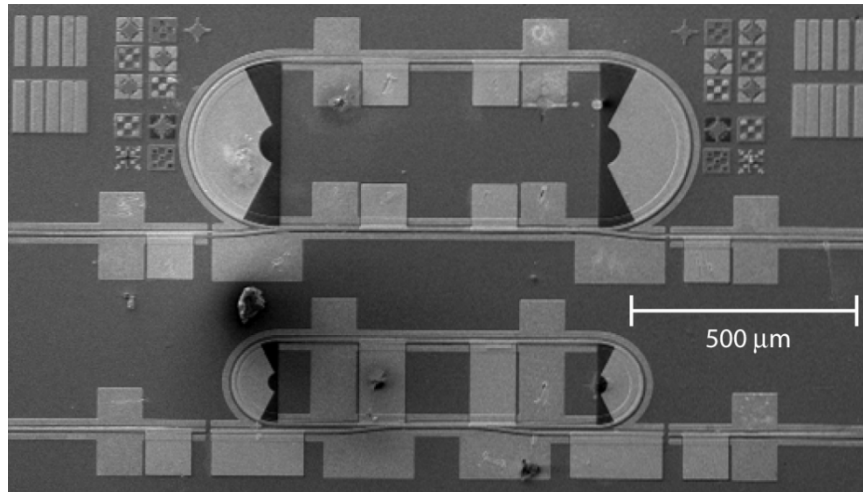


Figure 4-12) A top view SEM micrograph of two racetrack resonator lasers. The racetrack resonator lasers on the top and bottom have radii of 200 and 100  $\mu\text{m}$ , respectively

## 4.2 - Continuous Wave Lasing

The laser is driven by applying a positive bias voltage to the top p-probe contact while the optical power is measured by the two photodetectors on each side of the coupler. The photocurrent is measured while reverse biasing the photodetectors at -5V. Since the testing of the lasers are done all on chip without polishing and dicing, the lasing spectrum is measured by collecting scattered light near the bends of the ring through a fiber probe. The entire silicon chip is mounted on a TEC controller which allows the operating temperature of the laser to be varied from 0  $^{\circ}\text{C}$  to 80  $^{\circ}\text{C}$ .

The responsivity of the photodetectors was measured by dicing and polishing a discrete detector in the same chip and launching a laser light into the detector

through a lensed fiber. The fiber coupled responsivity was measured to be 0.25 A/W at 1580 nm. Taking into consideration the  $\sim 30\%$  reflection off the waveguide facet and an estimated 5.25 +/- .25 dB coupling loss, we estimate the photodetector responsivity to be in the range of 1.25 - 1.11 A/W [7]. This corresponds to an internal quantum efficiency between 97%-86% and is comparable to the  $\sim 1$  A/W responsivity of Ge on SOI waveguide photodetectors reported in reference [8]. We use a responsivity of 1.25 A/W in the remainder of this paper such that the laser power values are on the conservative side. The detector dark current was 200  $\mu$ A.

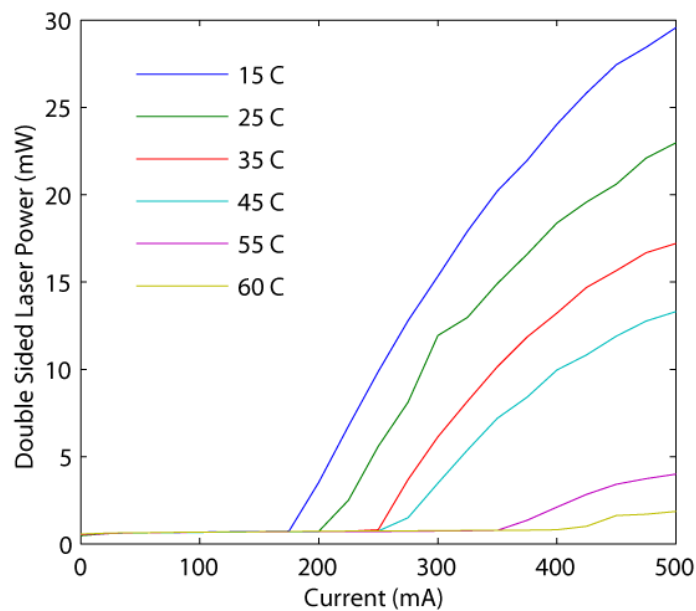


Figure 4-13. The LI curve for a racetrack laser with radius  $R = 200 \mu\text{m}$ , and  $L_{\text{interaction}} = 400 \mu\text{m}$  for various temperatures

Figure 4-13 shows the measured total c.w. laser output power which is the sum of the optical power measured at both detectors as a function of injected current for various operating temperatures ranging from 15 to 60  $^{\circ}\text{C}$  for the laser with a ring

radius and coupling interaction length of 200  $\mu\text{m}$  and 400  $\mu\text{m}$  respectively. As can be seen from Fig. 4-13, the laser threshold is 175 mA with a maximum output power of 29 mW at 15  $^{\circ}\text{C}$ . The maximum power is limited by the available drive current to the device. The laser has a 60  $^{\circ}\text{C}$  maximum lasing temperature with a characteristic temperature of 55 K. The laser has a threshold voltage of 1.75V and a series resistance of 3.5 ohms.

Figure 4-14 shows the measured multi-mode lasing spectrum of the laser driven at 240 mA. The spectrum was measured with an HP 70952A optical spectrum analyzer with a resolution bandwidth of 0.1 nm. The lasing wavelength is 1592.5 nm with a 0.21 nm mode spacing corresponding to a group index of 3.67.

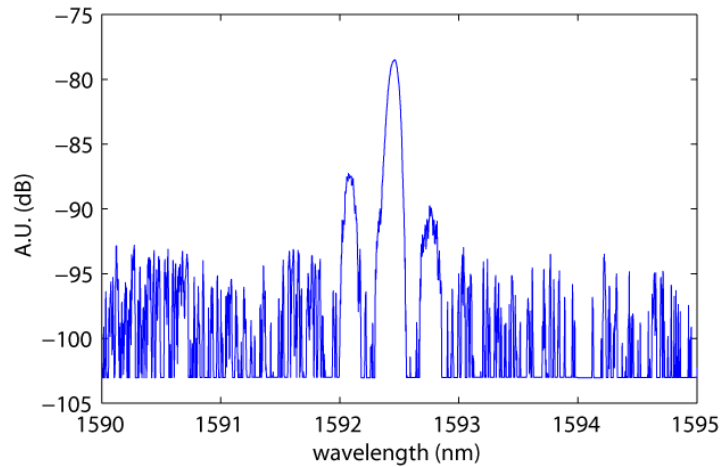


Fig. 4-14. The hybrid racetrack laser spectrum taken at 240 mA for a  $R = 100 \mu\text{m}$ ,  $L_{\text{interaction}} = 400 \mu\text{m}$

Radius	$L_{\text{Interaction}}$	$P_{\text{max}}$	$\eta_d$	$I_{\text{th}}$	$T_{\text{max}}$
200 $\mu\text{m}$	600 $\mu\text{m}$	29 mW	17%	175 mA	60 C
	400 $\mu\text{m}$	27.5 mW	13%	175 mA	60 C
100 $\mu\text{m}$	300 $\mu\text{m}$	3.1 mW	12%	200 mA	65 C
	100 $\mu\text{m}$	7 mW	4.3%	150mA	65 C

Table 4-2: Max power, differential efficiencies, threshold currents and maximum operating temperatures for the fabricated racetrack lasers

Table 4-2 shows the maximum output powers, differential efficiencies, threshold currents, and maximum output temperatures of the four device designs. The threshold current for these devices can be reduced by shortening the cavity lengths. The proton implant profile could also be optimized for improved injection efficiency which would further lower threshold currents and increase the differential efficiency.

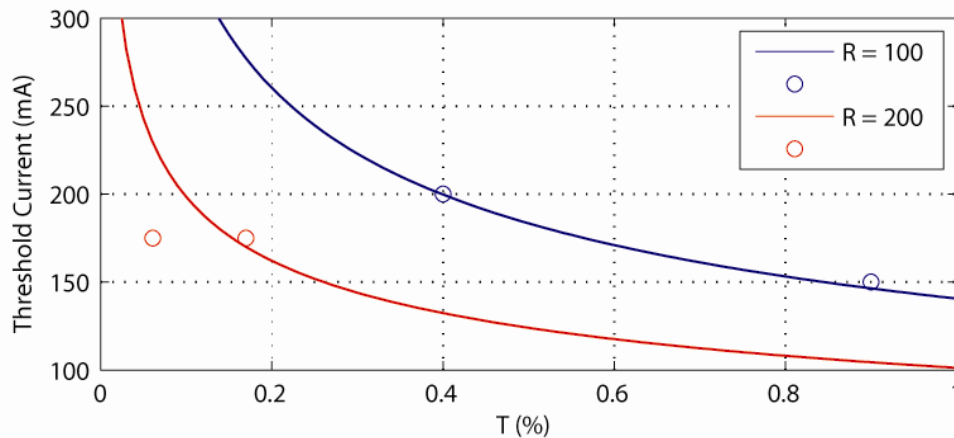


Fig. 4-15: The experimental and fitted threshold currents for the four fabricated racetrack lasers

The experimentally fitted threshold currents are shown in Fig. 4-15. The laser parameters, such as injection efficiency, and modal loss, were kept fixed from the threshold simulations made in the previous chapter. The additional bend loss for 200

$\mu\text{m}$  and  $100 \mu\text{m}$  bends were found to be  $0 \text{ cm}^{-1}$  and  $50 \text{ cm}^{-1}$ , respectively. The discrepancy between the  $45 \text{ cm}^{-1}$  experimental bend loss and  $12 \text{ cm}^{-1}$  simulated bend loss for  $R = 100 \mu\text{m}$  data point may be attributed to the rapid change in that region of the simulated curve or the absence of sidewall roughness in the simulation. Small deviations in the exact index values can cause significant changes in the simulated values.

#### *4.2.2 – Unidirectional C.W. lasing*

Mode hopping between the degenerate clockwise and the counterclockwise propagating modes is traditionally a problem for ring lasers. Since these two modes have spatially separated outputs, mode competition can be observed by looking at the L-I curves of the individual modes. The mode hopping produces kinks in the single output L-I curves, as seen in the top panel of Fig. 4-16. This can be overcome and unidirectional lasing achieved by seeding one mode over the other with an external light source. We demonstrate an integrated version of this by forward biasing one of the photo-detectors to use as an amplified spontaneous emission (ASE) light source. Here the detector on the left of the laser (shown in Fig. 4-5) is forward biased and used to seed the racetrack laser. As light is generated in the ASE source, the photon density of the counter clockwise propagating mode is greater than the photon density of the clockwise propagating mode, creating a differential in the amount of stimulated emission occurring in these two modes. This ultimately leads



to controlled unidirectional lasing [9]. Fig. 4-16 shows the LI curve for the counter clockwise mode at three forward current levels on the left “detector” for the  $R = 100 \mu\text{m}$ ,  $L_{\text{interaction}} = 100 \mu\text{m}$  device. It can be seen that at 50 mA forward detector current, the output power is unstable due to mode hopping. At 75 mA forward detector current, this L-I becomes smoother, and at 100 mA, the counter clockwise propagating mode achieves stable lasing.

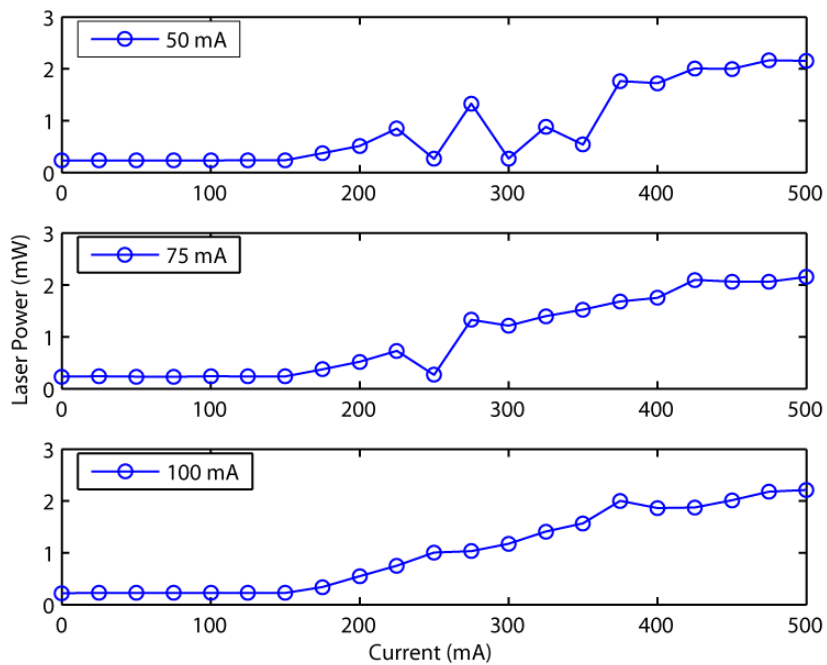


Figure 4-16. The LI curve for the clockwise lasing mode for three forward bias currents for the photodiode on the left of a laser with  $R = 100 \mu\text{m}$ , and  $L_{\text{interaction}} = 100 \mu\text{m}$ .

### 4.3 - Mode Locked Racetrack Lasers

Mode locked lasers operate by lasing in many modes simultaneously. These modes are phase correlated giving unique spectral and temporal properties. In the time

domain, their modes add up constructively and destructively such that the laser outputs short pulses with a fixed repetition rate. In the spectral domain, the laser outputs a stable frequency comb. These properties allow mode locked lasers to be used as a short pulse source for optical time division multiplexing (OTDM) applications, or a frequency comb source for wavelength division multiplexing (WDM) sources. The racetrack resonator topography is particularly interesting for mode locked lasing since its feedback is inherently broadband, allowing for lasing in many modes. Additionally, they are independent of facet preparation, so their repetition frequency can be controlled very precisely through lithography and they can be integrated with other photonic devices [10][11][12][13].

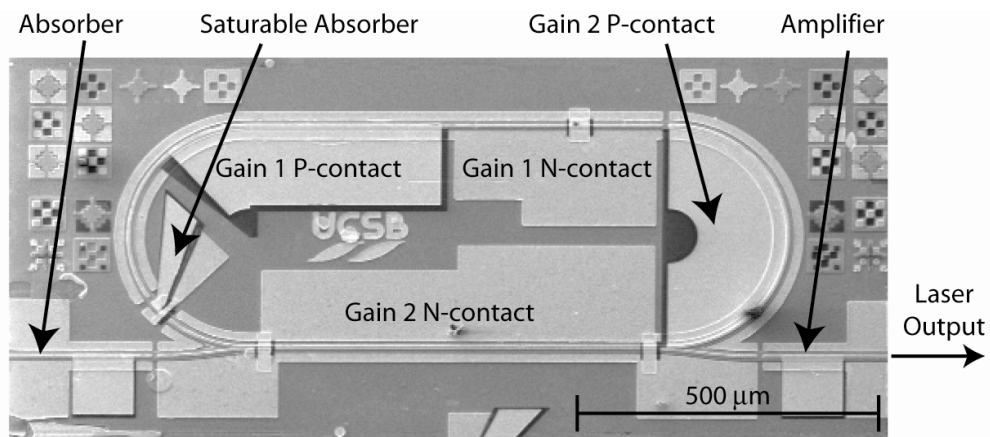


Figure 4-17: Scanning electron micrograph of a racetrack mode locked silicon evanescent laser.

We fabricated mode locked racetrack lasers by adding an electrically isolated 30 μm long saturable absorber inside the racetrack cavity as shown in Figure 4-17. The gain section is separated into two sections with lengths of 1.13 mm and 1.467 mm to

allow for another degree of freedom in device performance control. These sections are separated by 10  $\mu\text{m}$  long unpumped regions that have undergone proton implantation to achieve electrical isolation [14]. The two gain sections 1 and 2 are both forward biased in parallel at 410 mA. The device was operated in two modes: passive mode-locked and hybrid mode-locked. In passive mode locking a DC bias is applied to the saturable absorber in order to adjust the carrier lifetime in the saturable absorber, ultimately tuning the response on the saturable absorber. We use a DC bias of -0.66 volts in the data reported here, unless noted otherwise. In hybrid mode-locking, an additional RF signal is applied with the DC bias in order to actively gate the saturable absorber at the mode locked laser repetition rate. Mode-locking occurs via colliding pulse mode-locking (CPM) with clockwise and counter clockwise pulses colliding simultaneously in the saturable absorber at a rate  $\sim 30$  GHz as determined by the following expression:

$$\text{(Eq. - 4.11)} \quad f_{\text{repetition}} \approx \frac{c}{n_{\text{group}}L_{\text{cavity}}}$$

where  $c$ ,  $n_{\text{group}}$ , and  $L_{\text{cavity}}$  are the speed of light, the group index, and the round trip cavity length, respectively. Light is coupled out of the resonator through a 400  $\mu\text{m}$  long directional coupler. The coupler output facets were diced, polished, and anti-reflection coated with a single layer quarter wavelength  $\text{Ta}_2\text{O}_5$  dielectric coating. The clockwise lasing pulses are coupled out of the resonator into a reverse biased section of active region acting as an anti-reflection absorber. The counter-clockwise

lasing pulses are coupled out of the resonator and amplified through an integrated SOA before being collected by a lensed fiber. The output amplifier is biased at 47 mA producing an estimated  $\sim 4$  dB of gain based on the current density and length. The coupling loss was measured to be 13 dB by reverse biasing the amplifier and measuring the detected photocurrent and comparing this to the fiber coupled output power. In order to avoid removal of critical device components, facet polishing was minimal, leading to poor facet quality and the resulting higher coupling losses than previously reported [15]. The device is temperature stabilized on a stage held at 10 °C.

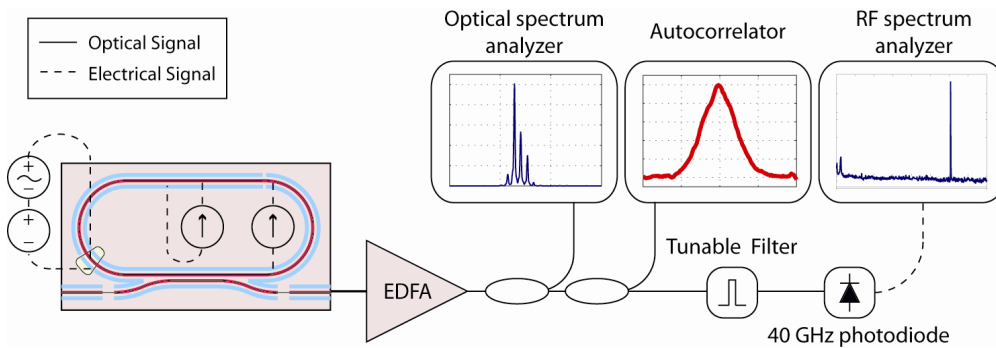


Figure 4-18: Racetrack ML-SEL experimental set up.

The device characteristic measurement set up allows simultaneous monitoring of the pulse train in the wavelength domain, time domain, and RF frequency domain, as shown in Figure 4-18. The ML-SEL pulses were collected by a lensed fiber and amplified through an EDFA. The signal is first split with 50% going to an optical spectrum analyzer, and the other 50% to a second 50/50 splitter. The outputs of the second splitter are sent to an autocorrelator and through a 1.2 nm wide tunable

notch filter to a 40 GHz bandwidth photodetector. The electrical signal from the photodetector is sent to a DC - 41 GHz RF spectrum analyzer.

#### *4.3.2 - Experimental Results*

When all sections (gain 1, gain 2, and the saturable absorber) are connected and forward biased together in parallel, the laser threshold was measured to be 250 mA. The autocorrelator pulse traces for *passive mode-locking and hybrid modelocking* are showed in Figure 4-19a. It can be seen that traces under these two modes of operation are almost identical. The auto-correlated pulse width was measured at 10 ps. A 7 ps pulse width is estimated by assuming a Gaussian pulse shape. The pulse width as a function of saturable absorber bias is shown in Figure 4-19b, with a minimum at the reported bias of -0.66V. The average power of the counter clockwise pulses is measured at 1.92 mW by reverse biasing the right SOA and measuring the collected photocurrent. We assume 100% internal quantum efficiency for the SOA acting as a photodetector to underestimate the power of the laser. This corresponds to a peak pulse power of 8.57 mW by taking into account the repetition rate of the laser and Gaussian pulse shape. The optical spectrum under passive and hybrid mode-locking is shown in Figure 4-20. It can be seen that the spectrum does not change noticeably between these two mode-locking modes. The optical spectrum is centered at 1588.75 nm has a 0.5 nm spectral width. This

corresponds to a time bandwidth product of 0.42, indicating that the pulses are transform limited.

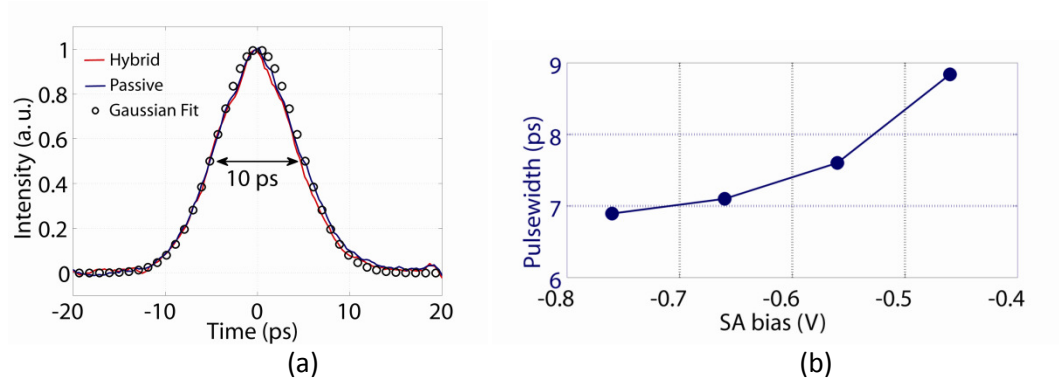


Figure 4-19: (a) Passive mode-locked and hybrid mode-locked autocorrelation trace.(b) Deconvolved pulse width versus saturable absorber bias.

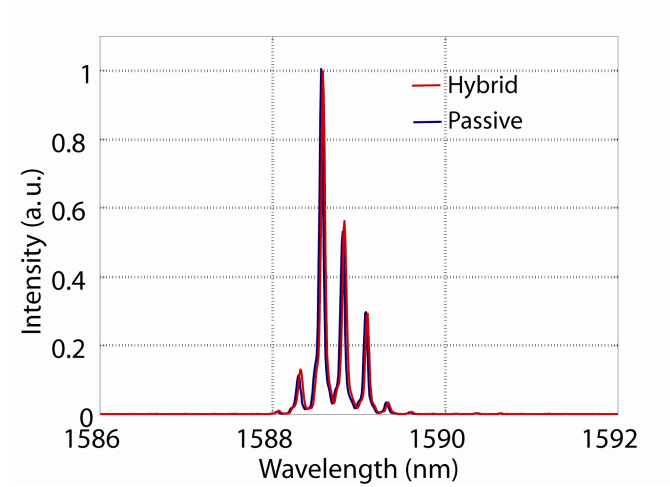


Figure 4-20: The passive and hybrid mode-locked optical spectrum. The spectrum does not change noticeably between the two mode-locking modes.

The RF spectrum is shown in Figure 4-21a under passive and hybrid mode locking with a 13 dBm 30.35 GHz RF signal. It can be seen that for hybrid mode locking, the RF spectrum narrows substantially, indicating a large reduction in signal jitter. Figure 5b shows the passively mode locked and actively mode locked RF spectrum over a

range of 40 GHz. It can be seen that the extinction ratio between the 30 GHz tone and the device relaxation resonance is greater than 45 dB, giving clear evidence of mode locking. In addition, the 30 GHz tone is greater than 40 dB above the measurement noise floor. The absolute timing jitter was calculated by integrating two times the single sideband noise of the mode locking RF peak. Figure 4-22 shows the jitter under hybrid mode locking versus the upper integration limit. It can be seen that for the frequency range of 1 kHz to 100 MHz offset from the repetition frequency, the laser has an absolute jitter of 364 fs which is well below the ITU specification of 3.3ps for digital transmission at a 30 GHz repetition rate (0.1 times the bit period).

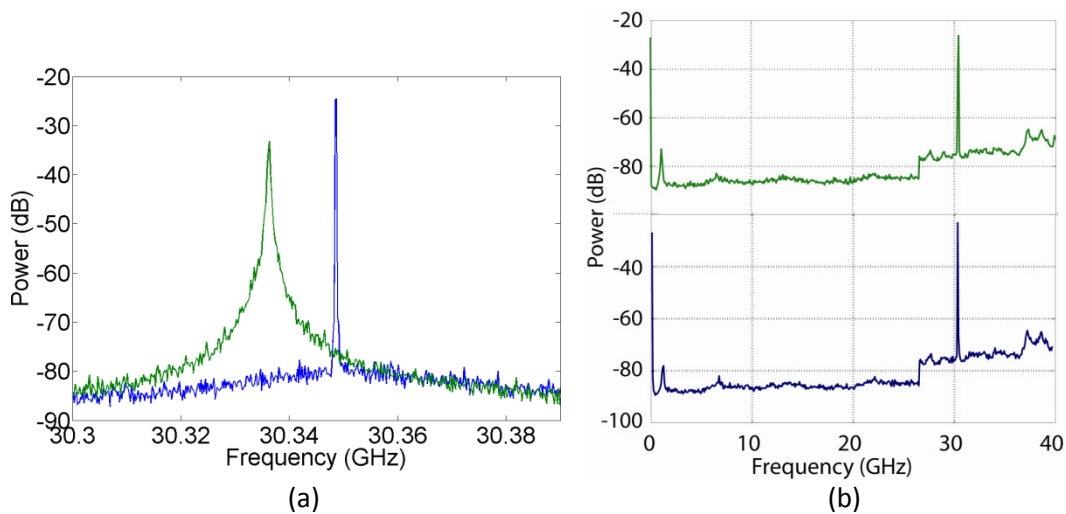


Figure 4-21: (a) RF spectrum of passively and hybridly locked mode locked laser measured with a 10 kHz resolution bandwidth. (b) Wide RF spectrum of the MLL under passive locking (green) and hybrid locking (blue).

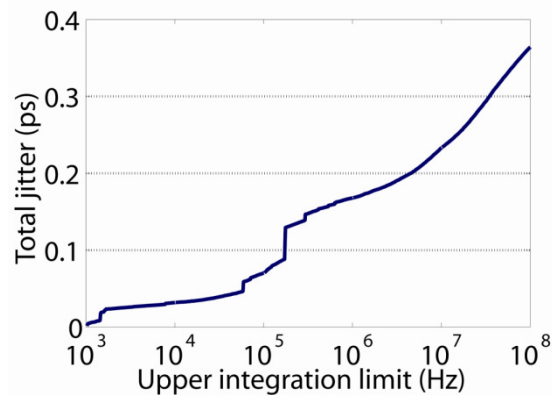


Figure 4-22: Jitter shown for single side band integration ranges from 1 kHz to 100 MHz.

The dependence of the hybrid mode locked performance on drive power when driven with the fundamental (30 GHz) drive frequency is shown in Fig. 4-23. As expected, the jitter reduces while the locking range increases with RF power with a maximum measured locking range of 50 MHz at 13.5 dBm. Since the cavity length is lithographically defined, only variations in the repetition rate detuning or group index of refraction can cause inconsistencies in the repetition rate among different devices. These inconsistencies could result from material variations, waveguide dimension variations, or other processing inconsistencies, but are likely to be very small for devices with the same design. The locking range of this device should easily compensate for any variation among different devices and fabrication process runs. It is likely that much lower locking ranges, such as those for low RF injection powers, would also be sufficient to achieve precise, repeatable mode locking frequencies using this type of device.



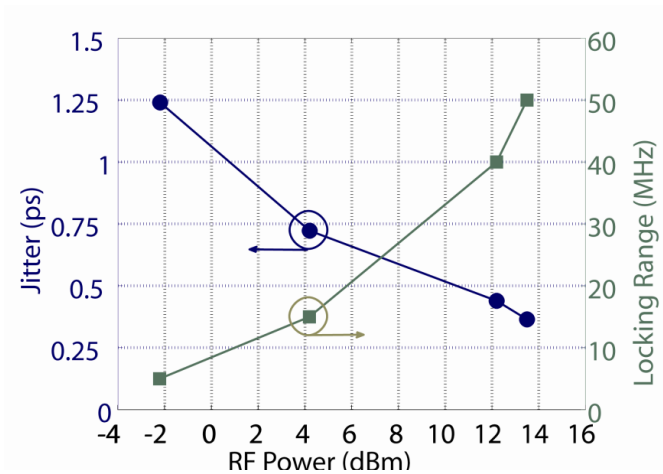


Figure 4-23: Jitter measured with a 1 kHz-100 MHz integration range and locking range versus RF powers for fundamental and sub-harmonic synchronization.

#### 4.4 - Summary

Racetrack lasers based on this second generation structure were presented in this chapter. The lasers operated continuous wave with a maximum output power of 29 mW and a maximum operating temperature of 60 °C. Mode locked operation was demonstrated with a repetition rate, and pulse width of 30 GHz, and 7 ps, respectively. Both passive and hybrid mode-locking have been achieved with the hybrid mode-locking showing a minimum jitter of 364 fs, making it well within the ITU specifications for digital data transmission.

## References

- [1] M. Sorel, P. J. R. Laybourn, A. Scir, S. Balle, G. Giuliani, R. Miglierina, and S. Donati, "Alternate oscillations in semiconductor ring lasers," *Opt. Lett.*, vol. 27, pp. 1992-1994, 2002.
- [2] M. Sorel, P. J. R. Laybourn, A. Scir, S. Balle, G. Giuliani, R. Miglierina, and S. Donati, "Alternate oscillations in semiconductor ring lasers," *Opt. Lett.*, vol. 27, pp. 1992-1994, 2002.
- [3] F. C. Cheng, "Investigation of a dye ring laser with backscattering," *Physical Review A*, vol. 45, pp. 5220, 1992.
- [4] S. L. Chuang, *Physics of Optoelectronic Devices*. New York: John Wiley & Sons, Inc., 1995 pp. 297
- [5] L. A. Coldren and S. W. Corzine, *Diode Lasers and Photonic Integrated Circuits*. New York: John Wiley & Sons, Inc., 1995 pp. 282-299
- [6] L. A. Coldren and S. W. Corzine, *Diode Lasers and Photonic Integrated Circuits*. New York: John Wiley & Sons, Inc., 1995 pp. 289
- [7] H. Park, A. W. Fang, R. Jones, O. Cohen, M. J. Paniccia, and J. E. Bowers, "A hybrid AlGaInAs-silicon evanescent waveguide photodetector," *Opt. Express*, 15, 6044-6052, (2007).
- [8] J. Liu, D. Pan, S. Jongthammanurak, K. Wada, L. C. Kimerling, and J. Michel, "Design of monolithically integrated GeSi electro-absorption modulators and photodetectors on a SOI platform," *Opt. Express* 15, 623-628 (2007)
- [9] P. Dragic, "Injection seeded Q-switched fiber ring laser", *IEEE Phot. Tech. Lett.* 16, No 8, 1822- 1824 (2004)

- [10] E. A. Avrutin, J. H. Marsh, and E. L. Portnoi, "Monolithic and multi-gigahertz mode locked semiconductor lasers: constructions, experiments, models, and applications," *IEE Proc. Optoelectron.* 147, 251-278 (2000).
- [11] T. Ohno, H. Ishii, S. Matsuo, H. Okamoto, Y. Kawaguchi, Y. Kondo, T. Furata, H. Ito, and Y. Yoshikuni, "Hybrid Modelocking of semiconductor ring lasers incorporating passive deep-ridge waveguides," *Electron. Lett.* 38, 884-886 (2002).
- [12] Y. Barbarin, E. A. J. M. Bente, M. J. R. Heck, Y. S. Oei, R. Nötzel and M. K. Smit, "Characterization of a 15 GHz integrated bulk InGaAsP passively modelocked ring laser at 1.53 $\mu$ m," *Opt. Express* 14, 9716 (2006).
- [13] S. Yu, T. F. Krauss, and P. J. R. Laybourn, "Mode Locking in Large Monolithic Semiconductor Ring Lasers," *Proc. of SPIE* 3278, 139-148 (1998).
- [14] H. Boudinov, H. H. Tan, & C. Jagadish., "Electrical isolation of n-type and p-type InP layers by proton bombardment," *J. Appl. Phys.* 89-10, 5343-5347, (2001).
- [15] B. R. Koch, A. W. Fang, O. Cohen, and J. E. Bowers, " Mode -locked silicon evanescent lasers," *Opt. Express* 15, 11225-11233 (2007).

## **Chapter 5 –Distributed Feedback Silicon Evanescent Lasers**

Although Fabry-Perot and long diameter racetrack ring lasers may have 15 db or so of side-mode suppression under certain CW operating conditions, this condition degrades under high current injection. These lasers also suffer from strong wavelength chirp when modulated, leading to high chromatic dispersion through optical fibers, ultimately limiting their bandwidth-distance product. Distributed feedback lasers are attractive for optical communications since they have a single longitudinal mode output and their short cavity lengths allow for low threshold currents while still producing output powers in the mW regime [1]. Since their output wavelength is determined by grating pitch, their chirp is much smaller than Fabry Perot's and their wavelength can be controlled very accurately for use in wavelength division multiplexing (WDM) applications. Figure 1 shows a concept for a silicon terabit transmitter utilizing hybrid integration. 25 distributed feedback lasers, each spaced at a frequency spacing of 100 GHz, are externally modulated at 40 Gb/s [2] and then multiplexed together into a single waveguide to form a wavelength division multiplexed 1 Tb/s data stream. Although micro-disk lasers yield single wavelength output, their wavelength selection is determined by the round trip cavity length; a parameter strongly dependent on fabrication variations, making wavelength targeting a challenge. In addition, their small size leads to high thermal impedance, which currently limits their maximum demonstrated continuous wave

operating temperature on silicon to 20 °C [3]. Grating based lasers, on the other hand, are more dependent on grating periodicity rather than duty cycle for wavelength selection, giving them increased wavelength targeting tolerance. Optically pumped III-V distributed feedback (DFB) membrane lasers on silicon-on-insulator (SOI) have been demonstrated with maximum output powers of 125 nW [4]. In this chapter, we present the use of distributed Bragg reflectors (DBR) to realize electrically pumped distributed feedback (DFB) silicon evanescent lasers [5] for wavelength selectivity. The first part of the chapter discusses the design and fabrication of gratings while the remainder of the chapter focuses on the demonstration of a DFB silicon evanescent laser.

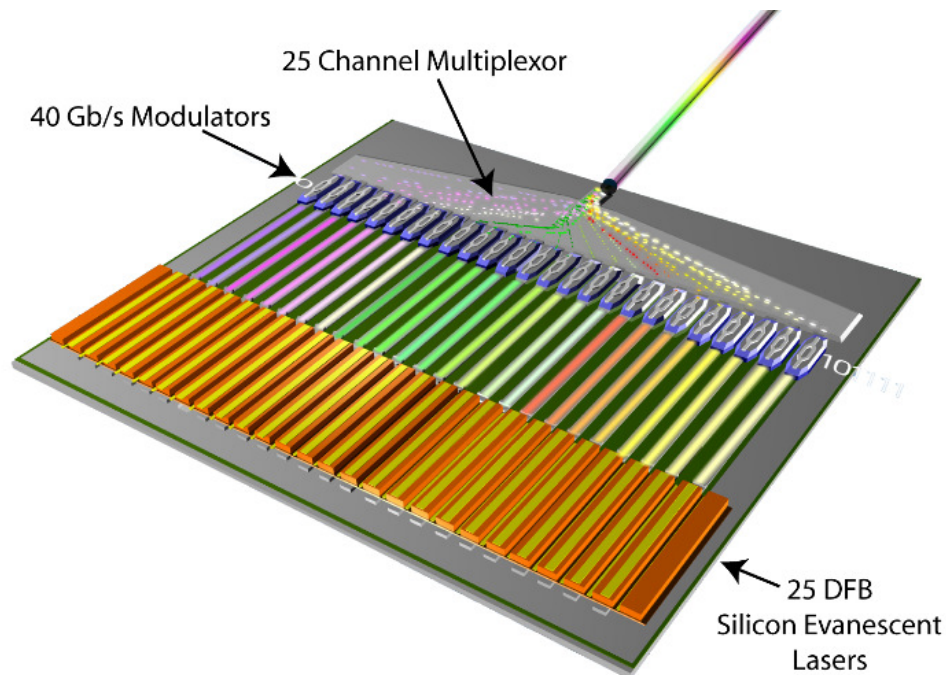


Fig. 5-1 - A proposed silicon terabit transmitter with 25 DFB-SELs externally modulated at 40 Gb/s.

## 5.1 – Bragg Grating Design and Fabrication

Bragg gratings are periodic structures whose refractive indices alternate periodically along the direction of propagation. As light propagates down this structure, reflections occur at the interfaces between the layers where there is a change in the refractive index, coupling the forward and backward propagating waves. The coupling of the forward and backward propagating waves in this structure, creates an anti-resonant condition where light with wavelengths of integer multiples of twice the grating period are off resonance with the structure and are therefore reflected with the greatest magnitude. This is expressed by the Bragg condition at normal incidence in Eq. 5-1 [6]:

$$(Eq. 5-1) \quad m\lambda = 2\Lambda$$

where  $\lambda$ , and  $\Lambda$  are the wavelength of light in the material and the period of the grating respectively. The variable,  $m$ , denotes the order of the grating. In this work we focus on first order gratings, where  $m$  is equal to 1, since these structures are less sensitive to variations in duty cycle. Gratings in waveguides are realized by modulating the waveguide effective index down the direction of propagation. This can be done either by modulating the waveguide width or height. Figure 5-2 (a) shows a diagram of the grating structure in our DFB-SELs. We create a periodic index variation by etching a surface corrugation on the top surface of the silicon waveguide. The III-V structure is bonded to the top of this waveguide to provide

gain. The coupled mode theory analysis of Bragg gratings is covered extensively in reference [7], and will not be reviewed here. Instead, we will use widely known equations to calculate the behavior of our fabricated gratings.

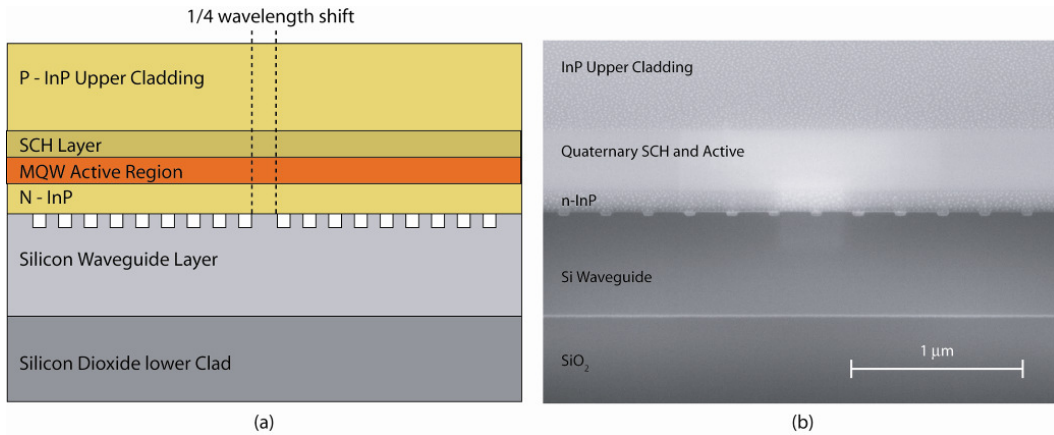


Fig 5-2 – (a) DFB-SEL longitudinal cross section diagram (b) Scanning electron microscope image of DFB-SEL longitudinal cross section.

The reflection of the grating per unit length is the grating coupling constant,  $\kappa$ . For a square wave index profile,  $\kappa$  is expressed as follows:

$$(Eq\ 5-2) \quad \kappa = \frac{1}{\Lambda} \frac{\Delta n}{\langle n \rangle} \sin(m * \pi * D)$$

where  $\Delta n$ , and  $\langle n \rangle$  are the difference in index between the two regions, and the mean index between the two regions, respectively. The grating duty cycle,  $D$ , is defined as the ratio between the length of the higher index region over the length of the grating.  $\kappa$  is useful for the characterization of gratings for DFBs and distributed Bragg reflectors (DBRs). For example, a high  $\kappa$  grating will give a higher reflectivity

than a low  $\kappa$  grating for the same number of grating periods due to the higher index contrast achieved at each of the interfaces.

The gratings are formed by depositing a 50 nm PECVD SiO<sub>2</sub> hard mask onto the unpatterned silicon on insulator wafer. The hard mask is patterned with electron-beam lithography and inductively coupled plasma dry etching to form a ~25 nm surface corrugated grating with a 238 nm pitch and 71 % duty cycle. The grating stop-band is designed at around 1600 nm, in order to account for the spectral shift seen in devices due to device heating, as described in Chapter 3 and 4. Next, silicon waveguides are formed by depositing a 200 nm SiO<sub>2</sub> hard mask and patterning with projection lithography and a second ICP dry etch. The silicon waveguide has a width, height, and rib etch depth of 1.5  $\mu\text{m}$ , 0.7  $\mu\text{m}$ , and 0.5  $\mu\text{m}$ , respectively. This yields a quantum well confinement factor of 5.2% and a silicon confinement factor of 59.2%. The III-V structure was then bonded to the silicon wafer and processed as described in Chapter 2. Figure 5-2 (b) shows a cross sectional scanning electron microscope image of the fabricated device. The effective indices of the unetched and etched regions calculated using the film mode matching (FMM) method are found to be 3.3688 and 3.3441, respectively. This results in a grating  $\kappa$  of  $\sim 247 \text{ cm}^{-1}$ . The  $\kappa$  of these gratings are large when compared to the  $73 \text{ cm}^{-1}$   $\kappa$  of surface corrugated gratings on passive silicon rib waveguides of similar dimensions since the index difference between air and silicon is quite large and the index perturbation is



located near the center of the optical mode. The grating is 340  $\mu\text{m}$  long with a  $\frac{1}{4}$  wavelength shift in the center of the grating. The grating is essentially a 1-D photonic band gap structure, with a band gap at the Bragg wavelength. By adding a  $\frac{1}{4}$  wavelength shift at the center of the structure, we create a defect in this structure, allowing for a mode to exist in the center of the laser at the Bragg wavelength. Typical DFBs are designed to have  $\kappa L$  of 1 for critical coupling, where  $L$  is the length of the grating [8]. Since we want to minimize thermal impedance by keeping the device a little longer, and these hybrid gratings have an intrinsically high  $\kappa$ , we operate in a higher regime where  $\kappa L = 8$ . This number should be reduced in future generations, for improved power extraction and higher differential quantum efficiency.

## *5.2 – Distributed Feedback Silicon Evanescent Laser*

The top of Figure 5-3 shows the device layout. The DFB-SEL consists of a 200  $\mu\text{m}$  long gain region. 80  $\mu\text{m}$  long tapers are formed by linearly narrowing the III-V mesa region above the silicon waveguide. This adiabatically transforms the mode from the hybrid waveguide to the passive silicon waveguide resulting in losses on the order of 1.2 dB per taper and reflections on the order of  $6 \times 10^{-4}$  [9]. Two tapers are placed on both ends of this gain region and are also electrically pumped, contributing to a small amount of optical gain. Silicon evanescent photo-detectors are placed on both sides of the laser in order to enable on-chip testing of the DFB-SEL performance. The

photo-detectors are 240  $\mu\text{m}$  long including the two 80  $\mu\text{m}$  long tapers. The detector to the right is placed 400 microns away in order to allow room for dicing and polishing for off chip spectral tests.

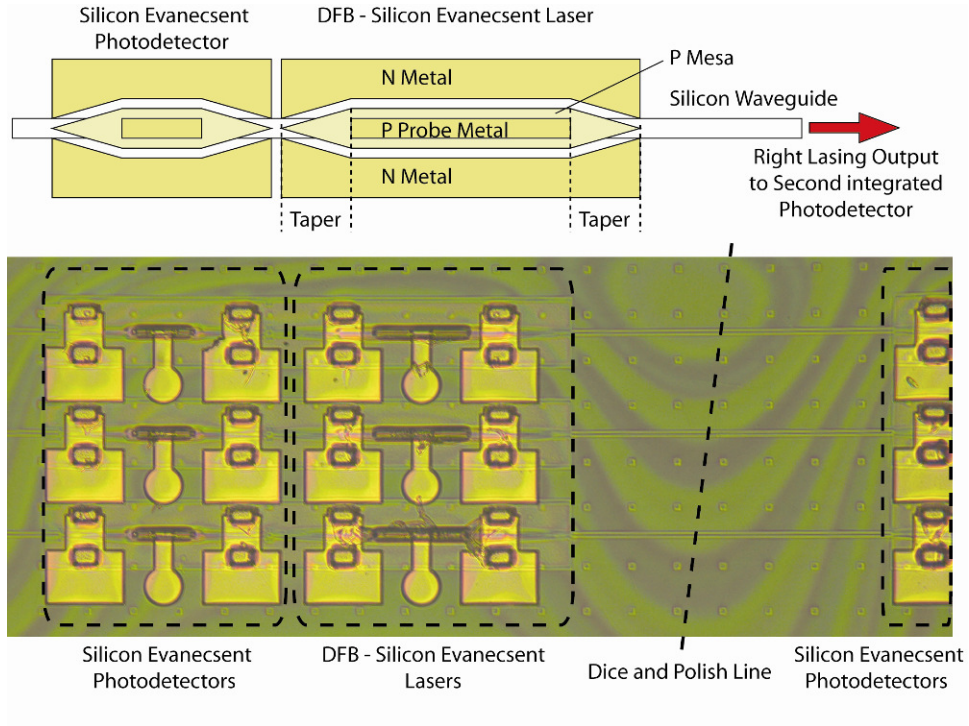


Fig 5-3 – (top) DFB-SEL device layout. (bottom) Microscope image of DFB-SEL and integrated silicon evanescent photo-detectors.

The spontaneous emission spectrum can be used to extract device parameters, such as the effective indices, the group index, the amount of phase shift in the center of the DFB, and  $\kappa$  from the DFB. The spontaneous emission out of one facet can be calculated as follows [10]:

$$(Eq\ 5-3) \quad R_{ASE}(\lambda) = \frac{hc}{\lambda} \frac{\eta_{sp}}{\eta_i} (|S_{11}|^2 + |S_{12}|^2 - 1)$$

where  $h$  is the Planck's constant,  $c$  is the speed of light, and  $\eta_{sp}$  is the population inversion factor.  $S_{11}$  and  $S_{12}$  are the scattering matrix elements of the device and can easily be calculated as a function of wavelength by first using transmission matrices for each element of the DFB, and converting the total transmission matrix to a scattering matrix as described in [11]. There are naturally many parameters that go into the  $S_{11}$  and  $S_{12}$  elements, so it is important to know what values can be determined. The grating period, duty cycle, and length are easily measured via SEM once the device is fabricated.  $\langle\alpha_i\rangle$  and  $\langle g\rangle$  are replaced with a  $\langle g_{effective}\rangle$  term where:

$$(Eq\ 5-4) \quad \langle g_{effective}\rangle = \langle g\rangle - \langle\alpha_i\rangle$$

since they cannot be experimentally decoupled from this particular measurement. The experimental data is then fit with theory by minimizing the error between the two. It is important to understand how the variables change the simulation, in order to get a good fit. In general,  $\kappa$  determines the width of the grating stop-band, the group index determines the periodicity of the features outside the stop-band, the effective index determines the lateral position of the simulated curve,  $\langle g_{effective}\rangle$  determines the amplitude variation, and the phase delay,  $\varphi_{defect}$ , in the quarter wavelength section determines the position of the defect relative to the stop-band.

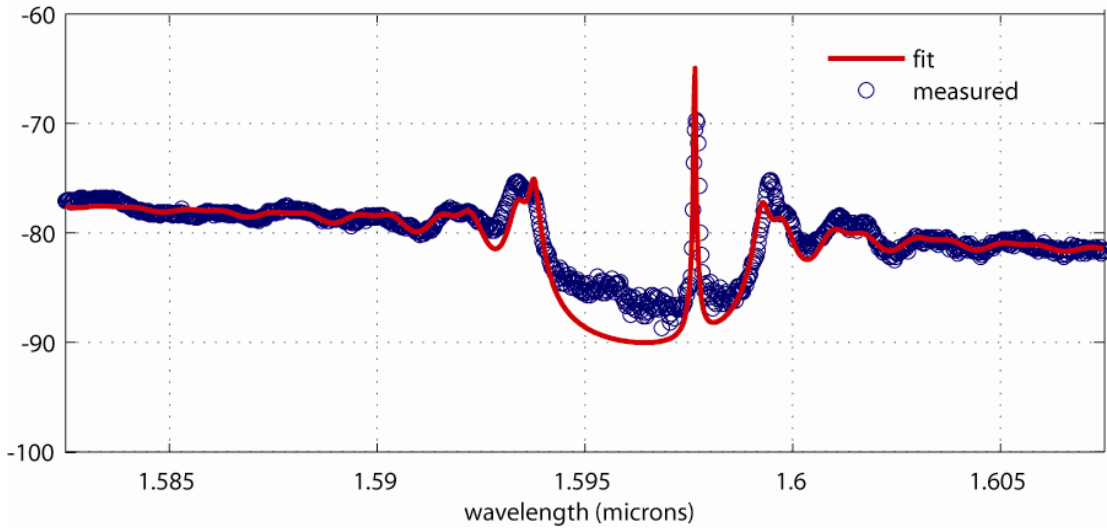


Figure 5-4 – The calculated and measured spontaneous emission spectrum at a 20 mA current injection level and 15 °C stage temperature.

$\langle g_{effective} \rangle$	$\kappa$	$n_{effective}$	$n_{group}$	$\varphi_{defect}$
4	$250 \text{ cm}^{-1}$	3.3504	4	$1.4 * \frac{\lambda}{4}$

Table 5-1 - Extracted device parameters from spontaneous emission simulation shown in Fig. 5-4

Our structure was simplified by assuming that the mesa region maintains its width (with no taper) throughout the length of the device. Even though this simplification neglects the chirp and change of  $\kappa$  in the grating under the taper, and the change in modal gain as the mode is pushed into the silicon under the taper, we still have sufficient agreement between theory and experiment (Figure 5-4) to get a ball park idea of the extracted parameters. The deviation between theory and experiment within the stop band of grating is partially attributed to the noise floor of the

spectrum analyzer. The extracted parameters are shown in Table 5-1. It can be seen that the value of  $\kappa$  is not too far off from the value calculated at the beginning of the chapter. The  $\frac{1}{4}$  wavelength shift is actually larger than originally designed for, since the duty cycle of the grating came out to 70% instead of 50%, resulting in more un-etched region than we intended.

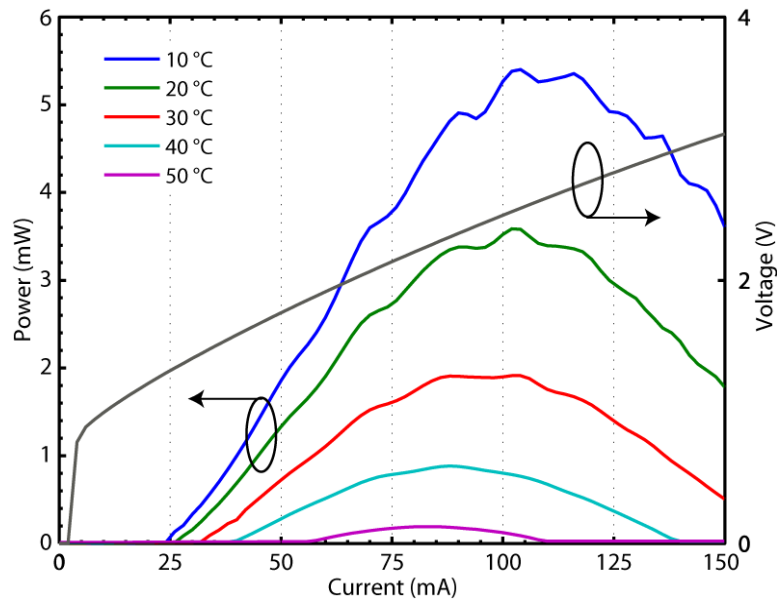


Figure 5-5 – L-I-V curve for stage temperatures of 10 °C to 50 °C.

The light-current (L-I) characteristics of the DFB-SEL are measured on chip by collecting light out of both sides of the laser with integrated silicon evanescent photo-detectors. To determine the laser power output, we assume 100% internal quantum efficiency of the photodetectors in order to conservatively assess the laser performance. It can be seen from Figure 5-5 that at 10 °C, the lasing threshold is 25 mA with a maximum output power of 5.4 mW. The maximum lasing temperature is

50 °C. The secondary y axis of figure 5-5 shows a voltage-current curve. The laser turn on is  $\sim 1.8$  V and the laser has a 13 ohm device series resistance.

The lasing spectrum is taken by dicing off the right photo-detector, polishing, and anti-reflection coating the silicon waveguide output facet. Light is collected with a lensed fiber into an HP spectrum analyzer with a 0.08 nm resolution bandwidth. Figure 5-6 shows the spectrum with a 10 nm span with the laser being driven at 90 mA. The laser has a lasing peak of 1599.3 nm and a side-mode suppression ratio of 50 dB. It can be seen from the inset that the laser operates single mode over a 100 nm span.

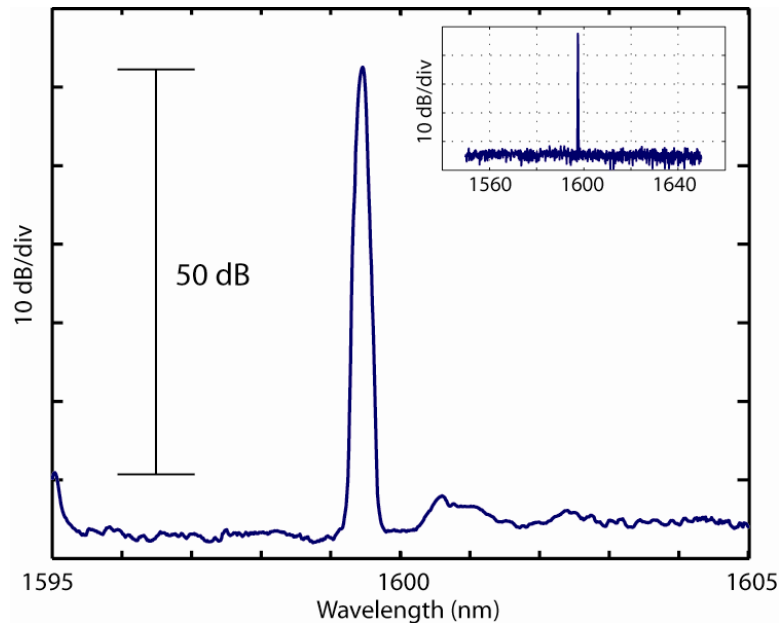


Figure 5-6 - The CW lasing spectrum at 90 mA injection current with a 50 dB side mode extinction ratio. (inset) The CW lasing spectrum over a 100 nm span showing single mode lasing. Both spectra are taken at a 15 °C stage temperature.

The thermal impedance,  $Z_T$ , of the laser was determined by measuring the lasing peak shift as a function of electrical dissipated power (injection current x device voltage) under continuous operation, and as a function of stage temperature under pulsed operation as described in Ref [12]. Figure 5-7a shows the spectral shift under CW operation for various current levels. It can be seen that the laser stays single mode throughout the various current injection levels. Figure 5-7b shows the corresponding plot of wavelength versus electrical dissipated power with a 12.849 nm/W slope ( $d\lambda/dP$ ). Figure 5-7c shows the change in lasing wavelength under pulsed operation as a function a stage temperature.  $d\lambda/dT$  is measured at 0.0971 nm/°C. The resulting thermal impedance is 132 °C/W. This value is higher than the 40 °C/W measured on 850  $\mu\text{m}$  long Fabry-Perot SELs but scales appropriately with the DFB-SEL's short device length of 360  $\mu\text{m}$ .

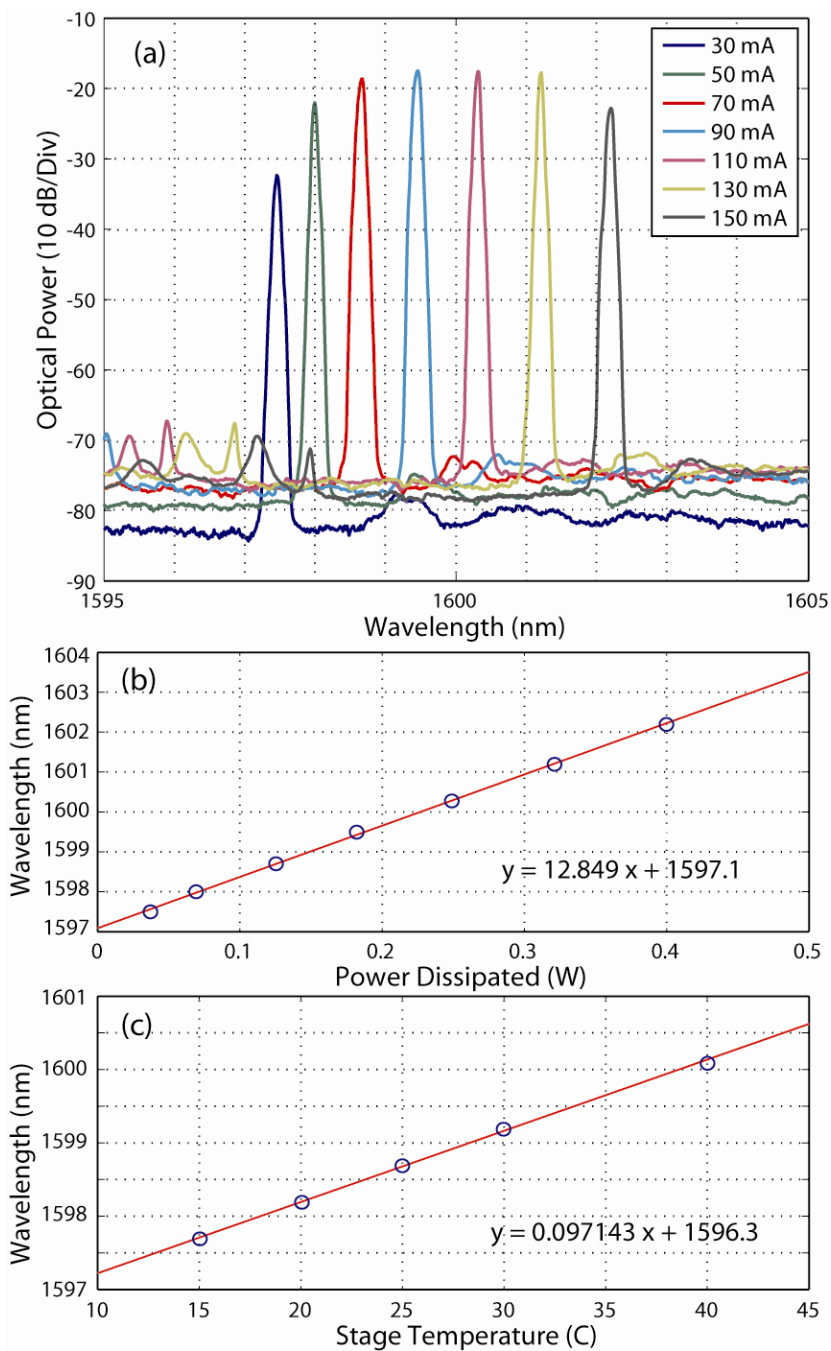


Figure 5-7 (a) Continuous wave lasing spectrum for various current levels. (b) Continuous wave lasing wavelength versus electrical dissipated power. (c) Pulsed lasing wavelength versus stage temperature.



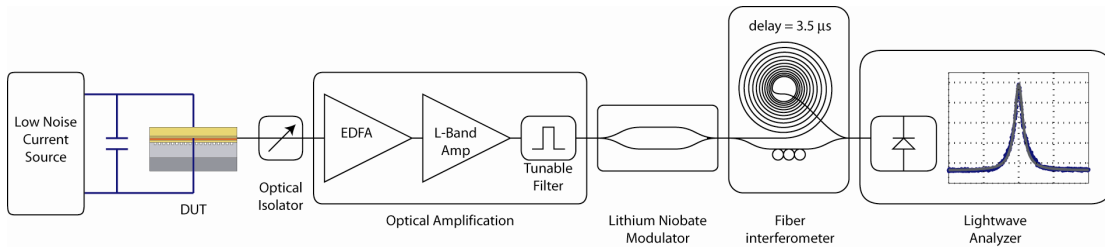
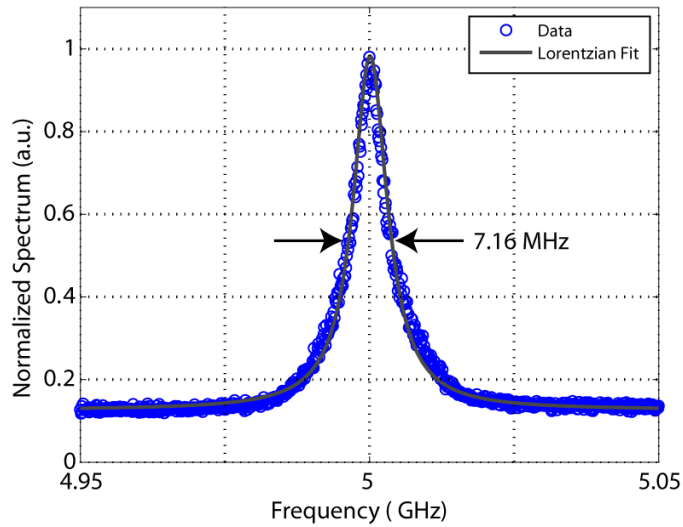


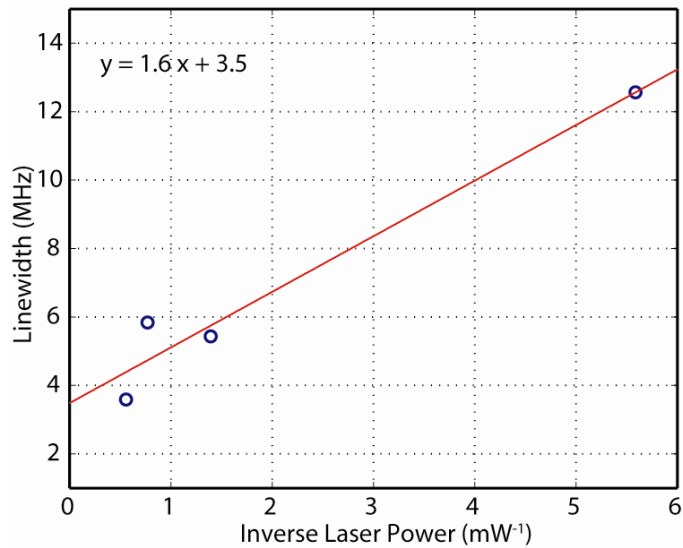
Figure 5-8 – Laser line width measurement experimental set up

The laser line width is measured by using the delayed-self heterodyne method [13] as shown in Figure 5-8. A low noise current source is used to drive the laser in conjunction with a 1000  $\mu\text{F}$  capacitor in parallel to filter out AC variations in the electrical drive since this measurement is very sensitive to the noise and stability of the system. The laser light is collected into a lensed fiber and amplified with a cascaded EDFA and L-band amplifier. Since the output wavelength is out of the EDFA's amplification range, the ASE generated from the EDFA is used as an optical pump for the L-Band amplifier, where the laser signal is amplified. Most of the ASE is filtered out with a 5 nm wide tunable band pass filter. The light is then modulated with a lithium niobate modulator at 5 GHz to generate Lorentzian sidebands 5 GHz away from the laser signal. The signal is passed through a fiber interferometer with a 3.5 microsecond delay. This delay limits the resolution of the line width measurement to 285 KHz since the resolution is the inverse of the time delay. The light is then collected into a photodetector in HP lightwave analyzer. The RF beat signal from the photodetector is measured at 5 GHz on the lightwave analyzer with a 50 KHz resolution bandwidth. Figure 5-9a shows the minimum measured self

heterodyned trace width to be 7.16 MHz corresponding to a 3.6 MHz linewidth, a typical value for commercial DFB lasers. The line width versus inverse output power is shown in figure 5-9b with the expected 1/P slope [14].



(a)



(b)

Figure 5-9 (a) Delayed-self heterodyned line width trace at 1.8 mW laser output power. (b) The laser line width versus the inverse laser output power.

### 5.3 - Summary

We have demonstrated a single wavelength electrically pumped distributed feedback silicon evanescent laser operating at 1600 nm. The laser threshold is 25 mA, and has a maximum output power of 5.4 mW at 10 °C with a maximum lasing temperature of 50 °C. The 50 dB of side mode suppression and 3.6 MHz line width, are comparable to commercial III-V DFB lasers, and can be used in conjunction with high speed silicon modulators and low loss multiplexors to create wavelength division multiplexed transmitters on silicon.

### References

- [1] G. Morthier, P. Vankwikelberge, Handbook of Distributed Feedback Laser Diodes (Arctech House, Norwood, MA, 1997)
  
- [2] Liu, L. Liao, D. Rubin, J. Basak, H. Nguyen, Y. Chetrit, R. Cohen, N. Izhaky, and M. Paniccia, " High-Speed Silicon Modulator for Future VLSI Interconnect," in *Integrated Photonics and Nanophotonics Research and Applications*, OSA Technical Digest (CD) (Optical Society of America, 2007), paper IMD3.
  
- [3] J. Van Campenhout, P. Rojo Romeo, P. Regreny, C. Seassal, D. Van Thourhout, S. Verstuyft, L. Di Cioccio, J. -M. Fedeli, C. Lagahe, and R. Baets, "Electrically pumped InP-based microdisk lasers integrated with a nanophotonic silicon-on-insulator waveguide circuit," *Opt. Express* 15, 6744-6749 (2007)
  
- [4] T. Maruyama, T. Okumura, S. Sakamoto, K. Miura, Y. Nishimoto, and S. Arai, "GaInAsP/InP membrane BH-DFB lasers directly bonded on SOI substrate," *Opt. Express* 14, 8184-8188 (2006)  
<http://www.opticsinfobase.org/abstract.cfm?URI=oe-14-18-8184>

- [5] A. W. Fang, E. Lively, D. Liang, Y.-H. Kuo, J. E. Bowers, "Distributed feedback silicon evanescent laser," Optical fiber communications conference (OFC), Post deadline session PDP15, San Diego CA (2008)
  
- [6] L. A. Coldren and S. W. Corzine, *Diode Lasers and Photonic Integrated Circuits*. New York: John Wiley & Sons, Inc., 1995 pp. 88
  
- [7] L. A. Coldren and S. W. Corzine, *Diode Lasers and Photonic Integrated Circuits*. New York: John Wiley & Sons, Inc., 1995 pp. 266
  
- [8] G. Morthier, P. Vankwikelberge, *Handbook of Distributed Feedback Laser Diodes* (Arctech House, Norwood, MA, 1997)
  
- [9] H. Park, Y.-H. Kuo, A. W. Fang, R. Jones, O. Cohen, M. J. Pannicia, J. E. Bowers, "A hybrid AlGaInAs-silicon evanescent preamplifier and photodetector," *Optics Express*, Vol. 15, No. 21, (2007)
  
- [10] R. Schatz, E. Berglind, and L. Gillner, "Parameter extraction from DFB lasers by means of a simple expression for the spontaneous emission spectrum," *IEEE Photonics Technology Letters*, Vol. 16, No. 10 (1994)
  
- [11] L. A. Coldren and S. W. Corzine, *Diode Lasers and Photonic Integrated Circuits*. New York: John Wiley & Sons, Inc., 1995 pp. 85
  
- [12] M. N. Sysak, H. Park, A. W. Fang, J. E. Bowers, R. Jones, O. Cohen, O. Raday, and M. J. Paniccia, "Experimental and theoretical thermal analysis of a Hybrid Silicon Evanescent Laser," *Opt. Express* **15**, 15041-15046 (2007)
  
- [13] D. Derrickson. *Fiber optic test and measurement* (Prentice Hall,1998), page 185
  
- [14] G. Morthier, P. Vankwikelberge, *Handbook of Distributed Feedback Laser Diodes* (Arctech House, Norwood, MA, 1997)

## Chapter 6 – Summary and Future work

The work presented in this dissertation lays down a foundation for the realization of electrically driven laser sources on silicon that can be manufactured in high volumes at low cost. The key to our approach is the transfer of un-patterned crystalline III-V materials to silicon waveguides through wafer bonding to create devices that utilize both silicon guiding and evanescently coupled III-V gain. This approach differs from the conventional die attach of III-V lasers by moving the  $< 1 \mu\text{m}$  precision alignment steps required during bonding, to post bonding III-V processing, allowing for alignment free bonding. This subtle difference allows for hundreds of lasers to be fabricated in a single bond step. The laser properties are tailored by the silicon waveguide, defining the active region confinement factor and emission properties through the topographic layout and/or the fabrication of silicon gratings. The major achievements of this work include: 1) the design and demonstration of optically pumped hybrid silicon evanescent lasers illustrating that evanescently coupled gain can allow for lasing in waveguides defined in silicon; 2) the first demonstration of electrically pumped Fabry-Perot silicon evanescent lasers along with a second generation of improved lasers; 3) the demonstration of racetrack ring lasers with integrated photodetectors operating in continuous wave and mode locked; and 4) the demonstration of distributed feedback lasers for wavelength division multiplexing applications by patterning gratings in the silicon region prior to bonding.

## *6.1 –Summary*

The first demonstration of a silicon evanescent laser was an optically pumped Fabry Perot laser [1]. The device consisted of a III-V epitaxial layer structure with 5 quantum wells transferred to a silicon waveguide. No patterning was done on the III-V region. When optically pumped through the III-V region above the silicon waveguide, a lasing mode was observed through the output facet. Regions with no silicon waveguide did not lase, showing the influence of the silicon on the lasing properties of the device. In addition, a few waveguide widths were fabricated and the mode profile dependence on waveguide width was observed, showing the ability to tailor the modal properties on silicon processing [2]. The waveguides wider than 1.5  $\mu\text{m}$  showed multiple lateral mode lasing. The 4  $\mu\text{m}$  wide devices operated with an optically pumped threshold of 23 mW with a maximum fiber coupled output of 4.5 mW and lasing up to 60 °C.

Electrically pumped silicon evanescent lasers were developed with the learning from the optically pumped proof of concept lasers. The structure was slightly modified with a reduction of the SCH/Absorber region, since the optical pump was no longer being used. This change and an increase in quantum well number to 8 allowed the increase in silicon confinement factor from  $\sim 40\%$  to  $\sim 65\%$  while still maintaining a 3-5% quantum well confinement factor. Doping was also added to the structure to allow for electrical injection. Initial devices were fabricated without lateral current

confinement, and utilized insulator aperturing beneath contact pads. These devices were used to verify the electrical characteristics and light generation properties of the device. In addition, they showed lasing under pulsed operation, illustrating the need for lateral current confinement to achieve CW operation.

Lateral current confinement was created in the structure by selectively implanting H<sup>+</sup> ions to define a current channel above the waveguides in the p type InP regions. Continuous wave lasing was demonstrated with lasing thresholds of 65 mA, maximum output powers of ~20 mW, and a maximum operating of 40 °C [3]. Heat extraction through the 2 μm thick lower silicon dioxide cladding and the parasitic series resistance from the placement of n contacts 15 μm away from the optical mode was seen as the limiting factor in the device performance. A second generation of devices with a reduced buried oxide thickness of 1 μm and n-contact distance of 8 μm away from the optical mode was demonstrated. Although this generation of devices was designed to have improved thermal impedance, the narrowing of the mesa region simultaneously increased the thermal impedance leading to no net change. The second generation devices had a maximum power output of 28 mW with a maximum lasing temperature of 45 °C; a 5 °C improvement in maximum operating temperature.

Since the optically pumped Fabry-Perot laser and 2 generations of electrically pumped Fabry-Perot lasers all depended on facet polishing to define their cavities,

they are intrinsically discrete and cannot be integrated with other devices. Racetrack lasers were demonstrated in order to illustrate the ability to make on-chip lasers and to show integration with photodetectors[4]. This also demonstrates the flexibility of the silicon evanescent waveguide platform over other hybrid integration approaches. Since we utilize the silicon in the device, we are able to fabricate structures that are more complex and have more functionality than the microdisk and Fabry-Perot lasers demonstrated by III-V membrane devices on silicon. The photodetectors have the identical waveguide structure as the laser and are added to the rings with no additional fabrication steps. The racetrack laser operated continuous wave with a threshold of 175 mA, a maximum output power of 29 mW, and a maximum operating temperature of 60 °C. Mode locked operation was also demonstrated by adding a saturable absorber section inside the cavity with a repetition rate, and pulse width of 30 GHz, and 7 ps, respectively [5]. Both passive and hybrid mode-locking have been achieved with the hybrid mode-locking showing a minimum jitter well within the ITU specification for digital transmission of 364 fs for 30 GHz data rates.

The final device demonstration presented in this work is the distributed feedback silicon evanescent laser[6]. Single wavelength lasers are one of the fundamental components in wavelength division multiplexed optical systems. The gratings for this device were fabricated in the silicon waveguide prior to bonding, reinforcing the fact that the silicon processing defines the laser cavity and performance. Current III-V



DFB gratings are fabricated by utilizing holographic lithography since projection lithography machines in III-V fabrication facilities do not have the resolution to make ~240 nm pitch gratings. Since these gratings have the same period across the wafer, they need to use techniques such as wave guide width variations in order to have an array of multiple wavelengths on a single die. Although this demonstration utilized e-beam lithography in a university cleanroom, it can be directly translated to a CMOS fabrication facility. State of the art CMOS lithography has a minimum feature size of 50 nm, allowing for the fabrication of gratings on silicon with excellent uniformity across the wafer, high repeatability, and the ability to lithographically implement quarter wavelength shifts inside the cavity. The DFB SELs lased with a maximum output power, threshold current and maximum operating temperature of 5.4 mW, 25 mA, and 50 °C, respectively.

## *6.2 - Future Directions*

Continued research in silicon evanescent lasers can be divided in the following areas:

1) optimization of the waveguide structure to improve laser performance in the area of minimizing drive current while still maintaining output levels in the 10s of mW range, extending the maximum operating temperature, 2) the development of ways to achieve multiple band gaps structures to create more complex lasers with tunable phase sections or cascaded electro absorption modulators, and 3) exploring the new hybrid design space of low loss silicon waveguides with high gain III-Vs to create

integrated devices that do not currently exist on a purely III-V or purely silicon platform to date.

The devices presented in this dissertation utilized relatively low confinement factors in the quantum well region ( $\sim 3 - 5 \%$ ) in order to still allow for high confinements over the silicon waveguide. Laser thresholds can be reduced by increasing the quantum well confinement to 10% and greater while still achieving high coupling efficiency to passive silicon waveguides using taper structures in the III-V and silicon regions. This in conjunction with reductions in cavity lengths and improvements in injection efficiency can further reduce these thresholds to achieve thresholds on the order of 1-10 mA. In Chapter 3, we showed that the injection efficiency for continuous wave operation was 51%. This is primarily limited by pumping active regions that have no overlap with the optical mode. By optimizing carrier profile in the active region overlap with the optical mode profile, the efficiency could be substantially increased to values greater than 85%. This can be done by first reducing the width of the proton implant defined current channel in p mesa from the current 4  $\mu\text{m}$  value to channel widths between 0.5 to 1.5  $\mu\text{m}$ . In addition, the depth of the proton implant profile can be optimized to minimize the amount of current profile spreading before the carriers flow into the quantum wells. Alternatively, other current lateral confinement schemes can be implemented without the use of proton implant. Figure 6-1a illustrates a scheme where the p-mesa region is etched close to the SCH region to provide a similar channeling effect.

This structure would have to be carefully designed as the mode profile would change with this etch. The lateral heat extraction would also be reduced but could be overcome with the proper contact and top heat sink design. Figure 6-1b shows a current confinement structure utilizing a selective etches of the SCH region to create a current aperture. Similar aperture structures have been demonstrated in VCSELs [7]. The mechanical strength of this structure may be weakened by this under etch, but can be reinforced with oxides or polymers. Alternatively, selective oxidation of the SCH can also provide the same type of current aperture without adding mechanical instability, as shown in Figure 6-1c.

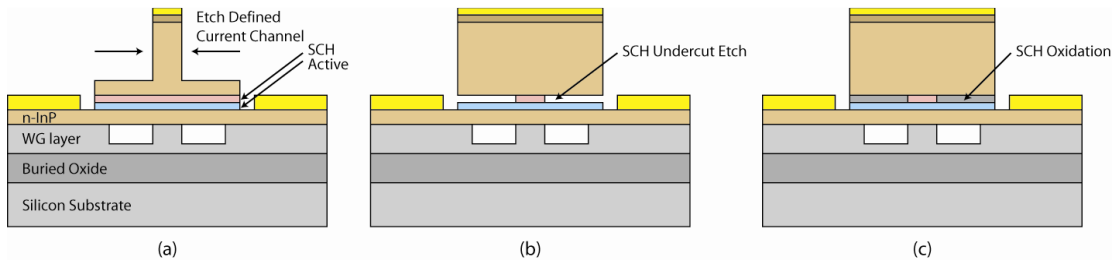


Figure 6-1: Alternative lateral current confinement structures through (a) mesa definition, (b) a SCH undercut aperture, and (c) a SCH oxidation aperture.

The epitaxial layer structure can also be modified to increase the injection efficiency. Figure 6-2 shows the band structure of our device with the addition of an electron blocking layer. In Chapter 3, we described the carrier flow through this structure with holes injected from the left of the diagram (p mesa side), and electrons injected from the right side. Electrons that escape from the quantum wells, can flow into the SCH reducing the overall injection efficiency. The addition of an extra layer, an

electron blocking layer, between the SCH and the quantum wells with a high conduction band offset and low valence band offset would be useful such that holes could still flow into the quantum wells, while keeping electrons inside the quantum wells [8]. The removal of an SCH all together can remove the need for an electron blocking layer. The waveguide height would need to be reduced in order to maintain the 3-5% quantum well confinement factor for this epitaxial layer structure to ~500 nm. As an added benefit, the silicon confinement factor would increase to 70% leading to a reduction in minimum bend radius due to the reduction of slab modes in the III-V mesa and improved coupling to passive silicon waveguides.

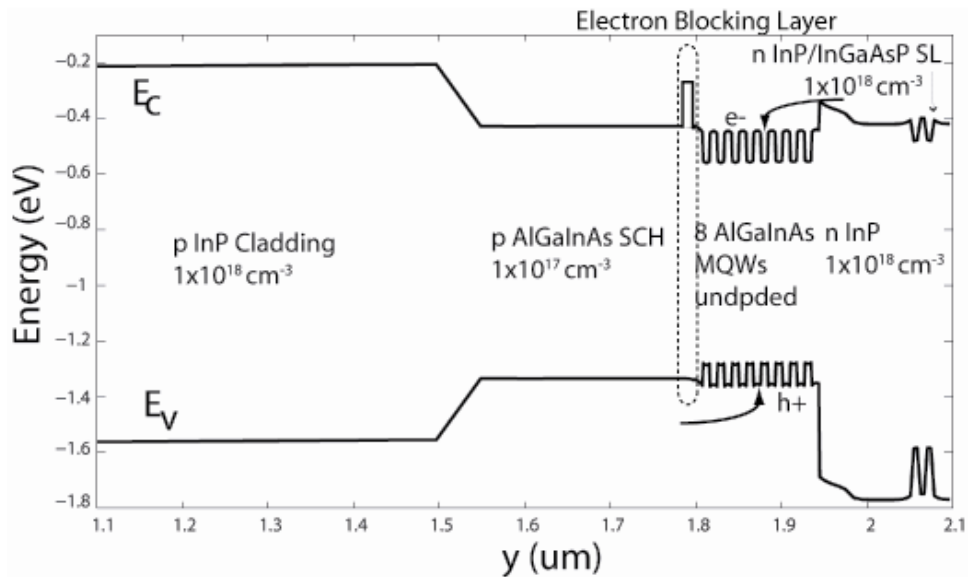


Figure 6-2: Device band diagram with the addition of an electron blocking layer.

The thermal analysis presented in Chapter 3, indicates that the thermal performance of silicon evanescent lasers is currently limited by heat extraction from the active region, due to presence of the silicon dioxide lower cladding. Since transverse heat

flow directly down the device is limited by the oxide thickness, lateral heat flow becomes an important mode of heat extraction. Thermal shunts can be created on the sides of the device by etching through the silicon waveguide layer and the lower cladding layer and filling the void with materials with higher thermal conductivity such as metal or polycrystalline silicon. Thick metals from the p-mesa or n-layer of the device are used to thermally connect the device to the substrate. The lateral heat flow from the active region to the substrate for these various shunt configurations are shown in Figure 6-3. The use of thermal shunts should substantially reduce the thermal impedance of the device, extending the maximum operating temperature of silicon evanescent lasers.

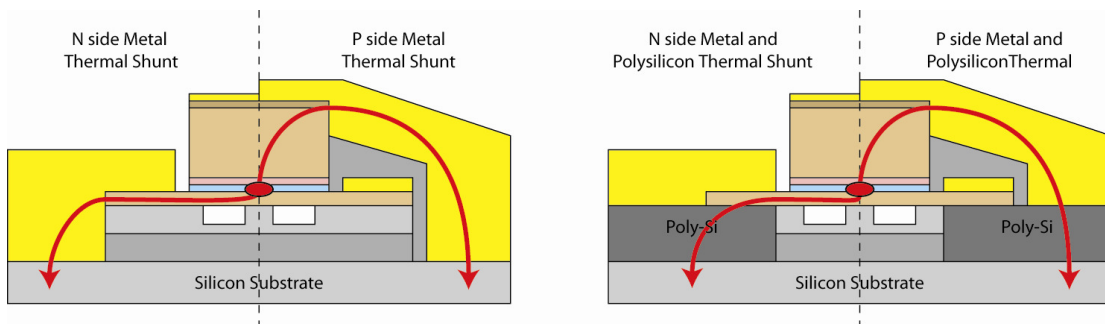


Figure 6-3: Metal thermal shunts and poly silicon thermal shunts. The path of heat transfer from the active region to the substrate are denoted with red arrows.

Wafer bonding III-V structures onto silicon can be viewed as being equivalent to a photonic integrated circuit on III-Vs utilizing a single re-growth to create 2 bandgap regions: large band gap transparent passive regions and small band gap light emitting active regions. Many advanced photonic integrated circuits, such as wavelength converters and integrated electro absorption modulator (EAM) sampled

grating (SG) DBR lasers, utilize three band-gap regions; large band gap transparent passive regions, small band gap light emitting active regions, and mid band gap electro-absorption or phase shifting regions. Although phase shifting regions can be achieved through carrier injection in silicon waveguide regions, it is desirable to realize a second III-V epitaxial layer transfer to the silicon waveguides. The introduction of a second III-V epitaxial layer can be done by either selectively changing the quantum well states across the wafer through quantum well intermixing [9], or by conducting non-planar wafer bonding techniques [10].

Finally, the unique characteristics of the silicon evanescent platform provides a design space where low loss silicon waveguides and high gain III-V materials can be used together and should be explored in order to realize devices that could not exist in each material system alone. For example, integrated mode locked lasers with passive regions and active regions have a maximum cavity size due to round trip losses associated with the loss of the passive region. Since the loss of silicon passive waveguides are much lower than their InP based counterparts, ultra long cavities (~ meters) can be realized to produce integrated mode-locked lasers with repetition rates that are shorter than anything ever reported (~ 100 MHz and lower).

Although there is still much research and development to be done in the area of silicon evanescent lasers, the work presented in this dissertation serves as an important step towards achieving photonic integration on silicon by not only

providing a manufacturable way to integrate compound semiconductors in silicon to create hybrid lasers, but also by developing a few types of lasers with characteristics that can be used in a large range of applications.

### *References*

- [1] H. Park, A. W. Fang, S. Kodama, and J. E. Bowers, "Hybrid silicon evanescent laser fabricated with a silicon waveguide and III-V offset quantum wells," *Optics Express*, 13, 9460-9464, (2005)
- [2] A. W. Fang, H. Park, R. Jones, O. Cohen, M. J. Paniccia, J. E. Bowers, "A Continuous-Wave Hybrid AlGaInAs–Silicon Evanescent Laser," *IEEE Photonics Technology Letters*, Vol. 18, Issue 10, pg 1143 – 1145 (2006)
- [3] A. W. Fang, H. Park, O. Cohen, R. Jones, M. J. Paniccia, and J. E. Bowers, "Electrically pumped hybrid AlGaInAs-silicon evanescent laser," *Optics Express*, 14, 9203-9210, (2006)
- [4] A. W. Fang, R. Jones, H. Park, O. Cohen, O. Rada, M. J. Paniccia, and J. E. Bowers, "Integrated AlGaInAs-silicon evanescent racetrack lasers and photodetector," *Optics Express*, Vol. 15, Issue 5, pp. 2315-2322, 2007
- [5] B. R. Koch, A. W. Fang, O. Cohen, and J. E. Bowers, " Mode -locked silicon evanescent lasers," *Opt. Express* 15, 11225-11233 (2007).
- [6] A. W. Fang, E. Lively, D. Liang, Y.-H. Kuo, J. E. Bowers, "Distributed feedback silicon evanescent laser," *Optical fiber communications conference (OFC), Post deadline session PDP15, San Diego CA* (2008)
- [7] M.H.M. Reddy, T. Asano, D. Feezell, D.A. Buell, A.S. Huntington, R. Koda, and L.A. Coldren, "Selectively Etched Tunnel Junction for Lateral Current and Optical Confinement in InP-Based Vertical Cavity Lasers," *Jour. of Elec. Mat.*, vol. 33, no. 2, pp. 118-122, 2004.

- [8] Y.-A. Chang, T.-S. Ko, J.-R. Chen, F.-I. Lai, C.-L. Yu, I.-T. Wu, H.-C. Kuo, Y.-K. Kuo, L.-W. Lai, L.-H. Lai, T.-C. Lu, and S.-C. Wang, "The carrier blocking effect on 850 nm InAlGaAs/AlGaAs vertical-cavity surface-emitting lasers," *Semicond. Sci. Technol.* 21, 1488-1494 (2006).
  
- [9] E. Skogen, *Quantum well intermixing for wavelength-agile photonic integrated circuits*, Ph.D Dissertation, University of California Santa Barbara, 2003
  
- [10] J. Geske, D. Leonard, M. MacDougal, J. E. Bowers, "CWDM Vertical-Cavity Surface Emitting Laser Array Spanning 140 Nm Of The C, S, and L, Fiber Transmission Bands," 29th Optical Fiber Communications Conference (OFC'04), paper TuE7, Los Angeles, CA, FEBRUARY 2004



# Appendix A –

## A.1 - Electrically Pumped SEL Process Follower

- 1 Plasma Assisted Bonding and InP Substrate Removal**
  - 1.1 Use 8mm squares  
SOI size -  
III-V active epi size -
  - 1.2 Rinse both pieces in ACE/ISO/DI (2X/1X/1x)  
SOI in ultrasonic. III-V in gentle rinse
  - 1.3 Swab both pieces in Tergitol using 20 strokes in each direction
  - 1.4 Rinse both pieces in DI
  - 1.5 Inspect and repeat 1.3-5 until no surface particles are present
  - 1.6 Descum - place both samples in PECVD descum for 1 minute at 100W/0.3torr
  - 1.7 Silicon native oxide removal - Place SOI samples in Buffered HF  
Dip time: \_\_\_\_\_ Rate~ 100nm/min
  - 1.8 III-V (InGaAs) cap layer removal -  
H2O:H2O2:H3PO4 (38:1:1)  
Etch time: 5 min \_\_\_\_\_  
rate ~ .1 um/min
  - 1.9 Rinse III-V in DI
  - 1.10 III-V Surface treatment (oxide removal) in NH4OH  
Dip time: 1 min \_\_\_\_\_
  - 1.11 Rinse III-V in DI
  - 1.12 Rinse SOI in DI
  - 1.13 Inspect and clean in tergitol/DI until no surface particles are present
  - 1.13a Ozone Treatment for 15 minutes
  - 1.14 O2 Precoat RIE 5 chamber  
O2: sccm \_\_\_\_\_ 50 sccm 55 mT  
RF power: \_\_\_\_\_ 300W  
Time: 10 min \_\_\_\_\_
  - 1.15 O2 Plasma treat SOI and III-V surfaces in RIE 5  
O2: sccm \_\_\_\_\_ 26 sccm 15mT  
RF: power \_\_\_\_\_ 39W  
Time: sec \_\_\_\_\_ 45s
  - 1.16 Dip both pieces in DI
  - 1.17 Dry both pieces with N2 and perform physical bond
  - 1.18 Perform strong bond  
Bond pressure: \_\_\_\_\_  
Bond temperature: 300C \_\_\_\_\_  
Bond time: 12 hr \_\_\_\_\_
  - 1.19 Mount Bonded sample on SI carrier with crystal bond

1.20 Place in HCL:H2O (3:1) until bubbling stops (~ 1 to 1.5 hour), keep an eye on the sample after 50min

Etch time:

**2 SiN Hard Mask deposition for thin mesa etch**

2.1 DI Rinse & Dehydration Bake (115C 2 min)

Rinse time: 2 min \_\_\_\_\_

2.2 PECVD Nitride deposition

Chamber clean (w/o sample): 30 min \_\_\_\_\_

Nitride thickness: 1500 A \_\_\_\_\_

2.3 DI Rinse & Dehydration Bake (115C 2 min)

Rinse time: 2 min \_\_\_\_\_

2.4 PECVD Nitride deposition

Nitride thickness: 1500 A \_\_\_\_\_

**3 PATTERN SiN FOR MESA ETCH**

3.1 Acetone/Iso/N2 Clean, O2 descum 30 seconds

3.2 Bake/Spin HMDS

2min \_\_\_\_\_ 110C \_\_\_\_\_

1 min \_\_\_\_\_ 5K rpm

3.3 Spin/Bake 4330 (positive)

Spin speed: 5K \_\_\_\_\_

Spin time 1 min

Bake Temp: 95C \_\_\_\_\_

Bake time: 1 min

3.4 Edge bead removal

Razor blade method, Or edge bead removal pattern

If pattern, use 90 seconds expose time & develop in

AZ400:Di 1:4

3.5 Align '16 micron mesa' pattern from 'Epump2' mask set AZ400K:DI 1:4

Expose time for old SUSS contact aligner: 25" \_\_\_\_\_

OR Expose time for new MA6 SUSS: 17" \_\_\_\_\_

Develop time: 1' \_\_\_\_\_

3.6 O2 descum 300 mT/100W

Descum time: 20" \_\_\_\_\_

3.7 Dektak resist height

Resist height: \_\_\_\_\_

3.8 CF4 etch 300mT/100W

Etch time: 4 min. \_\_\_\_\_ (SiN etchrate is ~ 750 A/min)

3.9 O2 descum 300 mT/100W

Descum time: 20" \_\_\_\_\_

3.10 Strip PR in 80C 1165, heat 1165 BEFORE placing sample in container (~10min)

3.11 Rinse in ISO/Di

**4 RIE2 ETCH FOR MESA to quaternary region**

4.1 O2 Chamber clean (w/o sample)

O2: 20 sccm \_\_\_\_\_

Pressure: 125 mT \_\_\_\_\_

- Voltage: 500 V \_\_\_\_\_
- Time: 30' \_\_\_\_\_
- 4.2 MHA Precoat (w/o sample)
  - CH4: 4 sccm \_\_\_\_\_
  - H: 20 sccm \_\_\_\_\_
  - Ar: 10 sccm \_\_\_\_\_
  - Pressure: 75 mT \_\_\_\_\_
  - Voltage: 500 V \_\_\_\_\_
  - Time: 20' \_\_\_\_\_
- 4.3 Load sample
- 4.4 MHA Etch
  - CH4: 4 sccm \_\_\_\_\_
  - H: 20 sccm \_\_\_\_\_
  - Ar: 10 sccm \_\_\_\_\_
  - Pressure: 75 mT \_\_\_\_\_
  - Voltage: 500 V \_\_\_\_\_
  - Time: check log book \_\_\_\_\_
  - Monitor with Laser
- 4.5 O2 Sample clean
  - O2: 20 sccm \_\_\_\_\_
  - Voltage: 300 V \_\_\_\_\_
  - Time: 11' \_\_\_\_\_
- 4.6 Dektak etch depth
  - Depth: ~19000 A (including SiN) \_\_\_\_\_

## 5 WET ETCH FOR MESA/BOTTOM N-METAL

- 5.1 Remove AllnGaAs active layer
  - AllnAs/AllnGaAs etch time (1:5:15 H3PO4:H2O2:H2O):
  - 1 min \_\_\_\_\_ (look for color change)
- 5.2 Dektak etch depth
  - Depth: ~22960 A (including SiN) \_\_\_\_\_

## 6 BOTTOM N-METAL DEFINITION

- 6.1 Sample Solvent Clean: Ace (2min), methanol (1min), O2 descum 30 seconds
- 6.2 Sample Dehydration bake:
  - 110C \_\_\_\_\_
  - 1 min \_\_\_\_\_
- 6.3 Spin on SF-11 Resist (~1.5um)
  - Use blue tape, lots of sf11, and very fast ramp rate ~ 6000rpm/s
  - 4000rpm \_\_\_\_\_
  - 30seconds \_\_\_\_\_
- 6.4 Pre-Exposure-Bake:
  - 200C
  - 1 min \_\_\_\_\_
- 6.5 Spin on SF-11 Resist (~1.5um)

- Use blue tape, lots of sf11, and very fast ramp rate ~ 6000rpm/s  
 4000rpm \_\_\_\_\_  
 30seconds \_\_\_\_\_
- 6.6 Pre-Exposure-Bake:  
 200C  
 2 min \_\_\_\_\_ Let cool before next step
- 6.7 Spin on AZ5214 Resist (negative)  
 4000rpm \_\_\_\_\_  
 30seconds \_\_\_\_\_
- 6.8 Pre-Exposure-Bake:  
 95C \_\_\_\_\_  
 2 min \_\_\_\_\_
- 6.9 Edge bead removal  
 Razor blade method, Or edge bead removal pattern  
 If pattern, use 90 seconds expose time & develop in AZ400:Di 1:
- 6.10 Expose with 'N metal' mask  
 Expose time for old SUSS: 9" \_\_\_\_\_  
 Expose time for new MA6 SUSS: 7" \_\_\_\_\_
- 6.11 Post-Exposure-Bake:  
 110C \_\_\_\_\_  
 1 min \_\_\_\_\_
- 6.12 Flood expose  
 1 min \_\_\_\_\_
- 6.13 Develop the Resist: using diluted AZ-400K developer (dilution ratio of 1:4)  
 40 seconds \_\_\_\_\_
- 6.14 Post- Development Bake  
 110C \_\_\_\_\_  
 1 min \_\_\_\_\_
- 6.15 1st Deep UV expose SF-11 Resist:  
 1000W  
 300 seconds \_\_\_\_\_
- 6.16 Develop SF-11 Resist: SAL101 Developer  
 70 seconds \_\_\_\_\_
- 6.17 2nd Deep UV expose SF-11 Resist:  
 1000W  
 300 seconds \_\_\_\_\_
- 6.18 Develop SF-11 Resist: SAL101 Developer  
 70 seconds \_\_\_\_\_
- 6.19 3rd Deep UV expose SF-11 Resist:  
 1000W  
 300 seconds \_\_\_\_\_
- 6.20 Develop SF-11 Resist: SAL101 Developer  
 60 seconds \_\_\_\_\_
- 6.21 O2 plasma resist residue descum

- 300 mT \_\_\_\_\_  
 100 W \_\_\_\_\_  
 30s \_\_\_\_\_
- 6.22 Remove surface oxide:  
 Rinse in HF:H2O (1:10) 30 sec \_\_\_\_\_  
 Rinse in H2O 1 min \_\_\_\_\_
- 6.23 Load into e-beam 3 and deposit Ni;Ge;Au;Ni;Au  
 (50A;200A;200A;200A;10000A)  
 Ni: \_\_\_\_\_  
 Ge: \_\_\_\_\_  
 Au: \_\_\_\_\_  
 Ni: \_\_\_\_\_  
 Au: \_\_\_\_\_
- 6.24 Lift off in 1165 80C. Rinse in ISO.  
 O2 descum in necessary to remove resist residue

## 7 Nitride Removal

- 7.1 Rinse in ACE/ISO/Di  
 7.2 O2 descum at 300mT/100W  
 Descum time: 1" \_\_\_\_\_  
 7.3 CF4 etch 300mT/100W  
 Etch time: 4 min. \_\_\_\_\_

## 8 Thin mesa P metal deposition

- 8.1 Sample Solvent Clean: Ace (2min), methanol (1min), Di, O2 descum 30 sec  
 8.2 Sample Dehydration bake:  
 110C \_\_\_\_\_  
 1 min \_\_\_\_\_
- 8.3 Spin on SF-11 Resist (~1.5um)  
 Use blue tape, lots of sf11, and very fast ramp rate ~ 6000rpm/s  
 4000rpm \_\_\_\_\_  
 30seconds \_\_\_\_\_
- 8.4 Pre-Exposure-Bake:  
 200C  
 1 min \_\_\_\_\_
- 8.5 Spin on SF-11 Resist (~1.5um)  
 Use blue tape, lots of sf11, and very fast ramp rate ~ 6000rpm/s  
 4000rpm \_\_\_\_\_  
 30seconds \_\_\_\_\_
- 8.6 Pre-Exposure-Bake:  
 200C  
 2 min \_\_\_\_\_
- 8.7 Spin on AZ5214 Resist (negative)  
 4000rpm \_\_\_\_\_  
 30seconds \_\_\_\_\_
- 8.8 Pre-Exposure-Bake:

- 95C \_\_\_\_\_  
2 min \_\_\_\_\_
- 8.9 Edge bead removal  
Razor blade method, Or edge bead removal pattern  
If pattern, use 90 seconds expose time & develop in AZ400:Di 1:4
- 8.10 Expose with 'p metal mask'  
Expose time for old SUSS: 9" \_\_\_\_\_  
Expose time for new MA6 SUSS: 7" \_\_\_\_\_
- 8.11 Post-Exposure-Bake:  
110C \_\_\_\_\_  
1 min \_\_\_\_\_
- 8.12 Flood expose  
1 min \_\_\_\_\_
- 8.13 Develop the Resist: using diluted AZ-400K developer (dilution ratio of 1:4)  
40 seconds \_\_\_\_\_
- 8.14 Post- Development Bake  
110C \_\_\_\_\_  
1 min \_\_\_\_\_
- 8.15 1st Deep UV expose SF-11 Resist:  
1000W  
300 seconds \_\_\_\_\_
- 8.16 Develop SF-11 Resist: SAL101 Developer  
70 seconds \_\_\_\_\_
- 8.17 2nd Deep UV expose SF-11 Resist:  
1000W  
300 seconds \_\_\_\_\_
- 8.18 Develop SF-11 Resist: SAL101 Developer  
70 seconds \_\_\_\_\_
- 8.19 2nd Deep UV expose SF-11 Resist:  
1000W  
300 seconds \_\_\_\_\_
- 8.20 Develop SF-11 Resist: SAL101 Developer  
60 seconds \_\_\_\_\_
- 8.21 O2 plasma resist residue descum  
300 mT \_\_\_\_\_  
100 W \_\_\_\_\_  
30 s \_\_\_\_\_
- 8.22 Remove surface oxide:  
Rinse in HF:H2O (1:10) 30 sec \_\_\_\_\_  
Rinse in H2O 1 min \_\_\_\_\_
- 8.23 Load into e-beam 3 and deposit Pd;Ti;Pd:Au(30A;170A;170A;15000A)  
Pd: \_\_\_\_\_  
Ti: \_\_\_\_\_  
Pd: \_\_\_\_\_  
Au: \_\_\_\_\_

- 8.20 Lift off in 1165 80C. Rinse in ISO/Di.  
O2 descum in necessary to remove resist residue
- 8.21 Strip Anneal
  - Open Forming Gas (behind HF bench)
  - load sample
  - pump down to 1mTorr - adjust gas flow
  - set temperature to 320C Make sure this is the correct temp based on optimisation.
  - Anneal for 30 sec
  - Once it starts set the temperature to 0
  - Do not release until 20 sec into annealing

**9 SiN Hard Mask deposition for proton implant surface protection**

- 9.1 DI Rinse & Dehydration Bake (115C 2 min)  
Rinse time: 2 min \_\_\_\_\_
- 9.2 PECVD Nitride deposition  
Chamber clean (w/o sample): 30 min \_\_\_\_\_  
Nitride thickness: 1500 A \_\_\_\_\_
- 9.3 DI Rinse & Dehydration Bake (115C 2 min)  
Rinse time: 2 min \_\_\_\_\_
- 9.4 PECVD Nitride deposition  
Nitride thickness: 1500 A \_\_\_\_\_

**10 Proton implantation Mask**

- 10.1 Sample Solvent Clean:
  - Ace (2min), methanol (1min), Di, O2 descum 30 sec
- 10.2 Sample Dehydration bake:
  - 110C \_\_\_\_\_
  - 1 min \_\_\_\_\_
- 10.3 Spin/bake SF11 - remove edge bead w/ razor blade
  - Use blue tape, lots of sf11, and
  - very fast ramp rate ~ 6000rpm/s
  - Spin speed: 4K \_\_\_\_\_
  - Spin time: 30" \_\_\_\_\_
  - Bake temperature: 200C \_\_\_\_\_
  - Bake time: 1' \_\_\_\_\_
- 10.4 Spin/bake SF11 - remove edge bead w/ razor blade
  - Use blue tape, lots of sf11, and
  - very fast ramp rate ~ 6000rpm/s
  - Spin speed: 4K \_\_\_\_\_
  - Spin time: 30" \_\_\_\_\_
  - Bake temperature: 200C \_\_\_\_\_
  - Bake time: 1' \_\_\_\_\_
- 10.5 Spin/bake SF11 - remove edge bead w/ razor blade
  - Use blue tape, lots of sf11, and

- very fast ramp rate ~ 6000rpm/s
- Spin speed: 4K \_\_\_\_\_
- Spin time: 30" \_\_\_\_\_
- Bake temperature: 200C \_\_\_\_\_
- Bake time: 2' \_\_\_\_\_
- 10.6 Spin on AZ5214 Resist (negative)
- 4000rpm \_\_\_\_\_
- 30seconds \_\_\_\_\_
- 10.7 Pre-Exposure-Bake:
- 95C \_\_\_\_\_
- 2 min \_\_\_\_\_
- 10.8 Edge bead removal
- Razor blade method, Or edge bead removal pattern
- If pattern, use 90 seconds expose time & develop in
- AZ400:Di 1:4
- 10.9 Expose 'p mesa' (same mask as the first litho, but negative resist)
- 9 seconds \_\_\_\_\_
- 10.10 Post-Exposure-Bake:
- 110C \_\_\_\_\_
- 1 min \_\_\_\_\_
- 10.11 Flood expose
- 1 min \_\_\_\_\_
- 10.12 Develop the Resist: using diluted AZ-400K developer
- (dilution ratio of 1:4)
- 40 seconds \_\_\_\_\_
- 10.13 Post- Development Bake
- 110C \_\_\_\_\_
- 1 min \_\_\_\_\_
- 10.14 O2 descum at 300mT/100W
- Descum time: 10" \_\_\_\_\_
- 10.15 Deep UV expose
- Expose time: 300" (with spin) \_\_\_\_\_
- 10.16 Develop in SAL101 and DI rinse
- Develop time: 70" \_\_\_\_\_
- 10.17 Deep UV expose (2nd time)
- Expose time: 300" (with spin) \_\_\_\_\_
- 10.18 Develop in SAL101 and DI rinse
- Develop time: 70" \_\_\_\_\_
- 10.19 Deep UV expose (3rd time)
- Expose time: 300" (with spin) \_\_\_\_\_
- 10.20 Develop in SAL101 and DI rinse
- Develop time: 70" \_\_\_\_\_
- 10.21 Deep UV expose (4th time)
- Expose time: 300" (with spin) \_\_\_\_\_
- 10.22 Develop in SAL101 and DI rinse



- Develop time: 60" \_\_\_\_\_
- 10.23 Send out to KROKO for implantation
- 11 Strip Proton resist and SiN Hard Mask deposition for p metal isolation**
- 11.1 PR removal in 1165 80C. Rinse in ISO/Di.  
O2 descum in necessary to remove resist residue
- 11.2 DI Rinse & Dehydration Bake (115C 2 min)
- Rinse time: 2 min \_\_\_\_\_
- 11.3 PECVD Nitride deposition  
Chamber clean (w/o sample): 30 min \_\_\_\_\_
- Nitride thickness: 1500 A \_\_\_\_\_
- 12 SiN P metal isolation layer patterning**
- 12.1 Sample Solvent Clean: Ace (2min), methanol (1min)
- 12.2 DI Rinse  
Rinse time: 2 min \_\_\_\_\_
- 12.3 O2 Descum 30 seconds
- 12.4 Dehydration bake 110 C 2 min
- 12.5 Spin/Bake 4330 (positive)  
Spin speed: 5K \_\_\_\_\_  
Bake time: 1 min \_\_\_\_\_
- 12.6 Edge bead removal  
Razor blade method, Or edge bead removal pattern  
If pattern, use 90 seconds expose time & develop in AZ400:Di 1:4
- 12.7 Align 'SiO2' pattern from mask  
Expose time for old SUSS contact aligner: 25" \_\_\_\_\_  
OR Expose time for new MA6 SUSS: 17" \_\_\_\_\_  
Develop 1 min AZ 400: 1:4
- 12.8 O2 descum 300 mT/100W  
Descum time: 20" \_\_\_\_\_
- 12.9 Dektak resist height  
Resist height: \_\_\_\_\_
- 12.10 CF4 etch  
Etch time: 6 min. \_\_\_\_\_
- 12.11 O2 descum 300 mT/100W  
Descum time: 20" \_\_\_\_\_
- 12.12 Strip PR in 80C 1165
- 12.13 Rinse in Iso/Di
- 13 P probe pad metal deposition**
- 13.1 Rinse in ACE/ISO/Di
- 13.2 O2 descum at 300mT/100W  
Descum time: 30 Sec \_\_\_\_\_
- 13.3 Sample Dehydration bake:

- 200C \_\_\_\_\_  
1 min \_\_\_\_\_
- 13.4 Spin/bake SF11 - remove edge bead w/ razor blade  
Use blue tape, lots of sf11, and very fast ramp rate ~ 6000rpm/s  
Spin speed: 4K \_\_\_\_\_  
Spin time: 30" \_\_\_\_\_  
Bake temperature: 200C \_\_\_\_\_  
Bake time: 1' \_\_\_\_\_
- 13.5 Spin/bake SF11 - remove edge bead w/ razor blade  
Use blue tape, lots of sf11, and very fast ramp rate ~ 6000rpm/s  
Spin speed: 4K \_\_\_\_\_  
Spin time: 30" \_\_\_\_\_  
Bake temperature: 200C \_\_\_\_\_  
Bake time: 2' \_\_\_\_\_
- 13.6 Spin on AZ5214 Resist (negative)  
4000rpm \_\_\_\_\_  
30seconds \_\_\_\_\_
- 13.7 Pre-Exposure-Bake:  
95C \_\_\_\_\_  
2 min \_\_\_\_\_
- 13.8 Edge bead removal  
Razor blade method, Or edge bead removal pattern  
If pattern, use 90 seconds expose time & develop in AZ400:Di 1:4
- 13.9 Expose with probe metal' from mask  
Expose time for old SUSS: 9" \_\_\_\_\_  
Expose time for new MA6 SUSS: 7" \_\_\_\_\_
- 13.10 Post-Exposure-Bake:  
110C \_\_\_\_\_  
1 min \_\_\_\_\_
- 13.11 Flood expose  
1 min \_\_\_\_\_
- 13.12 Develop the Resist: using diluted AZ-400K developer (dilution ratio of 1:4)  
  
40 seconds \_\_\_\_\_
- 13.13 Post- Development Bake  
110C \_\_\_\_\_  
1 min \_\_\_\_\_
- 13.14 1st Deep UV expose SF-11 Resist:  
1000W  
300 seconds \_\_\_\_\_
- 13.15 Develop SF-11 Resist: SAL101 Developer  
70 seconds \_\_\_\_\_
- 13.16 2nd Deep UV expose SF-11 Resist:  
1000W  
300 seconds \_\_\_\_\_

- 13.17 Develop SF-11 Resist: SAL101 Developer  
70 seconds \_\_\_\_\_
- 13.18 3rd Deep UV expose SF-11 Resist:  
1000W  
300 seconds \_\_\_\_\_
- 13.19 Develop SF-11 Resist: SAL101 Developer  
60 seconds \_\_\_\_\_
- 13.20 O2 plasma resist residue descum  
300 mT \_\_\_\_\_  
100 W \_\_\_\_\_  
1 min \_\_\_\_\_
- 13.21 Remove surface oxide:  
Rinse in HF:H2O (1:10) 30 sec \_\_\_\_\_  
  
Rinse in H2O 1 min \_\_\_\_\_
- 13.22 Load into e-beam 1 and deposit Ti;Au (100A;15000A)  
Ti \_\_\_\_\_ Use Angled deposition chuck  
Au: \_\_\_\_\_
- 13.23 Lift off in 1165 80C. Rinse in ISO. O2 descum in necessary to remove resist residue